COMPLEX DYNAMICS AND PERFORMANCE OF INHOMOGENEOUS THERMOELECTRICS

Von der Fakultät für Physik
der Universität Duisburg-Essen
genehmigte Disseration
zur Erlangung des Grades
Dr. rer. nat.
von

Sebastian Angst
aus Duisburg

Tag der Disputation: 30.09.2016

Referent: Prof. Dr. Dietrich E. Wolf

Korreferent: Prof. Dr. Christian Heiliger

ABSTRACT

This thesis aims to illuminate complex dynamics and performance of inhomogeneous thermoelectrics by means of a theoretical approach. For our investigations, we develop a versatile network model, which is based on the phenomenological Onsager-de Groot-Callen theory. This model allows us to study three setups related to the fabrication of a new type of thermoelectric generator.

The first setup is related to the production of the generator's raw material. Therefore, the current-activated pressure-assisted densification technique is applied to create nanostructured bulk material. The network model is designed to account for the complex dynamics caused by the particle motion during the densification. In particular, we investigate the influence of elongated pores parallel to the electrodes, which lower the conductivity. Moreover, we investigate a self-organized assembly of particles in binary particle mixtures.

With the second setup, we scrutinize the application of the Harman method to inhomogeneous material. The Harman method is often used to determine the thermoelectric transport properties. It turns out that this method employed on inhomogeneous material, systematically overestimates the absolute value of the Seebeck coefficient. It is demonstrated that the error is caused by the temperature distribution, which memorizes the influence of the priorly applied electrical current. Related to this, we show that the electrical power of double segmented generators is usually less than expected from the electrical conductivity and the true open circuit Seebeck coefficient. Nonetheless, we prove that by choosing transport parameters from a small range, a power enhancement can be obtained.

Finally, we investigate the usage of a pn junction as a generator, where the temperature gradient is parallel to the pn interface and electrodes are attached on the cold side. The dismissal of hot side contacts facilitates the application in high temperature regimes. In a first step, the diode character of the interface is neglected. We investigate the reduction of the electrical power compared to a conventional device. Thereby, we determine a relation between power and current. Furthermore, geometrical optimizations are discussed. In a second step, diode characteristics are included into the model, which leads to a qualitative agreement to experimental results.

ZUSAMMENFASSUNG

In der vorliegenden Dissertation werden die komplexe Dynamik und die Leistung inhomogener thermoelektrischer Materialien theoretisch untersucht. Dazu wird auf Basis der phänomenologischen Onsager-de Groot-Callen-Theorie ein vielseitiges Netzwerkmodell entwickelt. Dieses Modell ermöglicht die Analyse von drei Prozessen, die eng in Verbindung mit der Herstellung eines neuen thermoelektrischen Generatormodells stehen.

Der erste Prozess hängt mit der Produktion des Ausgangsmaterials des Generators zusammen. Hierbei kommt die stromaktivierte Druckverdichtung zum Einsatz. Das Netzwerkmodell ist so konzipiert, dass es die komplexe Dynamik, ausgelöst durch die Partikelbewegung während der Druckverdichtung, berücksichtigt. Von besonderem Interesse sind parallel zur Elektrode wachsende Poren, die die elektrische Leitfähigkeit verringern. Des Weiteren zeigt sich, dass bei Anwendung der stromaktivierten Druckverdichtung auf binäre Partikelmischungen eine selbstorganisierte Strukturbildung auftritt.

Der zweite Prozess entspricht der häufig zur Bestimmung thermoelektrischer Transporteigenschaften eingesetzten Harman-Methode. Diese erweist sich als fehlerhaft bei der Anwendung auf inhomogene Materialien. Bei segmentierten Strukturen und binären Partikelmischungen tritt ein systematischer Fehler auf, der zu einer Überbewertung des Betrags des Seebeck-Koeffizienten führt. Der Fehler rührt von der Temperaturverteilung her, welche den Einfluss des zuvor verwendeten elektrischen Stroms speichert. In diesem Zusammenhang wird gezeigt, dass die Temperaturverteilung in einem segmentierten Generator in der Regel zu einer Leistungsreduktion führt. Die Ausnahme bildet ein kleiner Parameterbereich, in dem der Generator eine größere Leistung liefert, als von den korrekt gemessenen Transportparametern zu erwarten wäre.

Schließlich wird die Benutzung eines pn-Übergangs als thermoelektrischer Generator untersucht. Da Elektroden lediglich auf der kalten Seite angebracht werden, ist der Einsatz bei sehr großen Temperaturunterschieden möglich. Unter Vernachlässigung der Dioden-Charakteristik erwirkt die Geometrie des pn-Generators allerdings eine deutlich Leistungreduktion gegenüber einem vergleichbaren gewöhnlichen Generator. Durch eine genaue Analyse kann ein funktionaler Zusammenhang zwischen Leistung und Strom bestimmt werden. Darauf aufbauend werden geometrische Optimierungen vorgenommen. Die Berücksichtigung der pn-Charakteristik liefert eine qualitative Übereinstimmung mit experimentellen Ergebnissen.

CONTENTS

LIST OF FIGURES

LIST OF TABLES

ACRONYMS

BD Ballistic deposit

CAPAD Current-activated pressure-assisted densification

CCA Cluster-cluster aggregate

CPM Constant property model

MD Molecular dynamics

ND Normal pressure-driven densification

PNG Pn junction generator

OBIV Optical beam induced voltage

SCR Space charge region

TE Thermoelectric

TEG Conventional thermoelectric generator

1 INTRODUCTION

The ability of thermoelectrics to convert heat into electricity and electrical power into heating or cooling facilitates a variety of applications. Motivated by the public discourse on climate change, which has highlighted the unavoidable necessity of reducing greenhouse gas emissions, we first mention waste heat recovery as one of the applications [1]. Bearing in mind that almost 60% of employed energy is wasted in form of heat underlines the big potential of waste heat recovery. In particular, electricity generation, transportation and industrial manufacturing processes leave vast amounts of energy unexploited [2, 3]. As an example, car manufacturers are working on replacing the alternator by a thermoelectric generator attached to the exhaust pipe [4]. On a prototype level researchers were able to save 2.2% fuel with this technique [5]. Further prototypes exist in the context of self-powered residential heating systems [6]. On a smaller scale, distributed energy harvesting has already reached the market in form of wood burning camping stoves, which produce electricity to power a combustion improving fan and to charge small batteries [7, 8].

However, the only moderate conversion efficiency of thermoelectric devices has so far hindered their application on a large scale. Furthermore, research still has to solve intricate challenges related to material and system design such that thermoelectric waste heat recovery systems produce energy with competitive costs per watt [9].

Research also focuses on abundantly available small temperature differences and pursues micro energy harvesting to power energy autonomous embedded systems. The body temperature of human beings or animals could provide energy for sensors delivering information for medical applications or wildlife tracking. In another example, it was shown that a sensor can be operated with the temperature difference between air and wall in a tunnel [10]. Such a system is extremely reliable, since the generator works without moving parts. The durability has been demonstrated by deep space probes powered by thermoelectric generators, which have been working for decades [11]. The heat is typically provided by Pu238 heat sources [12].

The fact that heat can be turned into electricity was discovered by Thomas J. Seebeck in 1821. A decade later Charles A. Peltier detected that electrical current transports heat, which is called Peltier effect, enabling electrical heating and cooling. The moderate coefficient of performance restricts its usage to niche applications such as cooling of micro chips [13]. In the 1950s, it was A. Ioffe who pointed out the advantages of heavily doped semiconductors as thermoelectric material, which led to first applications outside of a laboratory environment. Up to the 1990s thermoelectrics barely attracted attention until two strategies to improve material properties were proposed by L. D. Hicks/M. S. Dresselhaus [14] and G. Slack [15]. Former pro-

posed to use nanostructured materials in order to increase electronic properties, while the second approach is well described by the term electron-crystal/phonon-glass material. Both mentioned paths are accompanied by the usage of material compositions. This may happen on the atomic [16], nano and/or mesoscale [17, 18]. Beside material optimization, applying novel device concepts will be another way to increase the generator performance [19]. Some of those concepts are based on assembling distinct materials, which is beneficial for the performance of thermoelectric generators under large temperature differences [20, 21] or which enable the application of larger hot side temperatures [22].

In this thesis, we approach material compositions from a classical perspective using the phenomenological Onsager-de Groot-Callen theory. We support the investigation of complex material assemblies by developing a simulation tool based on the aforementioned theory, since analytical calculations are restricted to rare special cases. Our implementation is versatile, and we tackle various issues from the nano to the macro scale.

However, all our investigations are related to the production process of a generator made of a pn junction. Such a device is built and examined in the group of G. Schierning and R. Schmechel at the University of Duisburg-Essen. Since hot side contacts are not required, temperatures up to 780 °C can be applied [23]. This is unusual, since hot side contacts tend to fail at elevated temperatures. A further beneficial effect emanates from the junction itself. Simulations showed that additional charge carries are generated in the space charge region, which may enhance electrical power and efficiency [22].

The device is made of heavily doped, nanostructured bulk silicon. One upscalable way of creating nanostructured bulk material is compressing nanoparticles by current-activated pressure-assisted densification. In order to analyze this process, we perform simulations based on the network model. Our investigations focus on complex interrelations between thermoelectric transport and structure (see chapter 4). The quality of the material is assessed by the determination of the transport parameters. A widely used technique for this evaluation is the Harman method, which measures all transport coefficients of a device or a material in one single setup. We will show in chapter 5 that its application to inhomogeneous media leads to flawed results. As examples, we consider segmented materials and random composite materials. Motivated by Harman method results, we demonstrate that material composites may deliver more power than expected from its transport parameters (see chapter 6). Eventually, in chapter 7, we investigate the aforementioned generator made of a pn junction. Beside simulations, we show experimental results and work out essential elements.

Initially, however, we present the fundamental physics of irreversible processes and thermoelectrics (see chapter 2), and subsequently explain the network model in chapter 3.

2 FUNDAMENTALS

In this chapter we recap the phenomenological description of thermoelectricity by H.B. Callen [24], which is based on the thermodynamics of non-equilibrium processes, extensively presented by S. de Groot and P. Mazur [25]. It also incorporates Onsager's reciprocal relations [26, 27], whose proof was awarded by the Nobel Prize. Owing to aforementioned researchers the theory is called Onsager-de Groot-Callen theory. Moreover, in the last section we present prominent optimization strategies for thermoelectric material.

2.1 THERMODYNAMICS OF NON-EQUILIBRIUM PROCESSES

Systems out of equilibrium are present in all aspects of nature and industry. Non-equilibrium systems evolve irreversibly into thermodynamic equilibrium while producing entropy S, which is maximized in equilibrium. The latter is accounted for by classical thermodynamics also acting as the foundation of non-equilibrium thermodynamics, which is based on the concept of local equilibrium [28]. Thereto a non-equilibrium system is divided into cells, which are assumed to be in equilibrium exchanging energy and particles with surrounding cells. Intensive variables like temperature $T = T(\mathbf{r}, t)$, pressure $p = p(\mathbf{r}, t)$ and chemical potential $\mu_c = \mu_c(\mathbf{r}, t)$, originally established for equilibrium conditions, are defined locally within the cells, and become functions of position $\mathbf{r}$ and time t. Substituting extensive variables like entropy S and energy U by entropy density $s = s(\mathbf{r}, t)$ and energy density $u = u(\mathbf{r}, t)$, the laws of classical thermodynamics can be formulated locally. In order to obtain meaningful thermodynamic variables, cells should be small enough to resolve spatial variations of those variables. However, they should be large enough to reflect proper fluctuations: In equilibrium state variables fluctuate around an average value, but the fluctuations are small compared to the average. Since the ratio between fluctuations and average value increases with decreasing particle number, the cell size should not be too small ($\gtrsim 1\,\mu m$) [28].

For an open system exchanging heat and matter with its surrounding the second law of thermodynamics can be expressed in a balance equation [25, 29]

$$\frac{\mathrm{d}s}{\mathrm{d}t} + \nabla \cdot \mathbf{j_s} = \nu_S, \tag{2.1}$$

with the entropy current density $\mathbf{j_s}$ and the entropy production per volume ν_S. Focussing on the demands necessary for the description of thermoelectric effects, we utilize the Gibbs relation, which is assumed to be valid locally, in the following form

$$T\mathrm{d}s = \mathrm{d}u - \mu \mathrm{d}n, \tag{2.2}$$

where n is the concentration of charge carriers and μ the electrochemical potential. μ is related to the chemical potential μ_c and the electrical potential ϕ [30] via

$$\mu = \mu_c + q\phi, \tag{2.3}$$

with the particle's charge q. This separation of μ in an electrical and a non-electrical part can be made, if the electrical part does not affect non-electrical forces [29]. Combining eq. (2.2) with energy and particle conservation

$$\frac{\mathrm{d}u}{\mathrm{d}t} + \nabla \cdot \mathbf{j}_e = 0 \qquad \frac{\mathrm{d}n}{\mathrm{d}t} + \nabla \cdot \mathbf{j}_n = 0, \tag{2.4}$$

where $\mathbf{j}_e$ is the energy current density and $\mathbf{j}_n$ the particle current density, we get [29]

$$\frac{\mathrm{d}s}{\mathrm{d}t} + \nabla \cdot \underbrace{\left(\frac{1}{T}\left(\mathbf{j}_e - \mu \mathbf{j}_n\right)\right)}_{\mathbf{j_s}} = \underbrace{\mathbf{j_e} \cdot \nabla\left(\frac{1}{T}\right) - \mathbf{j_n} \cdot \nabla\left(\frac{\mu}{T}\right)}_{\nu_S}. \tag{2.5}$$

A comparison to eq. (2.1) lets us identify $\mathbf{j}_s$ and ν_S. The entropy production can be generalized to the bilinear form

$$\nu_S = \sum_i j_i F_i \tag{2.6}$$

containing currents j_i and their corresponding forces F_i. Concerning thermoelectricity, $\nabla\left(\frac{1}{T}\right)$ and $\nabla\left(\frac{\mu}{T}\right)$ are the conjugated forces for energy current density $\mathbf{j}_e$ and particle current density $\mathbf{j}_n$, respectively. In general, forces and currents are adjusted to the problem under consideration, e. g. chemical reactions, heat flow in anisotropic media and diffusion in multi-species fluids [26, 25, 28].

A current itself should be a function of the corresponding force, and if a system with small deviations from equilibrium is considered, it is justified to assume a linear relation between current and force [25, 31]. Indeed, it is empirically verified that numerous irreversible phenomena are well described by linear relations between current and force. Examples are Ohm's law for electric current, Fourier's law for heat current and Fick's law describing a matter flow due to concentration gradients. Astonishingly, the purely phenomenological ansatz has been affirmed in a vast range of experimental conditions [25]. Furthermore, it has been observed that j_i is not only evoked by F_i, but also by additional forces F_j. As an important example for such a cross effect thermoelectricity shall be discussed explicitly in section 2.2. Additional well-known cross effects occur in multi-species diffusive fluids, where the concentration gradient of one species affects the diffusion of the other species.

Summing up, the relation between flux and forces may be written as

$$j_i = \sum_j L_{ij} F_j \tag{2.7}$$

with constant and phenomenological transport coefficients L_{ij}. Inserting eq. (2.7) into eq. (2.6) one gets

$$v_S = \sum_{ij} L_{ij} F_i F_j. \tag{2.8}$$

From $v_S > 0$ we obtain conditions for L_{ij}. Assuming that one force is zero, it is directly inferred that

$$L_{nn} > 0 \qquad L_{ee} > 0. \tag{2.9}$$

Equation (2.8) corresponds to the definition of a positive definite matrix. Since a matrix L is positive definite when its symmetric part $L_s = (L + L^T)/2$ is positive definite as well, and since for symmetric matrices the latter is accompanied by a positive determinant, the coefficients L_{ij} have to fulfill

$$4 L_{nn} L_{ee} > \left(L_{ne} + L_{en}\right)^2. \tag{2.10}$$

Beside eqs. (2.9) and (2.10), a further relationship concerning the off-diagonal elements was established, namely Onsager's symmetry relation

$$L_{en} = L_{ne}. \tag{2.11}$$

Equation (2.11) implies the famous Kelvin relation (see section 2.2). William Thomson, also known as Lord Kelvin, calculated the relation bearing his name under the assumption that reversible effects can be treated independently from irreversible effects [29]. A proof of eq. (2.11) based on statistical arguments was achieved by Onsager [27]. Microscopic reversibility of physical processes is a necessary element of his proof. This principle is also known as detailed balance condition.

2.2 ONSAGER-DE GROOT-CALLEN THEORY

2.2.1 *Basics*

The theory of irreversible thermodynamics shall be applied to thermoelectricity. Having identified the relevant currents and forces in section 2.1, the coupled equations for the transport in a thermoelectric element read

$$\begin{pmatrix} \mathbf{j}_n \\ \mathbf{j}_e \end{pmatrix} = \begin{pmatrix} L_{nn} & L_{ne} \\ L_{en} & L_{ee} \end{pmatrix} \begin{pmatrix} \nabla\left(-\frac{\mu}{T}\right) \\ \nabla\left(\frac{1}{T}\right) \end{pmatrix}. \tag{2.12}$$

For practical reasons the energy flux is usually replaced by the heat flux $\mathbf{j}_q$, which fulfills

$$\mathbf{j}_e = \mathbf{j}_q + \mu \mathbf{j}_n. \tag{2.13}$$

Additionally, we use

$$\nabla\left(-\frac{\mu}{T}\right) = -\frac{1}{T}\nabla\mu - \mu\nabla\left(\frac{1}{T}\right) \tag{2.14}$$

to separate μ and T and employ their gradients explicitly. Next, using the expansion $\nabla(1/T) = -\nabla T/T^2$, particle and heat flux are expressed by

$$\begin{pmatrix} \mathbf{j}_n \\ \mathbf{j}_q \end{pmatrix} = \begin{pmatrix} L_{11} & L_{12} \\ L_{21} & L_{22} \end{pmatrix} \begin{pmatrix} -\frac{\nabla \mu}{T} \\ -\frac{\nabla T}{T^2} \end{pmatrix}. \tag{2.15}$$

The connection between transport coefficients from eq. (2.12) and eq. (2.15) are derived straightforwardly and can be found in [32]. The transport coefficients in eq. (2.15) again satisfy the conditions eqs. (2.9) to (2.11).

At this point the transport coefficients L_{ij} shall be connected to the experimentally observed quantities.

Electric conductivity Under isothermal conditions the electric current $\mathbf{j} = q\mathbf{j}_n$ reads

$$\mathbf{j} = \frac{-qL_{11}}{T} \nabla \mu. \tag{2.16}$$

A comparison to Ohm's law $\mathbf{j} = \sigma \mathbf{E}$, with the electric field $\mathbf{E} = -\nabla \mu/q$, leads to an expression for the electric conductivity

$$\sigma = \frac{q^2 L_{11}}{T}, \tag{2.17}$$

which is larger than zero, since $L_{11} > 0$.

Heat conductivity Now, the heat flux at open circuit conditions implying zero particle flux

$$\mathbf{j}_n = -\frac{L_{11}}{T} \nabla \mu - \frac{L_{12}}{T^2} \nabla T = 0 \tag{2.18}$$

is considered to result in

$$\mathbf{j}_q = -\frac{L_{22}L_{11} - L_{12}^2}{L_{11}T^2} \nabla T. \tag{2.19}$$

Equation (2.19) has the form of Fourier's law $\mathbf{j}_q = -\kappa \nabla T$ with open circuit heat conductivity

$$\kappa_{\text{oc}} = \frac{L_{22}L_{11} - L_{12}^2}{L_{11}T^2} \equiv \kappa, \tag{2.20}$$

where we have used $L_{12} = L_{21}$. Moreover, deriving the heat flux under closed circuit conditions comprising vanishing electrochemical gradient leads to

$$\mathbf{j}_q = -\frac{L_{22}}{T^2} \nabla T, \tag{2.21}$$

with closed circuit heat conductivity $\kappa_{\text{cc}} = L_{22}/T^2$.

Seebeck coefficient With $\mathbf{j} = 0$, the electric field $\mathbf{E} = -\nabla\mu/q$ is related to the temperature gradient via

$$\mathbf{E} = \frac{L_{12}}{qTL_{11}}\nabla T. \tag{2.22}$$

The Seebeck coefficient α is defined as the quotient of the electric field and the temperature gradient leading to

$$\alpha = \frac{L_{12}}{qTL_{11}}. \tag{2.23}$$

Peltier coefficient Regarding the heat transported by the electric current under isothermal conditions

$$\mathbf{j}_q = \frac{L_{21}}{qL_{11}}\mathbf{j} \tag{2.24}$$

the Peltier coefficient can be expressed as

$$\Pi = \frac{L_{21}}{qL_{11}} = \alpha T, \tag{2.25}$$

where the latter equality follows from Onsager's reciprocal relations $L_{12} = L_{21}$.

Considering the entropy current density $\mathbf{j}_s$ for $\nabla T = 0$, we find $\mathbf{j}_s = \mathbf{j}_q/T = \alpha q \mathbf{j}_n$, which emphasizes the relation of the Seebeck coefficient to the average entropy per particle $s_n = q\alpha$ [29, 32].

In summary, the transport equations are written in terms of the transport coefficients σ, κ, α as

$$\mathbf{j} = -\sigma\left(\nabla\mu/q + \alpha\nabla T\right) \tag{2.26}$$

$$\mathbf{j}_q = \alpha T\mathbf{j} - \kappa\nabla T. \tag{2.27}$$

Figure of merit All transport coefficients are condensed in the figure of merit $zT = \alpha^2\sigma T/\kappa$, which affects the efficiency of a thermoelectric generator and the coefficient of performance of a thermoelectric heat pump (see section 2.2.3). To emphasize its relevance we follow ideas presented in [32].

On the one hand, a generator requires a large heat flux, since $\mathbf{j}_q$ partly determines the power output. On the other hand, a large heat flux hinders the maintenance of a temperature difference. The latter is necessary in order to obtain a large voltage drop, which determines the power output as well. Largest heat flux is obtained with closed circuit conditions and maximized heat conductivity κ_{cc}. However, the voltage reaches its maximum in open circuit conditions at the highest possible temperature difference, requiring low κ_{oc}. In fact, what should be maximized for a good thermoelectric material is the quotient

$$\frac{\kappa_{cc}}{\kappa} = \frac{\alpha^2\sigma}{\kappa}T + 1 = zT + 1. \tag{2.28}$$

zT represents the quality of a thermoelectric material and most of the research aims at its improvement. Astonishingly, the temperature

T, an intensive quantity, appears in the definition of the quality factor, while the other quantities are material parameters. Nonetheless, the temperature has an important influence on the performance of a thermoelectric device and partly determines the working conditions.

2.2.2 *Stationary state distributions*

Using the coupled differential equations given by current conservation and local heat production

$$\nabla \cdot \mathbf{j} = 0 \qquad \nabla \cdot \mathbf{j}_q = \nabla \cdot \left(\mathbf{j}_e - \frac{\mu}{q} \mathbf{j} \right) = E \cdot \mathbf{j}, \tag{2.29}$$

where also energy conservation is taken into consideration, we are able to derive stationary state distributions of T and μ. Before we demonstrate the solution for constant properties, it is helpful to discuss $\nabla \cdot \mathbf{j}_q$. Applying eqs. (2.26) and (2.27), the local heat production is calculated as

$$\begin{aligned} \nabla \cdot \mathbf{j}_q &= T\mathbf{j} \cdot \nabla \alpha + \alpha \mathbf{j} \cdot \nabla T - \nabla \cdot (\kappa \nabla T) \\ &= T\mathbf{j} \cdot \nabla \alpha + \mathbf{E} \cdot \mathbf{j} - \frac{j^2}{\sigma} - \nabla \cdot (\kappa \nabla T) \,. \end{aligned} \tag{2.30}$$

The term $T\mathbf{j} \cdot \nabla \alpha$ deserves a detailed explanation. For that reason the Kelvin relation $\Pi = \alpha T$ is applied resulting in [25, 33]

$$T\mathbf{j} \cdot \nabla \alpha = T\mathbf{j} \cdot \nabla \left(\frac{\Pi}{T} \right) = \mathbf{j} \cdot (\nabla \Pi - \alpha \nabla T) \,. \tag{2.31}$$

Historically, two conditions have been distinguished: on the one hand an isothermal junction of two materials with different Peltier coefficients such that $\mathbf{j} \cdot (\nabla \Pi - \alpha \nabla T) = \mathbf{j} \cdot \nabla \Pi$ leading to Peltier heating or cooling at the interface and, on the other hand, a homogeneous thermoelectric material exposed to a temperature gradient:

$$\mathbf{j} \cdot (\nabla \Pi - \alpha \nabla T) = \mathbf{j} \cdot \nabla T \left(\frac{\mathrm{d}\Pi}{\mathrm{d}T} - \alpha \right) = \tau \mathbf{j} \cdot \nabla T \tag{2.32}$$

with the Thomson coefficient (e. g. [32])

$$\tau = \frac{\mathrm{d}\Pi}{\mathrm{d}T} - \alpha = T \frac{\mathrm{d}\alpha}{\mathrm{d}T}. \tag{2.33}$$

Both effects have the same origin: they are caused by a variation of the Seebeck coefficient and their nomenclature just refers to different conditions. Inserting eqs. (2.30) and (2.32) into eq. (2.29) one gets

$$\tau \mathbf{j} \cdot \nabla T - \frac{j^2}{\sigma} - \nabla \cdot (\kappa \nabla T) = 0. \tag{2.34}$$

Equation (2.34) may be used to derive the stationary state temperature distribution. In order to calculate the transient behavior eq. (2.34) has to be extended by a time derivative of the temperature, weighted by the volumetric heat capacity c [32]

$$\begin{aligned} c \frac{\partial T}{\partial t} + \nabla \cdot \mathbf{j}_q &= \mathbf{E} \cdot \mathbf{j} \\ c \frac{\partial T}{\partial t} &= \tau \nabla T \cdot \mathbf{j} - \frac{j^2}{\sigma} - \nabla \cdot (\kappa \nabla T) \,. \end{aligned} \tag{2.35}$$

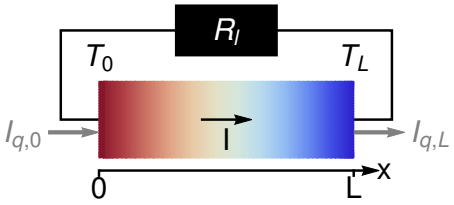

Figure 2.1: A sketch of a generator leg attached to a load resistance R_l.

Similarly, $\nabla \cdot \mathbf{j} = 0$ could be extended to derive the transient behavior of μ [34].

For a one-dimensional device and under the assumption of constant properties α, σ and κ eq. (2.29) can be solved analytically. This model is usually called constant property model (CPM), although due to the Kelvin relation the Peltier coefficient depends linear on temperature. Under CPM conditions eq. (2.34) becomes

$$\frac{\partial^2 T(x)}{\partial x^2} = -\frac{j^2}{\sigma\kappa}. \tag{2.36}$$

The current density j is assumed to be constant along the leg and the temperatures $T(0) = T_0$ and $T(L) = T_L$ at the boundaries of the one-dimensional system of length L are fixed and the solution reads

$$T(x) = -\frac{j^2}{2\sigma\kappa}x^2 + \left(\frac{T_L - T_0}{L} + \frac{j^2}{2\sigma\kappa}L\right)x + T_0. \tag{2.37}$$

The electrochemical potential distribution $\mu(x)$ follows from eq. (2.26) and eq. (2.37)

$$\frac{\mu(x)}{q} = \frac{\alpha j^2}{2\sigma\kappa}x^2 - \left(\frac{\alpha j^2}{2\sigma\kappa}L + \frac{j}{\sigma} + \alpha\frac{T_L - T_0}{L}\right)x + c_3. \tag{2.38}$$

The remaining constant c_3 is either given by a further boundary condition or can be set to zero if just the voltage difference matters.

Finally, we calculate the entropy production for constant properties in a thermoelectric material as follows

$$\nu_S = \mathbf{j}_e \cdot \nabla\left(\frac{1}{T}\right) - \mathbf{j}_n \cdot \nabla\left(\frac{\mu}{T}\right) \tag{2.39}$$

$$= \frac{\kappa(\partial_x T)^2}{T^2} + \frac{j^2}{\sigma T}. \tag{2.40}$$

The first term is the entropy production per volume due to Fourier heat conduction, while the second corresponds to entropy production by Joule heating per volume.

2.2.3 *Generator and heat pumps*

Although the actual setup is more complex, considering a single leg in the framework of CPM already leads to often used and suitable expressions for power and efficiency of a generator and heat pump.

GENERATOR Figure 2.1 shows a simple sketch of the generator leg considered here. The current I flows from the hot side at temperature T_0 to the cold side at temperature T_L[1]. It is produced by the Seebeck voltage $\alpha(T_0 - T_L)$. The heat flow at the hot side $I_{q,0} = j_{q,0}A$ and at the cold side $I_{q,L} = j_{q,L}A$ are derived from eq. (2.27) and eq. (2.37), where A is the cross section area:

$$I_{q,0} = j_q(0)A = \alpha T_0 I - \frac{I^2}{2G} + K(T_0 - T_L) \tag{2.41}$$

$$I_{q,L} = j_q(L)A = \alpha T_L I + \frac{I^2}{2G} + K(T_0 - T_L). \tag{2.42}$$

$G = \sigma A/L$ and $K = \kappa A/L$ are the electrical and the heat conductance of the leg. The power output is calculated from

$$P = I_{q,0} - I_{q,L} = \alpha(T_0 - T_L)I - \frac{I^2}{G}, \tag{2.43}$$

which leads to the efficiency

$$\eta = \frac{P}{I_{q,0}} = \frac{\alpha(T_0 - T_L)I - \frac{I^2}{G}}{\alpha T_0 I - \frac{I^2}{2G} + K(T_0 - T_L)}. \tag{2.44}$$

Often eqs. (2.43) and (2.44) are simplified by introducing the ratio $M = R_l/R$ between the load resistance R_l and the internal resistance $R = 1/G$. Using $\alpha(T_0 - T_L) = (R_l + R)I$ we can conclude

$$P = \frac{\alpha^2(T_0 - T_L)^2 M}{R(M+1)^2} \tag{2.45}$$

$$\eta = \frac{T_0 - T_L}{T_0} \cdot \frac{M}{M + 1 + \frac{(M+1)^2}{zT_0} - \frac{T_0 - T_L}{2T_0}}. \tag{2.46}$$

Analyzing the latter equations further, we find that P is maximized for $M = 1$ or $I = \alpha(T_0 - T_L)/(2R)$, while the maximum efficiency is reached at $M = \sqrt{1 + z(T_0 + T_L)/2}$.

HEAT PUMP In a thermoelectric heat pump a power source drives an electrical current I transporting heat from the cold side to the hot side as depicted in fig. 2.2. If it is desired to cool the cold side, I must be chosen such that the Peltier effect on the cold side is larger than Fourier heat and Joule heating. Equations (2.41) to (2.43) still hold and, hence, the coefficient of performance (COP) for a cooler reads

$$\varphi_c = \frac{I_{q,L}}{P} = \frac{\alpha T_L I + \frac{I^2}{2G} + K(T_0 - T_L)}{\alpha(T_0 - T_L)I - \frac{I^2}{G}}. \tag{2.47}$$

The maximum cooling power is reached at $I_{\max} = -\alpha T_L G$ leading to

$$I_{q,L}^{\max} = -\frac{\alpha^2 T_L^2 G}{2} + K(T_0 - T_L) = K\left(-\frac{zT_L^2}{2} + (T_0 - T_L)\right). \tag{2.48}$$

1 Throughout this work, the electrical current I flowing through the thermoelectric material is positive, if it flows from $x = 0$ to $x = L$.

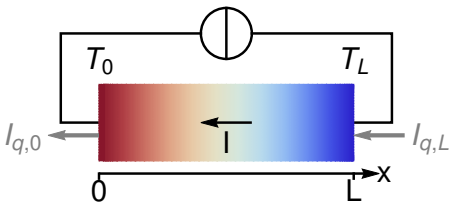

Figure 2.2: A sketch of a cooler leg driven by a power source .

The maximal temperature difference and hence the lowest T_L is achieved for $I_{q,L}^{\max} = 0$ and reads

$$(T_0 - T_L)_{\max} = zT_L^2/2. \tag{2.49}$$

If the device is operated as a heater, the hot side is of interest. Hence, the COP is given by

$$\varphi_h = \frac{I_{q,0}}{P} = \frac{\alpha T_0 I - \frac{I^2}{2G} + K(T_0 - T_L)}{\alpha(T_0 - T_L)I - \frac{I^2}{G}}. \tag{2.50}$$

In contrast to the cooler mode, a maximal hot side temperature does not exist, but φ_h has a maximum.

Note that some authors introduce a device figure of merit $Z = \alpha^2 G_{\text{tot}}/K_{\text{tot}}$ to account for parasitic losses in contacts.

2.3 MICROSCOPIC TRANSPORT MODEL

The Onsager-de Groot-Callen theory provides a fundamental understanding of thermoelectrics, but requires the input of phenomenological transport coefficients α, σ, κ. Those can be understood from a microscopic point of view within the framework of the adapted Landauer approach [35, 36, 37].

S. Datta (e. g. [36]) proposed the concept of an elastic resistor, depicted in fig. 2.3. For such a device it is assumed that electrons travel through a channel, which is characterized by the density of states (DOS), without gaining or loosing energy. Elastic transport does not necessarily imply ballistic transport. A diffusive transport may also be covered by the assumption as long as scattering only changes momentum but not energy. The conductive channel is attached to two reservoirs in equilibrium with temperatures T_1, T_2 and electrochemical potentials μ_1, μ_2, respectively. It is assumed that strong inelastic scattering within the large contacts maintains the equilibrium conditions [37] such that the contacts can be described by the Fermi function

$$f(E) = \frac{1}{\exp\left(\frac{E-\mu}{kT}\right) + 1}. \tag{2.51}$$

Equation (2.51) denotes the probability that a state with energy E is occupied in a system with temperature T. k is the Boltzmann constant.

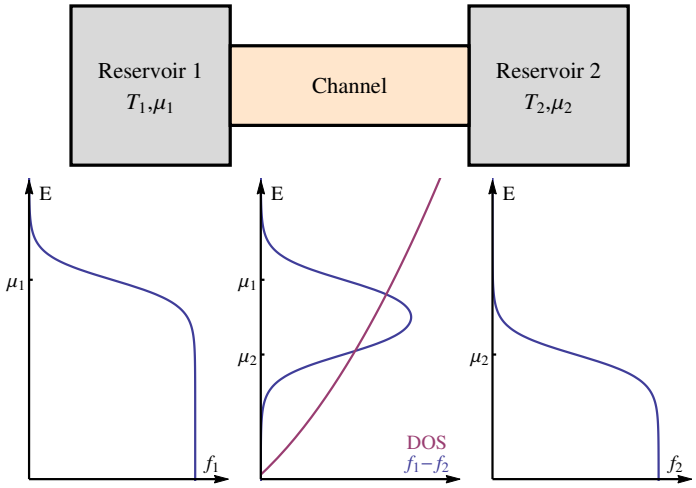

Figure 2.3: The elastic resistor is contacted as a channel to two reservoirs, which are in equilibrium characterized by the electrochemical potential μ_1, μ_2 and the temperatures $T_1 = T_2$.

Assuming $\mu_1 > \mu_2$ (e.g. maintained by attaching a battery), as shown in fig. 2.3, all states below μ_1 inside the channel get filled by electrons. At contact 2 electrons above μ_2 flow into reservoir 2, resulting in a steady electron current. Obviously, the difference $f_1 - f_2$ is the driving force for electron flow. Assuming that electrons with different energies travel independently through the conductor and taking into account spin degeneracy, the total electron current reads[2]

$$I_{\mathrm{el}} = \frac{2e}{h} \int_{-\infty}^{\infty} \frac{\lambda(E)}{\lambda(E) + L} M(E) \left(f_1(E) - f_2(E)\right) \mathrm{d}E, \tag{2.52}$$

where h corresponds to Planck's constant, e is the elementary charge[3], $M(E)$ is the number of modes, which is related to the DOS, and L is the length of the conducting channel. The term $T_{\mathrm{tr}} = \lambda/(L + \lambda)$ accounts for the transmission probability of an electron, where λ is its mean free path. In the limit of very large conductors, $L \gg \lambda$, $T_{\mathrm{tr}} \approx \lambda/L$ and the conductance eq. (2.54) vanishes with $1/L$ as expected from Ohm's law. In the ballistic regime, $L \ll \lambda$, T_{tr} approaches 1 resulting in a non-vanishing conductance. For small deviations from equilibrium leading to small voltages $V = (\mu_1 - \mu_2)/e \ll kT$, the approximation

$$f_1(E) - f_2(E) \approx (\mu_1 - \mu_2) \frac{\partial f_0}{\partial \mu} = (\mu_1 - \mu_2) \left(-\frac{\partial f_0}{\partial E}\right) \tag{2.53}$$

can be used, where $f_0 \approx f_1 \approx f_2$. Hence, the conductance of the elastic resistor reads

$$G = \frac{I_{\mathrm{el}}}{V} = \frac{2e^2}{h} \int_{-\infty}^{\infty} T_{\mathrm{tr}}(E) M(E) \left(-\frac{\partial f_0}{\partial E}\right) \mathrm{d}E. \tag{2.54}$$

2 Following the literature, we consider the electron current $I_{\mathrm{el}} = -I$ instead of the technical current I.

3 The electron's charge is $-e$.

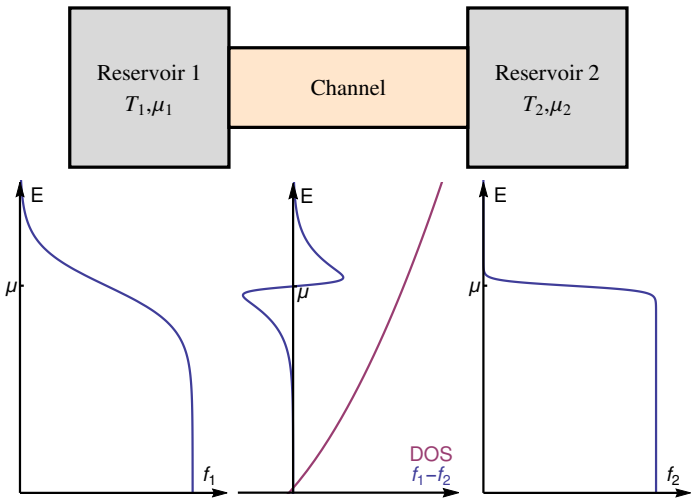

Figure 2.4: The electrochemical potential in both contacts are the same, but the temperatures $T_1 \neq T_2$ differ.

Equation (2.54) makes clear that the conduction mainly takes place in the $2kT$ window around the electrochemical potential.

It appears counterintuitive that a conductance and therefore a resistance is assigned to the channel implying that energy dissipation via Joule heating takes place, although it is assumed that the energy of an electron traveling through the channel does not change. This contradiction is resolved by the conjecture that the energy $\mu_1 - E$ is dissipated at contact 1 and $E - \mu_2$ at contact 2.

So far the differences between the Fermi functions in the contacts is due to differences in the electrochemical potential. Now, the consequences of temperature differences will be discussed leading to the Seebeck effect. Assuming $\mu = \mu_1 = \mu_2$ and $T_1 \neq T_2$, the difference $f_1 - f_2$ changes its sign at $E = \mu$ (see fig. 2.4) and electrons with $E > \mu$ are flowing from contact 1 to contact 2 and electrons with energy $E < \mu$ vice versa. Obviously, the net current depends on the DOS. If $\mathrm{d}D(E)/\mathrm{d}E > 0$ around μ as for n-type conductors, electrons flow from the hot to the cold side. In p-type conductors, where $\mathrm{d}D(E)/\mathrm{d}E < 0$, a net electron current from cold to hot is observed. Starting from eq. (2.52) we derive an expression for the Seebeck coefficient. Since a small temperature difference is the driving force, the Fermi function difference is approximated by

$$f_1(E) - f_2(E) \approx (T_1 - T_2)\,\frac{\partial f_0}{\partial T} = (T_1 - T_2)\,\frac{E-\mu}{T}\left(-\frac{\partial f_0}{\partial E}\right) \tag{2.55}$$

resulting in

$$I_{\mathrm{el}} = \underbrace{(T_1 - T_2)\,\frac{2e^2}{h}\int_{-\infty}^{\infty} T_{\mathrm{tr}}(E)M(E)\frac{E-\mu}{eT}\left(-\frac{\partial f_0}{\partial E}\right)\mathrm{d}E}_{G_S}\,. \tag{2.56}$$

Considering small $\mu_1 - \mu_2$ and small $T_1 - T_2$ the combination of the Taylor series expansion eqs. (2.53) and (2.55) results in

$$I_{\mathrm{el}} = G(V_1 - V_2) + G_S(T_1 - T_2), \tag{2.57}$$

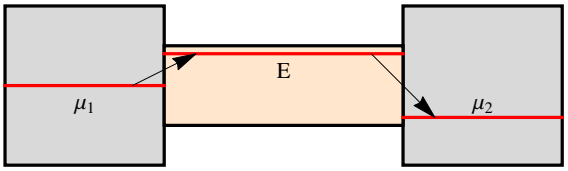

Figure 2.5: Charge carriers have to pick up an energy $E - \mu_1$ from contact 1 to get to energy E in the channel and they drop $\mu_2 - E$ in contact 2.

with $V_i = \mu_i/e$. The Seebeck coefficient is defined in open circuit conditions and given by

$$\alpha = \frac{V_1 - V_2}{T_1 - T_2} = -\frac{G_S}{G}. \tag{2.58}$$

Based on previous results, we comment on optimization of thermoelectric material within the scope of a one-level device defined by one energy level of width $\mathrm{d}E$ [36]. Studying the power factor $\alpha^2\sigma$ corresponding to the numerator of eq. (2.28) shows that it reaches its maximum if the energy level is around $2kT$ above or below the chemical potential. Thus, adjusting μ by adequate doping is one way to optimize thermoelectric material.

The following discussion of the heat current focuses on the heat transported by the electrons. Assuming energy levels as shown in fig. 2.5, an electron flowing into the channel from contact 1 extracts the energy $E - \mu_1$ in order to reach the transport energy level in the channel. Arriving at contact 2, it drops the energy $\mu_2 - E$. Hence, contact 1 is cooled, while contact 2 is heated. Dividing eq. (2.52) by e we get the number of electrons per unit time. Since each electron carries the energy $E - \mu$, the heat current reads

$$I_Q = \frac{2}{h} \int_{-\infty}^{\infty} T_{\mathrm{tr}}(E) M(E) \left(E - \mu\right) \left(f_1 - f_2\right) \mathrm{d}E. \tag{2.59}$$

And again, the difference $f_1 - f_2$, which arises due to a temperature and/or a electrochemical potential difference, is linearized and we get

$$I_Q = G_P \left(V_1 - V_2\right) + G_Q \left(T_1 - T_2\right). \tag{2.60}$$

with

$$G_P = \frac{2e^2}{h} \int_{-\infty}^{\infty} T_{\mathrm{tr}}(E) M(E) \left(-\frac{\partial f}{\partial E}\right) \frac{E - \mu}{e} \mathrm{d}E \tag{2.61}$$

$$G_Q = \frac{2e^2}{h} \int_{-\infty}^{\infty} T_{\mathrm{tr}}(E) M(E) \left(-\frac{\partial f}{\partial E}\right) \frac{\left(E - \mu\right)^2}{e^2 T} \mathrm{d}E \tag{2.62}$$

For a better comparison with experimental conditions, eq. (2.60) is often reformulated in terms of the electric current by applying eq. (2.57), resulting in

$$I_Q = \frac{G_P}{G} I_{\mathrm{el}} + \left(G_Q - \frac{G_P G_S}{G}\right) \left(T_1 - T_2\right), \tag{2.63}$$

with the Peltier coefficient $\Pi = G_P/G$ and the open circuit heat conductance $G_Q - G_P G_S/G$. To derive actual transport properties, it is necessary to determine $M(E)$ requiring the DOS, which can be gained, e. g. , from density functional theory and the mean free path.

2.4 optimization strategies for thermoelectric material

Starting in the 1950s, a lot of effort resulted in an increase of the figure of merit zT. A strong impact emanated from the work of A. Ioffe [38], who investigated semiconductors. Accordingly, thermoelectric materials in usage were, and still are, heavily doped semiconductors like Bi_2Te_3, Sb_2Te_3 among others, although those elements are scarce, expensive and harmful to health. Their figure of merit is limited to $zT \approx 1$ due to a strong interdependence of the transport parameters [39, 19]. In a highly degenerated semiconductor $\sigma \propto n$ and $\alpha \propto n^{-2/3}$ are intertwined by the charge carrier concentration n [16]. The heat conductivity can be separated into an electronic part κ_{el} and a phononic part κ_{ph}, where κ_{el} is directly proportional to the electrical conductivity $\kappa_{\mathrm{el}} = \sigma T L_L$ as stated by the Wiedemann-Franz law with the Lorenz number L_L [40]. zT reaches its maximum at an optimal charge carrier concentration, which is usually of the order 10^{19}-$10^{21}\mathrm{cm}^{-3}$ [16].

At the beginning of the 1990s new ideas entered the field of thermoelectrics, which can be summarized in two approaches [41]: Creating new bulk materials following the phonon-glass electron-crystal ansatz [15] and using low dimensional structures mainly inspired by L. Hicks and M. Dresselhaus [14]. While the first approach aims to decrease the phonon contribution to heat transport, the second intended to improve electrical properties. However, it turned out that most promising results were obtained by the reduction of κ_{ph} as well.

2.4.1 *Phonon-glass electron-crystal*

The rather peculiar requirements expressed by the term phonon-glass electron-crystal (PGEC) originate from the fact that the heat conductivity in glasses is remarkably low and that crystalline semiconductors exhibit a fair trade-off between the contradicting needs for high Seebeck coefficient and low resistivity [16]. The reduction of κ_{ph} in complex bulk materials can be induced by point defect scattering due to vacancies and interstitial atoms. Also, atom structures exhibiting rattlers have a low κ_{ph}. Furthermore, it has been suggested that the heat conductivity in certain complex structures scales inversely with the unit cell volume [42].

As an important example the material class of the so-called clathrates is discussed [43, 44]. Host atoms form a cage-like structure filled by guest atoms, the rattlers. A common approach for thermoelectrics is to use rather light atoms for the cage structure like Ga, Si, Ge and fill the eighth voids with heavy elements like Ba. Those materials are

semiconductors, therefore fulfilling the electron-crystal demand and have a rather large lattice parameter of the order of $10\mathring{A}$ [44]. Recently, it has been shown for $Ba_8Ga_{16}Ge_{30}$ that rattlers do not provide a strong scattering mechanism [45, 46], but rather alter the phonon dispersion relation in such a way that κ_{ph} is reduced. With this material class usually zT values around 1 are reached, but even $zT = 1.35$ [47] was found in $Ba_8Ga_{16}Ge_{30}$ at high temperatures $T = 900\,K$.

Filled skutterudites are another class of thermoelectric bulk material aiming in the direction of the PGEC approach [44]. Skutterudites are compositions of the form MX_3, where M is a metal atom and X stems from the pnictogen group [48]. Some of those compositions form holes, which can be filled by rattling atoms, also useful for doping. These materials are applicable in the intermediate and high temperature regime and figure of merits up to $zT = 1.7$ at $T = 850\,K$ have been observed in multiple filled skutterudites [49].

Recently, a very high zT of 2.6 ± 0.3 at 923 K was reported for SnSe [50]. It is the highest measured value so far and mainly attributed to its exceptional low thermal conductivity. Remarkably, SnSe is not characterized by a complex crystal structure or large unit cells.

2.4.2 *Low-dimensional thermoelectrics*

In their original work, Hicks and Dresselhaus [14, 51] theoretically revealed a strongly enhanced electrical performance in a two-dimensional quantum-well by means of theoretical arguments.

Although hints for an increased electrical performance were found in experiments [52], Kim et al. [53] argued that reducing the dimensionality does not necessarily bear great potential for improving the electronic part of zT. This is because an efficient usage of low dimensional materials requires very small structures and high fill factors. However, if the fill factor becomes too large the structures might lose their low dimensional properties.

On a related note, G. Mahan showed that the optimal DOS is a δ-function [54]. Sharp features of the DOS are experimentally realized in PbTe with resonant thallium impurity levels yielding $zT = 1.5$ at 773 K [55], which corresponds to a doubling of zT compared to the bulk value. Nonetheless, in up to date thermoelectrics the reduced heat conductivity has a much stronger influence than any change in the power factor [56].

One example of low-dimensional material with strongly reduced κ_{ph} are nanowires. Rough silicon nanowires were shown to have a figure of merit $zT = 0.6$ at room temperature [57, 58]. This is all the more impressive since bulk silicon has a very low room temperature zT in the order of 0.01. Especially the high heat conductivity of silicon in the range of $150\,WK^{-1}m^{-1}$ is the reason for the bad thermoelectric performance of bulk silicon. A further example are nanostructured superlattices. In a famous work on p-type Bi_2Te_3/Sb_2Te_3 a particularly high $zT = 2.4$ at 300 K was reported, which again is attributed to a reduction of the phonon heat conductivity [17].

The above mentioned experiments demonstrated the potential, but applying those materials in commercial application is difficult, since their production is too slow and expensive [39]. Another recent approach has the advantage of being easily upscalable and inexpensive [59]. There, nanometer-sized particles of well-known materials are produced by ball milling [39] or plasma synthesis [60], which are densified afterwards by hot pressing or current-activated pressure-assisted densification (CAPAD) (see chapter 4) in order to create nanostructured bulk material. It turned out that by nanostructuring κ_{ph} can even undercut the alloy limit, which was believed to be a lower limit for years. That is because in alloys phonons with short wavelength are preferentially scattered, while mid- to long-wavelength phonons are hardly affected and still transport heat. However, nanostructuring can introduce interfaces on those length scales, which leads to a lower heat conductivity than in alloys, if phonons with those wavelength contribute strongly to the heat transport [39].

Usually, electron flow is believed to be hardly affected by nanostructuring. In highly doped materials the mean free path of electrons is dominated by impurity scattering and of the order 2-5 nm [19]. Nonetheless, depending on fabrication details, a decreased electron mobility associated with an enhanced resistivity has been observed in nanostructured silicon [61].

One example for a successful implementation of bulk nanostructuring is Si, which is a very poor thermoelectric in its crystalline form. Nanocrystalline bulk silicon obtained from the gas phase and compacted by CAPAD reached figures of merit up to 0.6 around 1200 K [19, 62, 63]. Furthermore, nanostructured BiSbTe [59] produced by ball milling and hot pressing resulted in a 40% increased zT compared to an state-of-the-art ingot of the same material, basically achieved by a reduced heat conductivity.

Another sophisticated and promising ansatz consists of scattering phonons on all length-scales, which is accomplished by alloying, implementing a matrix structure on the nanoscale and creating grain boundaries on the mesoscale by CAPAD [18].

A lot of ideas of the preceding sections are dedicated to the reduction of κ_{ph}. But only recently, D. Narducci pointed out that especially for waste heat recovery it is necessary to dissipate a certain amount of energy, which restricts the choice of the material [64]. But even in a situation without this constraint, e. g. a generator operated between two reservoirs of constant temperatures, a critical contemplation is appropriate. The efficiency can be enhanced by reducing κ (increases zT). But in order to have a large power output, the heat current into the device needs to be large as well, which is aggravated by low κ. Thus, running a device at maximal efficiency guarantees that heat is converted at the highest rate, but it does not provide the highest possible power output [64].

2.4.3 *Further effects*

The phonon drag effect is caused by phonons giving momentum to the electron system, dragging them to low temperature regions and thus influencing the Seebeck coefficient [29]. Usually the cross-section is much larger for low energy phonons such that this effect is most pronounced at low temperatures.

The Seebeck coefficient is driven by the difference of two Fermi functions at distinct temperatures. This difference has a positive and a negative contribution to the Seebeck coefficient. Filtering out the electrons decreasing the absolute value of the Seebeck coefficient may lead to an increase of the thermopower [39]. The filtering is accomplished by introducing additional scattering mechanisms preferentially scattering unfavorable electrons. In superlattices energy filtering has been observed [65] and it could also be beneficial in nanostructured bulk materials [19]. However, it was shown using the Landauer formalism that significant effects from energy filtering require low doping concentration, which contradicts the demand for good thermoelectrics [66].

3 ONSAGER NETWORK MODEL

In this chapter we develop a network model, based on the phenomenological Onsager-de Groot-Callen theory.

The corresponding equations are analytically solvable in some special cases. One is the constant property model (CPM). This model has been studied extensively in one dimension and delivers a comprehensible understanding of thermoelectric devices [29, 67, 32, 68]. Another example of an analytically treatable special case is an one-dimensional thermoelectric with parameters depending linearly on the position [69]. Finding analytic solutions in two or three dimensions is not feasible.

Thus, numerical models were developed to support the description of thermoelectrics. Although based on the Onsager-de Groot-Callen theory, some of them neglect single thermoelectric effects since they do not include Joule heat and/or Peltier heat [70, 71]. Others are used to calculate either heat and electrical conductance or the Seebeck coefficient [72, 73, 74]. More complex models combined thermoelectricity with drift-diffusion models [75], which are applied to generators in intricate geometries [22]. For the investigation of complex, three-dimensional device structures including thermal coupling, radiation and convective heat flux, finite element simulation techniques are applied (e. g. [76]).

Our approach can be regarded as a finite volume method including all relevant effects and time-dependent variables as reviewed in [34]. We discretize the Onsager-de Groot-Callen theory on a network in a comprehensible and coherent way. This approach is versatile, and we will investigate bulk material represented by a square lattice, loose particle structures on lattices and continuous particle configurations. We validate the model by comparing the results to analytic expressions from CPM, one-dimensional segmented thermoelectrics and thermoelectrics with linear and temperature-dependent parameters.

Parts of this chapter have been published in [77].

3.1 MODEL DESCRIPTION

First, we recall the basic equations from the Onsager-de Groot-Callen theory as presented in chapter 2. Beside the electrical and heat cur-

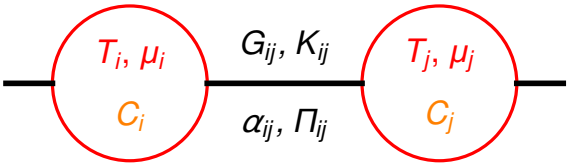

Figure 3.1: The variables T_i, μ_i and parameters, which are assigned to the sites and bonds, respectively, are shown for two connected sites.

rent density $\mathbf{j}$ and $\mathbf{j}_q$, respectively, their divergences are taken into account

$$\mathbf{j} = -\sigma \left(\nabla \mu / q + \alpha \nabla T \right) \tag{3.1}$$

$$\mathbf{j}_q = \alpha T \mathbf{j} - \kappa \nabla T \tag{3.2}$$

$$c \frac{\partial T}{\partial t} + \nabla \cdot \mathbf{j}_q = \mathbf{E} \cdot \mathbf{j} \tag{3.3}$$

$$\nabla \cdot \mathbf{j} = 0. \tag{3.4}$$

We assume that the electrical equilibration time is much shorter than the thermal equilibration time such that the electrochemical potential distribution $\mu(\mathbf{r})$ immediately adapts to temperature changes or changing boundary conditions. Thereby, local charging effects are neglected. However, μ varies with time due to temperature-dependent Seebeck voltages.

In order to discretize eqs. (3.1) to (3.4) on a network, we assign variable temperatures T_i and electrochemical potentials μ_i to each lattice site i (see fig. 3.1). The bonds between two connected sites i and j are characterized by the electrical conductance G_{ij}, the heat conductance K_{ij}, the Seebeck and Peltier coefficient, α_{ij} and Π_{ij}. In the network model the electric current I_{ij} and the heat current $I_{q,ij}$ between neighboring sites i and j read

$$I_{ij} = G_{ij} \left(\frac{\mu_i - \mu_j}{q} + \alpha_{ij} \left(T_i - T_j \right) \right) \tag{3.5}$$

$$I_{q,ij} = \mathrm{K}_{ij} \left(T_i - T_j \right) + \Pi_{ij} I_{ij}. \tag{3.6}$$

The material parameters $G_{ij}, K_{ij}, \alpha_{ij}, \Pi_{ij}$ are defined by the materials at site i and j. The electrical conductance of bond ij, half of which is of material i or j, is given by

$$\frac{1}{G_{ij}} = \frac{1}{2G_i} + \frac{1}{2G_j} + R_{\text{inter}}, \tag{3.7}$$

where an additional interface resistance R_{inter} is added. Likewise, the thermal conductance is calculated from the material properties i and j and an interface contribution $R_{\text{q,inter}}$ as

$$\frac{1}{K_{ij}} = \frac{1}{2K_i} + \frac{1}{2K_j} + R_{\text{q,inter}}. \tag{3.8}$$

Interface contributions become relevant if crystalline material, which is divided into grains by grain boundaries, is considered. In the following work we will neglect interface contributions, $R_{\text{inter}} = 0, R_{\text{q,inter}} =$

0, and focus on bulk effects. However, in chapter 4 we treat particles without distinguishing between bulk and interface explicitly.

To derive the connection between the bond Seebeck coefficient α_{ij} and α_i, α_j we have a closer look at the Seebeck voltage $\alpha_{ij}\left(T_i - T_j\right)$ between the sites i and j, which is the sum of two contributions: first, the voltage between site i and the interface located at the bond ij at temperature T_{ij} and second, the voltage between the interface and site j leading to

$$\begin{aligned}\alpha_{ij}\left(T_i - T_j\right) &= \alpha_i\left(T_i - T_{ij}\right) + \alpha_j\left(T_{ij} - T_j\right) \\ &= \bar{\alpha}_{ij}\left(T_i - T_j\right) + \Delta\alpha_{ij}\left(\overline{T}_{ij} - T_{ij}\right),\end{aligned} \tag{3.9}$$

where $\bar{\alpha}_{ij} = (\alpha_i + \alpha_j)/2$, $\overline{T}_{ij} = (T_i + T_j)/2$ and $\Delta\alpha_{ij} = \left(\alpha_i - \alpha_j\right)$. Approximating $\overline{T}_{ij} = T_{ij}$ eq. (3.9) simplifies to

$$\alpha_{ij} = \bar{\alpha}_{ij} = \frac{\alpha_i + \alpha_j}{2}. \tag{3.10}$$

The validity of this approximation will be discussed in section 3.2.

To specify the Peltier coefficient Π_{ij}, we have to take into account the Peltier heat $\Pi_i I_{ij}$, which is transported to site i, and $\Pi_j I_{ij}$ leaving site j. If both heat currents are not equal, the difference $(\Pi_i - \Pi_j) I_{ij}$ is released (or consumed) at the interface, which is often referred to as the (interface) Peltier effect [78]. We assume that this heat is delivered to (or taken from) both adjacent sites in equal parts. Thus, summing up, the net Peltier heat current at site i reads

$$\Pi_{ij} I_{ij} = \Pi_i I_{ij} - \frac{1}{2}\left(\Pi_i - \Pi_j\right) I_{ij} = \Pi_j I_{ij} + \frac{1}{2}\left(\Pi_i - \Pi_j\right) I_{ij} \tag{3.11}$$

with

$$\Pi_{ij} = \frac{\Pi_i + \Pi_j}{2} = \frac{\alpha_i T_i + \alpha_j T_j}{2}. \tag{3.12}$$

Due to the Kelvin relation $\Pi_i = \alpha_i T_i$ for site i.

In its discretized form the time evolution of the temperature at node i reads

$$\dot{T}_i = \frac{1}{C_i}\sum_j \left(-I_{q,ij} + I_{ij}\frac{(\mu_i - \mu_j)}{2q} \right), \tag{3.13}$$

where j runs over nearest neighbors of i. C_i is the specific heat capacity of site i. Electrical power produced on the bond ij is assigned to both adjacent sites in equal parts. Besides, the sum over the heat currents between i and j accounts for the divergence of the heat current, which contains Peltier and Thomson heat (see section 2.2). In our nomenclature a current I_{ij} or $I_{q,ij}$ has a positive sign, if it flows from node i to node j. Thus, the minus sign in $-I_{q,ij}$ ensures that the temperature increases if a heat current flows to node i. The electrodes are represented as nodes, which have either a fixed temperature or which have one external bond through which heat is exchanged with a heat bath of fixed temperature (see fig. 3.2). The typical time scale on which the heat current levels out temperature differences between

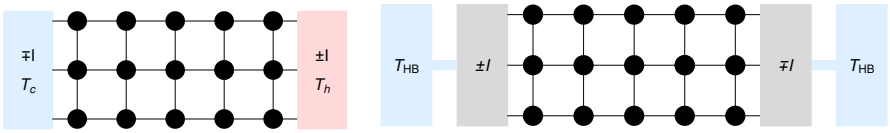

(a) (b)

Figure 3.2: Figure 3.2a: Two-dimensional example of the setup investigated in the current chapter. Between the electrodes, where the current I is injected or withdrawn, the material grid is located. The electrode temperatures T_h and T_c are fixed. Figure 3.2b: In contrast, here, the electrodes are connected to a heat bath of fixed temperature T_{HB} and the electrode temperature develop according to eq. (3.13).

neighboring sites reads C_i/K_{ij}. For the numerical integration the time step is about one-hundredth of the time scale of the fastest heat exchanging mechanism.

As explained above, we assume that $C_{\mathrm{el},i}/G_{ij}$ is much shorter than C_i/K_{ij}. Therefore, we neglect the electrical heat capacitance $C_{\mathrm{el},i}$. As a result, the electrochemical potential distribution instantaneously adapts to a temperature change, and the μ_i are obtained by a discretization of eq. (3.4), which corresponds to Kirchhoff's first law

$$0 = \sum_j I_{ij}, \tag{3.14}$$

where j runs over nearest neighbors of i. The nodes representing the electrodes have one external bond through which a fixed current I is delivered, respectively extracted from the system.

Now, the simulation procedure works as follows: An initial temperature distribution and a total current I entering the one electrode and leaving the other are provided. Specifying the electrical current I corresponds to attaching a load resistance R_l to the electrodes. Current and load are related via

$$I = \frac{U_\alpha}{R + R_l}, \tag{3.15}$$

where U_α denotes the Seebeck voltage and R the internal resistance of the thermoelectric material. The electrochemical potentials are calculated according to eq. (3.14). Several methods to solve such a system of linear equations are available, e. g. a fast node elimination algorithm [79] or a conjugate gradient method. Here, we use the latter implemented in the MTL4 library [80]. The resulting electrochemical potentials are fed into eq. (3.13) in order to calculate the temperatures for the next time step, which is done by an explicit 4th order Runge-Kutta method [81]. The temporal evolution of the temperatures requires a continuous update of the electrochemical potential distribution. Iteratively solving eq. (3.13) and eq. (3.14) gives the transient and finally the stationary state.

We aim to investigate quite different processes requiring varying setups and boundary conditions. To avoid redundancies, we implemented the solution of the thermoelectric transport as a base class.

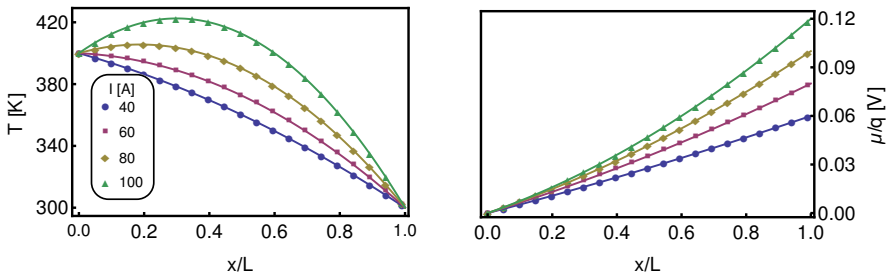

Figure 3.3: The temperature distribution (left) and the potential distribution (right) calculated with the model (symbols) and according to the CPM (line). Note that just the value of every fifth site is shown.

Each modeled process is implemented in a derived class, which inherits all basic functionality from the base class and just needs to provide setup and boundary condition.

Especially for the simulation of bulk material, it is desired to use real transport parameters, and in that case bond conductances are calculated from conductivities according to the discretization lengths.

3.2 MODEL VALIDATION

In the present section we validate the model comparing simulation results to analytic expressions. The analytic models are one-dimensional, and hence, we perform the following simulations on a one-dimensional grid.

3.2.1 *Constant property model*

The most common approximation is the one-dimensional CPM leading to eqs. (2.37) and (2.38). In the simulation, the electrodes are characterized by the same parameters as the material in between (see table 1), fulfilling the requirements of constant properties and circumventing Peltier heating/cooling at the electrode-sample interface. Here, the electrodes are characterized by a fixed temperature. The dimensions of the setup are $L = L_x = L_y = L_z = 10^{-2}\mathrm{m}$, which is discretized by $N = N_x = 100$ sites. Note that two additional sites represent the electrodes, such that in total $N + 1$ bonds are present. Figure 3.3 shows the comparison for an electrical current flowing in x-direction, which reveals a perfect agreement between eqs. (2.37) and (2.38) and the simulation.

The approximation $\overline{T}_{ij} = T_{ij}$ applied in eq. (3.9) is exact for $\Delta\alpha = \alpha_i - \alpha_j = 0$ as well as a linear temperature distribution $T(x)$. In

$\alpha[\mathrm{V/K}]$	$\sigma[\mathrm{S/m}]$	$\kappa[\mathrm{W/(Km)}]$
$2 \cdot 10^{-4}$	10^5	2

Table 1: The parameters used for the comparison between eqs. (2.37) and (2.38) and the simulation

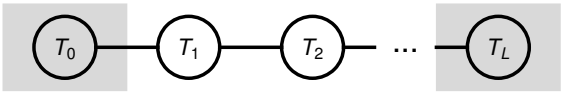

Figure 3.4: A chain of sites connected to electrodes (gray) with fixed temperature T_0 and T_L.

general, considering position- or temperature-dependent Seebeck coefficients and non-linear $T(x)$, the accuracy increases with N, as shall be shown in section 3.2.2.

Usually, when used as a generator, metal electrodes are attached to the thermoelectric material. Compared to the semiconductor, metals are characterized by a vanishing Seebeck coefficient. However, we show that electrodes with fixed temperature and $\alpha = 0$ should be avoided in the simulation, since the influence of the interface Peltier effect on the temperature distribution strongly depends on the discretization length $h = L/N$ as indicated by fig. 3.5. The effect of h will now be derived by means of solving the differential equation eq. (3.13) for T_1, the temperature of the site next to the left electrode (see fig. 3.4). Thereby, we approximate T_2 by $(T_0 + T_1)/2$, which is motivated by fig. 3.5. Note that $I_{10} = -I$ and $I_{12} = I$, while $I = -30\,\mathrm{A}$ corresponds to the current flowing through the thermoelectric from right to left. Furthermore, we use that a bond conductance is $N + 1$ times as large as the total conductances K, G and obtain

$$C\dot{T}_1 = -\left(\frac{3}{2}K(N+1) + \frac{\alpha}{4}I\right)T_1 + \frac{3}{2}K(N+1)T_0 \tag{3.16}$$

$$+ \frac{I^2}{G(N+1)} - \frac{\alpha}{4}T_0 I. \tag{3.17}$$

Setting $T_1(0) = T_0$ the solution of eq. (3.16) reads

$$T_1(t) = \left(T_0 + \frac{B}{A}\right)e^{\frac{At}{C}} - \frac{B}{A} \tag{3.18}$$

with

$$A = -\frac{1}{C}\left(\frac{3}{2}K(N+1) + \frac{\alpha}{4}I\right) \tag{3.19}$$

$$B = \frac{1}{C}\left(\frac{3}{2}K(N+1)T_0 + \frac{I^2}{G(N+1)} - \frac{\alpha}{4}T_0 I\right). \tag{3.20}$$

For the non-diverging stationary state $\lim_{t\to\infty} T_1(t) = -B/A$, which requires $A < 0$, we expand $-B/A$ for large N to first order and get

$$\lim_{t\to\infty} T_1(t) = T_0 - \frac{IT_0\alpha}{3KN} + \mathcal{O}(N). \tag{3.21}$$

The inset of fig. 3.5 illustrates that the approximation eq. (3.21) describes the data satisfyingly. Moreover, it shows how T_1 approaches T_0 for large N, which implies that the effect of Peltier cooling/heating vanishes as N tends towards infinity. Responsible for this unphysical behavior are the fixed electrode temperature and the diverging

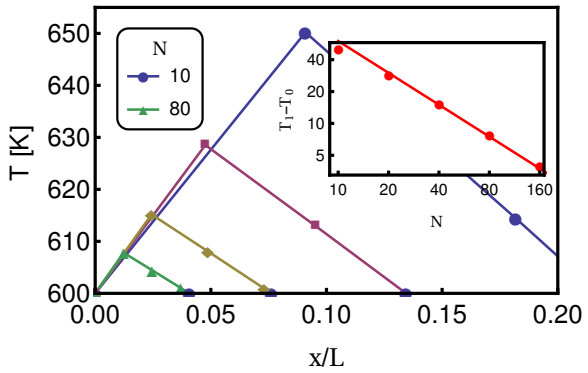

Figure 3.5: The stationary state temperature of the sites close to the left side strongly depend on the number of grid points N. The inset shows the the stationary state temperature difference $T_1 - T_0$ in dependence of N. The line is derived from eq. (3.21), which basically decreases as N^{-1}. For this simulation we choose $\alpha = 10^{-3}\,\mathrm{V/K}$, $\kappa = 1\,\mathrm{W/(Km)}$ and $\sigma = 10^5\,\mathrm{S/m}$.

heat conductance between adjacent sites. The fixed electrode temperature is unrealistic, since the heating/cooling affects both sides of the interface. Moreover, it is known that the Peltier heat is not a $\delta-$function, but rather slightly spread due to electron phonon heat exchange [82, 3].

As a consequence, for the simulation of devices we avoid using electrodes with negligible Seebeck coefficient and fixed temperatures.

3.2.2 *Segmented thermoelectrics*

As a further verification we consider thermoelectrics consisting of two segments of different materials A and B (see fig. 3.6) connected in series along the current direction.

The calculation [83, 84] of the analytic expressions for $T(x)$ and $\mu(x)$ bases on the assumption that for each segment, which is characterized by a corresponding parameter set, eq. (2.36) holds resulting in a piecewise quadratic temperature distribution

$$T(x) = \begin{cases} T_A(x) = -\frac{j^2}{2\sigma_A\kappa_A}x^2 + a_1 x + a_2 & 0 \le x/L \le f \\ T_B(x) = -\frac{j^2}{2\sigma_B\kappa_B}x^2 + b_1 x + b_2 & f < x/L \le 1 \end{cases} \tag{3.22}$$

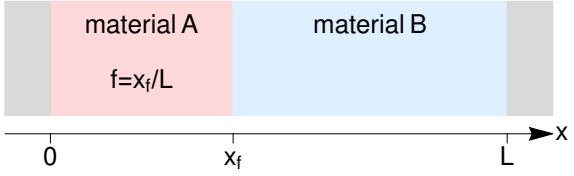

Figure 3.6: In this section we consider a segmented thermoelectric, which is a series connection of two materials A and B. f represents the fraction of material A.

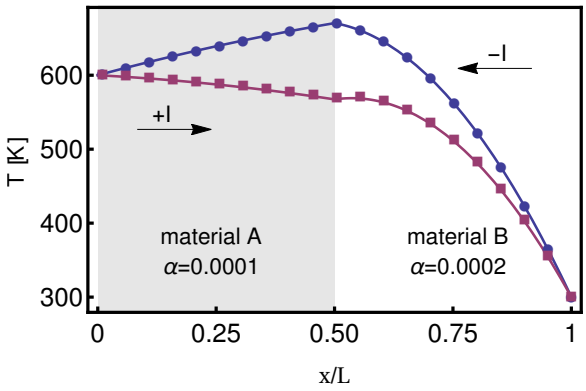

Figure 3.7: Temperature distribution in a segmented heterogeneous material calculated as in [84, 83] (lines) and the simulation result (points) for $I = 50\,\mathrm{A}$ (red) and $I = -50\,\mathrm{A}$ (blue). Parameters are taken from table 2

as well as a piecewise quadratic potential distribution

$$\frac{\mu(x)}{q} = \begin{cases} \mu_A(x)/q = \frac{\alpha_A j^2}{2\sigma_A \kappa_A} x^2 - \left(\frac{j}{\sigma_A} + \alpha a_1\right) x + a_3 & 0 \le x/L \le f \\ \mu_B(x)/q = \frac{\alpha_B j^2}{2\sigma_B \kappa_B} x^2 - \left(\frac{j}{\sigma_B} + \alpha b_1\right) x + b_3 & f < x/L \le 1 \end{cases} . \tag{3.23}$$

f is the quotient of the interface position x_f and the system length L and corresponds to the fraction of material A. The remaining coefficients for the linear and the constant term are determined from the following conditions: the temperature, the electrochemical potential, the energy flux and therefore the heat flux are continuous at the interface. Furthermore, the boundary temperatures are fixed. The extension to n segments is straight forward [83] and is shown in appendix A.

Fig. 3.7 depicts the temperature distribution for $I = 50\,\mathrm{A}$ (red squares) and $I = -50\,\mathrm{A}$ (blue points) calculated with $N = 100$. The effect of Peltier heating/cooling at the interface is clearly apparent and it is captured by the analytic expression (lines) and the simulation (points) in a convincing agreement. However, a closer examination reveals small deviations between simulation results and eq. (3.22). They stem from the fact that Peltier heat is introduced or withdrawn not exactly at the interface, but at the adjacent sites. The deviations vanish as N increases, since the sites constituting the interface are moved closer together.

Now, it shall be discussed in how far the total voltage U across a thermoelectric material is affected by the approximation eq. (3.9).

	α[V/K]	σ[S/m]	κ[W/(Km)]
material A	$1 \cdot 10^{-4}$	10^5	2
material B	$2 \cdot 10^{-4}$	10^4	1

Table 2: The parameters used for the simulations of a segmented TE.

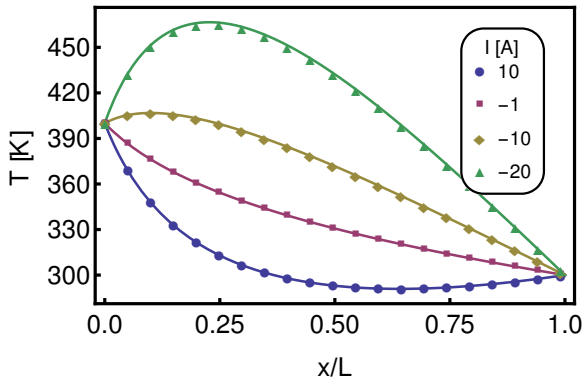

Figure 3.8: Temperature distribution for a linear property model. Symbols stems from simulations, while lines are calculated as in [69].

This is of particular interest, since the power and efficiency depend on U. We calculate the difference between the analytic voltage $U_{\text{theo}} = (\mu(L) - \mu(0))/q$ with $\mu(x)$ from eq. (3.23) and the voltage obtained from the simulation U_{sim}. We find that $U_{\text{theo}} - U_{\text{sim}}$ exactly equals $(\alpha_B - \alpha_A)(\overline{T}_{ij} - T(x_f))$, with $T(x_f)$ from eq. (3.22) and $\overline{T}_{ij} = (T_i + T_j)/2$, where sites i and j constitute the interface between material A and B. This difference is a direct consequence of the approximation eq. (3.9).

The deviation $U_{\text{theo}} - U_{\text{sim}}$ vanishes as N^{-1}, which can be made clear by considering the temperature difference

$$\overline{T}_{ij} - T(x_f) = \frac{1}{2}\left(T_i - T(x_f) + T_j - T(x_f)\right). \tag{3.24}$$

Equation (3.24) can be regarded as the sum of a forward and backward difference. According to the Taylor expansion

$$T(x \pm h) - T(x) = \pm T'(x)h + \frac{1}{2}T''(x)h^2 + \mathcal{O}(h^3), \tag{3.25}$$

forward and backward difference depend linearly on h for $h \to 0$. If the derivative of $T(x)$ is continuous, the sum of forward and backward difference is quadratic in h. However, a linear instead of a quadratic behavior in h is observed here, because the piecewise structure eq. (3.22) has to be taken into account. Thus, the linear term is not canceled out. In summary, each bond connecting two sites of different materials creates an error, which vanishes linearly with h or like N^{-1}.

3.2.3 *Linear properties model*

Here, the capability of the model to capture the influence of a continuous material distribution is reviewed.

For a Seebeck coefficient and a heat conductivity depending linearly on the position an analytic solution can be found [69]. The Seebeck coefficient reads

$$\alpha(x) = \frac{2\alpha_{\text{avg}}}{1 + \Delta_\alpha}\left(\Delta_\alpha + (1 - \Delta_\alpha)\frac{x}{L_x}\right), \tag{3.26}$$

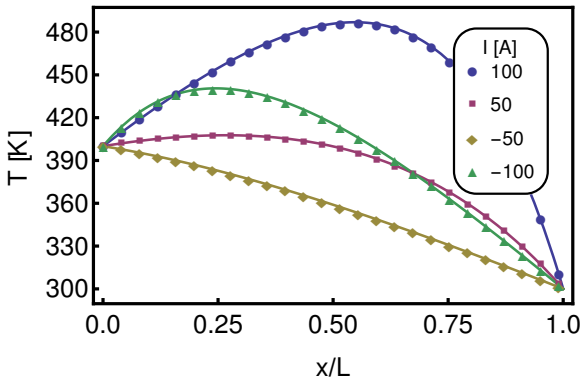

Figure 3.9: Temperature distribution for a model with constant σ, κ and τ. The Seebeck coefficient depends on temperature (see text).

where α_{avg} is the average value of the Seebeck coefficient and $\Delta_\alpha = \alpha(L)/\alpha(0)$ the ratio between maximal and minimal Seebeck coefficient. The heat conductivity is defined similarly. For the following simulations $\sigma = 10^5\,\text{S/m}$, $\kappa_{\text{avg}} = 1\,\text{W/(Km)}$, $\alpha_{\text{avg}} = 5 \cdot 10^{-4}\,\text{V/K}$ and $\Delta_\alpha = \Delta_\kappa = 0.111$.

In fig. 3.8 the temperature distribution for a cubic sample with edge length $L = 0.01\,\text{m}$ discretized by $N = 100$ sites is shown. As the good agreement suggests, the additional contributions are well captured by the simulation. Depending on the current, interesting distributions may occur. I. e. if the current is flowing from low to high Seebeck coefficients ($I = 10\,\text{A}$) Joule heating is overcompensated by $\nabla\alpha T\mathbf{j}$ such that the temperature distribution becomes concave. Also the term $\nabla \cdot (\kappa \nabla T(x))$ is responsible for a concave $T(x)$ as can be seen from the red curve ($I = -1\,\text{A}$).

3.2.4 *Temperature-dependent properties*

Obtaining analytic expressions for $T(x)$ for temperature-dependent properties is a difficult task. Here, a solution for a constant Thomson coefficient $\tau = Td\alpha/dT$ and hence, a temperature-dependent Seebeck coefficient, is presented. Heat and electric conductivity are constant. Then, from the heat divergence we obtain

$$\begin{aligned} \tau j \frac{\partial T}{\partial x} - \frac{j^2}{\sigma} - \kappa \frac{\partial^2 T}{\partial x^2} &= 0 \\ \Leftrightarrow \frac{\partial^2 T}{\partial x^2} - A\frac{\partial T}{\partial x} &= -B, \end{aligned} \tag{3.27}$$

with $A = \frac{\tau j}{\kappa}$ and $B = \frac{j^2}{\sigma\kappa}$. This inhomogeneous differential equation is solved by means of standard methods. Using the boundary conditions $T(0) = T_0$ and $T(L) = T_L$ we get

$$T(x) = T_0 + \frac{Bx}{A} - \left(T_0 - T_L + \frac{BL}{A}\right)\frac{e^{Ax} - 1}{e^{AL} - 1}. \tag{3.28}$$

A temperature-independent Thomson coefficient is present, if $d\alpha/dT \propto T^{-1}$, which requires a Seebeck coefficient depending logarithmically on T:

$$\alpha(T) = a \log(bT). \tag{3.29}$$

Such a dependence does usually not occur in real materials. Instead, for degenerated semiconductors the Seebeck coefficient is proportional to T, while it is inversely proportional to T in non-degenerated semiconductors. However, we use eq. (3.28) for a comparison to simulations (see fig. 3.9). Here, α obeys eq. (3.29) with $a \approx 3.476 \cdot 10^{-4}\,\mathrm{V/K}$ and $b = 225^{-1}\,1/\mathrm{K}$, such that $\alpha(300\,\mathrm{K}) = 10^{-4}\,\mathrm{V/K}$ and $\alpha(400\,\mathrm{K}) = 2 \cdot 10^{-4}\,\mathrm{V/K}$.

From the good agreement, it is possible to conclude that the model is able to capture all possible kinds of heat production in a thermoelectric material. Let us finally remark on the error made due to the approximation of the Seebeck coefficient. As mentioned in section 3.2.2, for a continuous $T'(x)$, the deviations between the simulated voltage and the analytically calculated voltage vanishes as N^{-2}, which could be recovered with the presented data.

3.3 CONCLUSION

We presented the successful development of a thermoelectric network model based on phenomenological transport equations. Simulation results have been compared to several one-dimensional analytic treatable cases, and we showed that all relevant aspects of thermoelectricity are covered by the model. Moreover, we discussed the consequences of model approximations. From that discussion we conclude that deviations to analytic models become severe, when the number of sites is not much larger than the number of interfaces between distinct materials. This discussion will be continued in section 5.3.

4

MODELING CURRENT-ACTIVATED PRESSURE-ASSISTED DENSIFICATION

4.1 INTRODUCTION AND BASICS

The current-activated pressure-assisted densification (CAPAD) represents a method to rapidly densify powders with little grain growth, which enables the production of materials with unique properties. The technique we denote by CAPAD is known under various names, as for instance spark plasma sintering (SPS) and field-assisted sintering (FAST), which are the most common ones [85]. All these names represent the same basic setup: A low pressure in the range of 10-100 MPa is applied on an initially porous powder, while a kA current is flowing either through the powder or the sinter die (see fig. 4.1). The pressure is too weak for a significant densification, and dissipation of electrical energy is used to heat up the powder enabling a strong compression. Here, we focus on the case of conducting powder, where most of the current flows through the powder implying a strong internal Joule heating. As proposed in [86] we use the name CAPAD capturing both important aspects, which lead to the success of the process.

CAPAD is a rather old technique: First patents for a sintering machine using current and pressure date back to the beginning of the 20th century [85]. However, commercial availability of CAPAD apparatus triggered vast research in the 90s [87]. In comparison to conventional methods, like hot pressing or pressureless sintering, whose processing times are in the range of hours, CAPAD creates materials with densities near to theoretical values within minutes, while keeping small grain sizes [86]. The latter is distinctly difficult with conventional techniques, which usually cause strong grain coarsening. Nonetheless, little grain growth is observed during CAPAD as well. For example, Bor doped nanoparticles with an average particle size of 10 nm are compressed to a dense bulk with average particle size of 43 nm [88]. In general, however, the grain growths depends strongly on process details like heating rate, holding times and temperature.

In the field of thermoelectrics CAPAD has been proved successful for several materials. Poudel et al. [59] created nanostructured BiSbTe with an approximately 40% higher conversion efficiency than the microcrystalline reference sample, where the enhancement mainly originates from the reduction of the lattice thermal conductivity. Further materials were reported to obtain better thermoelectric performances like Si [61], SiG, TiO_2 [85] and ZnO-based materials [87]. Beyond thermoelectrics, nanostructuring creates additional outstanding material properties like high wear resistance or optical features combined with high strength and hardness [89].

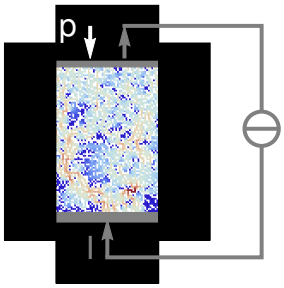

Figure 4.1: Sketch of the setup for CAPAD. The sample, whose local temperature is color-coded from blue to red, is located in between electrodes, which are attached to a power source (gray). A slight pressure p is applied to the upper movable electrode and a current I is imposed.

As pointed out by J. Garay [86], possible densification mechanisms include sintering, particle rearrangement and plastic deformation. Sintering refers to a mechanism caused by a reduction of the surface curvature, where the driving force arises from a decrease of the surface energy. Several transport mechanisms are related to sintering: surface, grain boundary and volume diffusion as well as evaporation and deposition. All of them lead to the growth of the contact area, but just by volume and grain boundary diffusion particle centers are moved closer together, which corresponds to a densification.

Regardless whether conducting or non-conducting powder is densified, particle rearrangement is among the relevant densification mechanisms for the early stage of the process [85, 90, 91, 92, 93, 94, 95, 96]. Particle rearrangement is pressure-driven, but temperature and current can play a major role.

For conducting materials, it has been pointed out that the percolating network of particles implicates high local current densities, which lead to hot spots. In those, particles can melt partially enabling the viscous sliding of particles, which recrystallize once the temperature has decreased [97]. The enlarged density in hot regions and the removal of oxide layers due to melting results in higher local electrical conductivity. This in turn, may inhibit the densification of loose regions, since the percolation pattern is burned into the powder. Experimental hints in form of density fluctuations were reported in [98]. In CAPAD experiments with non-conducting ceramics, the observed little grain growth and fast densification at the beginning of the process are related to particle sliding, while at high density atomic motion prevails [90, 93]. Particle sliding can be enabled by plastic deformation, local melting and softening [91, 92]. Note that the occurrence of significant temperature differences between particle center and particle surface is controversially discussed within the literature [99, 95, 100, 101, 102]. Moreover, particle rearrangement is also important in liquid phase sintering. In a recent experiment with Al_2O_3, it was shown that the electrical current flowing through the liquid phase reduces the viscosity of the liquid phase, which constitutes a coupling between electrical current and particle mobility as well [103].

Note that also electromigration has been discussed to influence densification, but usual current densities in CAPAD are too low to provoke electromigration (up to several $100\,\mathrm{kA/cm^{-2}}$ are necessary).

CAPAD process parameters are measured either globally, as density, current and voltage, or solely on the boundary, as the temperature, which is usually quantified by a pyrometer on the top or the bottom of the powders. However, spatial distributions of temperature and current and their effect on microstructure and material properties are of great interest. A couple of finite element and finite difference models have been developed to tackle this problem. Their complexity evolved starting from simulations focusing on temperature and electric current distribution in already densified samples. Those simulations aimed to predict temperature differences between the center of sample and pyrometer measurement [104]. Thereafter, densification was included [105]. Further finite element studies focused on the stress distribution inside the specimen [106] and the optimization of the tooling design [107]. Recently, a thermo-electrical-mechanical finite element framework was developed, taking into account grain growth and densification [108].

In the present work, we will take a different approach. We focus on the early stages of CAPAD, and using a network model, we investigate the intertwining of microstructure, current flow and densification, which has attracted little interest so far. Schwesig et al. [98] did a first theoretical study of the particle dynamics of CAPAD including the complex, inhomogeneous current pattern and the corresponding Joule heating, which influences the structure itself in an intricate way.

In this chapter we investigate two types of lattice models and eventually combine a lattice model with a molecular dynamic model to properly account for the particle motion. Parts of the following chapter have been published in [109, 110].

4.2 NETWORK MODEL

We reconsider the model developed by Schwesig et al. [98], which will be called model S in the following.

4.2.1 *Model details*

Model S is a network model on a hypercubic lattice. Occupied sites represent conducting particles, empty sites characterize voids and two neighboring particles are connected by a bond ij, carrying the electrical conductance G_{ij}. Electrodes are attached at the top and the bottom, spanning the whole grid. The upper electrode can move downwards to simulate the densification process. In the following we confine the analysis to 2d.

The basic simulation works as follows: An initial configuration is created by randomly placing particles on the grid until a predefined density is reached. If the particle configuration is not percolating, which means that both electrodes are not connected by a path of

bonds between occupied sites, it is assumed that the structure becomes mechanically instable. In that case all particles connected to the upper electrode are shifted downwards until percolation is established. Predefining a current I, which enters one electrode and leaves the other, we are able to derive local Joule heating as described below. If the heating of a particle exceeds a threshold, it becomes mobile and it is moved. This may lead to an interruption of percolation, which is followed by a further densification.

Let us now come to a detailed description of those processes. We assume that heat is introduced in current pulses of length Δt_1. The time between successive pulse $\Delta t_2 \gg \Delta t_1$ is much longer than the time the system needs to relax into a state with negligible spatial temperature fluctuations. We approximate particle temperatures T_i by the average temperature

$$\langle \overline{T} \rangle = \frac{1}{\Delta t} \int_0^{\Delta t} \left(\frac{1}{N} \sum_i T_i \right) \mathrm{d}t \tag{4.1}$$

with $\Delta t = \Delta t_1 + \Delta t_2$. The current pulse produces the Joule heat $I_{ij}^2 G_{ij}^{-1}$ on bond ij, which is assigned to both adjacent particles in equal parts such that particle i receives the heat

$$\Delta Q_i = \tfrac{1}{2} \sum_j I_{ij}^2 G_{ij}^{-1} \Delta t_1, \tag{4.2}$$

where j runs over all occupied neighboring sites of particle i. Note that model S does not take into account Seebeck and Peltier effect. Regulating the process such that the average temperature is kept constant, Joule heating compensates for heat losses to the environment characterized by temperature T_{HB}

$$\Delta Q_{\mathrm{loss}} = K_0 (\langle \overline{T} \rangle - T_{\mathrm{HB}}) \Delta t = \sum_i \Delta Q_i. \tag{4.3}$$

A current pulse lets the temperature of particle i rise to

$$T_i = \langle \overline{T} \rangle + \tfrac{1}{C_i} \Delta Q_i. \tag{4.4}$$

If the particle temperature T_i reaches T_m, it becomes mobile. We rewrite this condition in a particularly beneficial way using eqs. (4.3) and (4.4) leading to a definition of the melting threshold m:

$$\frac{\Delta Q_i}{\Delta Q_{\mathrm{loss}}} \geq \frac{C_i}{K_0 \Delta t} \left(\frac{T_m - T_{\mathrm{HB}}}{\langle \overline{T} \rangle - T_{\mathrm{HB}}} - 1 \right) \equiv m. \tag{4.5}$$

The left hand side of eq. (4.5) is independent of I and as a consequence eq. (4.3) can always be fulfilled by an appropriate rescaling of I, which has no further effect on the simulation. The above physical interpretation is not unique and further, slightly different explanations can be found in [98, 111, 110]. However, all interpretations share a comparable dependence of m on mobilization and sample temperature.

If the mobilization criterion for a particle i is fulfilled, it is squeezed randomly into nearest or next nearest empty sites. If several particles

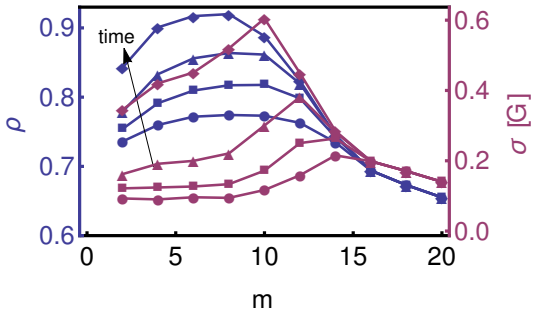

Figure 4.2: Density ρ (blue) and conductivity σ (red) for varying thresholds m after 500 (circles), 2000 (squares), $10n^4$ (triangles) and $5 \cdot 10^5$ (stars) time units Δt. Initial density is $\rho = 0.6$ and each data point is averaged over 100 runs with different initial setups.

are mobile, they are moved in a random sequence. For the implementation, the physical origin of the particle mobilization is insignificant as long as it is related to a temperature threshold. The particle motion may lead to an interruption of the connection between the electrodes. Then the upper electrode and all particles connected to it are moved downwards until percolation is re-established. The process stops, if no particle gets enough heat to exceed the threshold.

As natural units we use the parameters $I = 1$, $C_i = 1$, $G_{ij} = 1$, Δt and the particle diameter d.

4.2.2 *Influence of pores on electrical conductivity*

In this section, we will extend the explanation for an intricate relation between density and conductivity published in [111]. Furthermore, we show hints that former results belong to transient behavior. Therefore, we use a 100×100 grid with 100 different initial structures with density $\rho = 0.6$, which is slightly above the site percolation threshold.

In fig. 4.2 density and conductivity are depicted for varying m and at different times $t = 500$ (circles), $t = 2000$ (squares) and $t = 10^4$ (triangles) and $t = 5 \cdot 10^5$ (stars). Previous investigations included simulations up to $t = 400$ [111], and in order to extrapolate to the final state, which is characterized either by full density or by a configuration without mobilized particles, fit functions were used. However, those fit functions are not sufficiently describing the presented data, making an extrapolation impossible. Nonetheless, from fig. 4.2 we recognize that for large m the compression has reached a final state. Moreover, for $m \leq 1$ we can predict that always mobile particles are present, which enables, but not compels full density. Interestingly, in a fully densified state ($\rho = 1$) and for $m \leq 1$ all particles are mobile, because each particle receives the same Joule heat, but for $\rho < 1$ not all particles reach the mobilization threshold. Considering $m > 1$, full density can be reached as well, but whether a system ends up with $\rho = 1$ is difficult to foresee and depends on the details of each configuration.

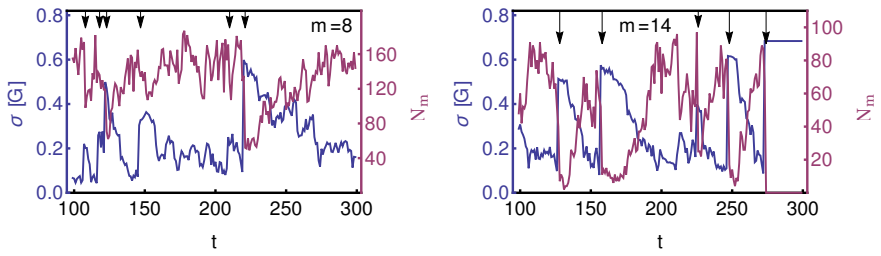

Figure 4.3: The conductivity σ and the number of mobile particles N_m are shown over time for one configuration and for $m = 8$ (left) and $m = 14$ (right). Times at which a densification steps takes place are indicated by an arrow. They are usually accompanied by strong increase of σ and a strong decrease of N_m, respectively.

Turning back to fig. 4.2, we recognize that ρ reaches a maximum at intermediate mobilization thresholds $m \approx$ 8-10. Its position depends slightly on time. Effects of system sizes and system shape on the maximum have not been considered here, but are expected. For large m, only in current bottlenecks Joule heating is strong enough to overcome the mobilization threshold. Since the current is distributed sufficiently after a few compaction steps, further mobilization is inhibited and compaction stops. For small m, whole parallel current paths are mobilized, instead of particles in low density cross-sections. Due to the high number of mobile particles, disintegrated paths are restored within a current pulse. The probability of interrupting the percolation shrinks, slowing down densification. With increasing time and density, it is observed that more time is necessary to compress the powder further, which is mainly attributed to the fact that an interruption of percolation becomes more unlikely at high densities.

The conductivity $\sigma = GL_x/L_y$, which is derived from the total conductance of the sample G and the dimensions L_x, L_y, is as well characterized by a time-dependent maximum. In general, highest density is associated with largest conductivity, but both maxima occur at different m, and we always find a regime (e. g. $10 < m < 14$ at $t = 500$), in which σ decreases while ρ increases. In order to understand this counterintuitive result, we consider the subtle correlations between particle configuration and conductivity created during the process [111]. To densify a system rapidly (e. g. with $m = 8$), fast growth of pores parallel to the electrodes are favorable. However, large pores cut off current paths and force the current to flow through bottlenecks, which lowers the conductivity. And indeed, particle configurations and pores statics reveal that large, elongated pores are more likely in dense systems $(m = 8)$ than in looser packages $(m = 14)$. Those pore structures are also reflected by current distributions. A significantly higher probability of large currents is found in systems compacted with $m = 8$ in comparison to those compacted with $m = 14$.

The general relation between pore structure and conductivity was mentioned before [111]. In the following, we elaborate this argument and show that m affects the conductivity in several ways.

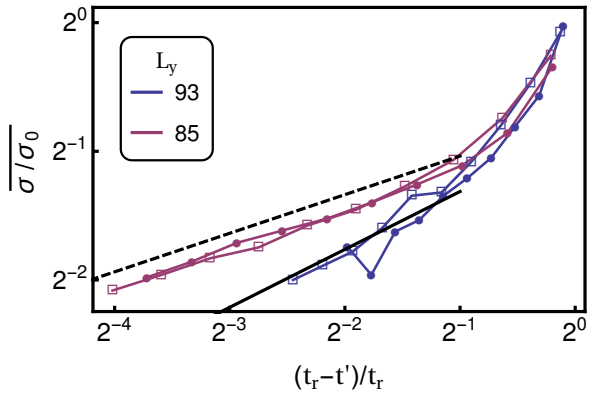

Figure 4.4: The figure shows how the conductivity evolves in time for constant L_y and for $m = 8$ (disks) and $m = 14$ (empty squares). It is normalized by $\sigma_0 = \sigma(L_y)$, which is the conductivity directly after a compaction step. It is plotted as a function of $(t_r - t')/t_r$, where t_r is the time to rupture of percolation. We used 500 different samples. However, just 80% of the samples could be compressed to $L_y = 85$ for $m = 14$. The black line represents a power law with exponent $\alpha = 0.3$ and the black dashed line with exponent $\alpha = 0.5$.

Figure 4.3 shows a typical behavior of the conductivity and the number of mobile particles N_m for $m = 8$ (left) and $m = 14$ (right). Observable in both cases, and of special interest, is the behavior strongly related to compression steps, which are indicated by arrows. Those are superimposed by smaller fluctuations. Nonetheless, we recognize that with each compression step N_m decreases drastically, while σ increases strongly. Between two compression steps N_m and σ behave inversely, which is attributed to pore growth parallel to the electrodes, lowering the conductivity and focusing the current, which leads to more mobile particles. We emphasize that at constant density the influence of the pore structure on σ and N_m is enormous. Looking closer at σ we realize that $\sigma(m = 8) < \sigma(m = 14)$, just as indicated in fig. 4.2. Furthermore, for $m = 14$ it can be recognized that directly at or shortly after (in different cases) the last densification step N_m equals zero. This is not surprising, since directly after a densification step a more homogeneous current distribution is achieved, lowering the chance to overcome the mobilization threshold. As a consequence, it is highly probable that the compression stops in a well-conducting configuration in comparison to the fluctuations induced by compression and pore growth.

Further insight is obtained by a detailed analysis of the decay of the conductivity between two compaction steps. Figure 4.4 shows the rescaled conductivity for $m = 8$ and $m = 14$ at different L_y in dependence of $(t_r - t')/t_r$, where t_r is the time between two compaction steps (also called breakdown time), and t' is set to zero after each compaction. We averaged over 500 different initial configurations with the same density and system size. However, for $m = 14$ only 80% of the samples reached $L_y = 85$ within the simulated 4000 time steps. We derived t_r, which may vary strongly, individually for each

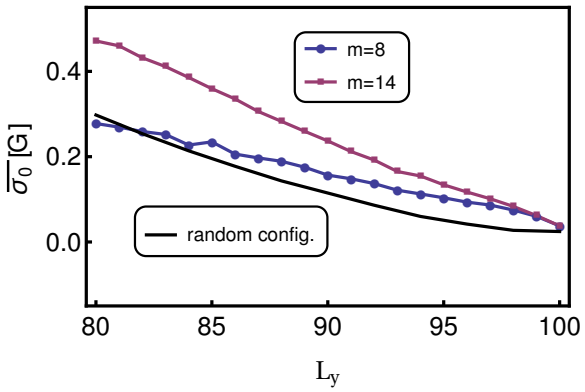

Figure 4.5: The dependency of the average conductivity $\overline{\sigma}_0$ with L_y is shown for $m = 8$ and $m = 14$. The black line corresponds to the conductivity of a randomly created system with the same number of particles.

sample and height L_y. Furthermore, we rescaled the conductivity by σ_0, which corresponds to the conductivity directly after a compaction step ($t' = 0$). Subsequently, data are binned in 10 bins and the average conductivity $\overline{\sigma/\sigma_0}$ for each bin is derived. At first, we recognize that the influence of m is considerably weaker than the influence of L_y. As L_y decreases t_r increases, which is mainly attributed to the higher density. For $(t_r - t')/t_r \gtrsim 0.5$ a rapid decay of $\overline{\sigma/\sigma_0}$ is observed, which is nearly equal for $L_y = 93$ and $L_y = 85$. For $(t_r - t')/t_r \lesssim 0.5$ a different behavior occurs, which can be approximated by a power law

$$\overline{\sigma/\sigma_0} \sim \left(\frac{t_r - t'}{t_r}\right)^{\beta}. \tag{4.6}$$

Here, we find $\beta = 0.3 \pm 0.02$ (black dashed line) for $L_y = 93$ and $\beta = 0.5 \pm 0.05$ for $L_y = 85$ (black line). Although the data just span a small range on the abscissa and the ordinate, we describe the data by a power law. The usage of a power law is motivated by a similar behavior observed in the dynamic thermal fuse model [112, 113, 114]. Likewise it consists of resistors on a grid, which are warmed up by Joule heating until a temperature threshold is exceeded and the resistor is irreversibly burned through. The process terminates when percolation between the two electrodes is interrupted. Of particular interest are fracture patterns, the breakdown time and the divergence of resistance, which was found to follow the power law

$$R \sim \left(\frac{t_r - t'}{t_r}\right)^{-\beta} \tag{4.7}$$

with $\beta = 0.28 \pm 0.05$ [114]. Although details of the model differ from model S, we find that both power laws are characterized by close exponents, especially at the beginning of the compression (large L_y). However, a detailed analysis of the influence of model parameters, like density and system size, is required, to make a comparison more valuable.

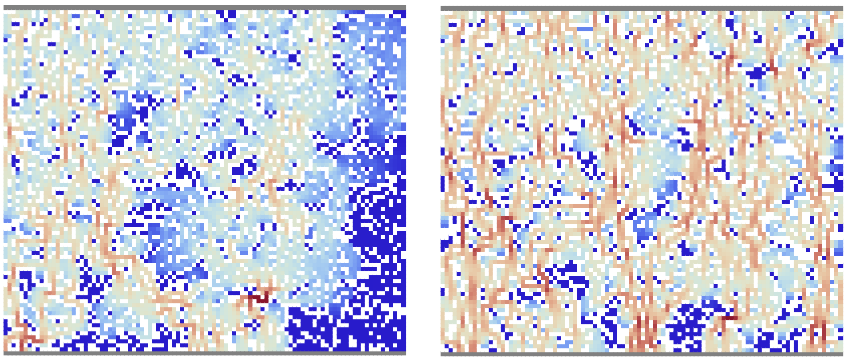

Figure 4.6: Typical configurations and heat distributions at $L_y = 85$ for $m = 8$ (left) and $m = 14$ (right) occurring directly after a compaction step. Heat is color-coded from red (hot) to blue (cold). Electrodes are printed in gray.

Next, we discuss the average conductivity $\overline{\sigma}_0$ depicted in fig. 4.5 for varying L_y. Straight from the beginning of the process, a system compacted with $m = 8$ has a lower conductivity than a system compacted with $m = 14$, and this difference grows as L_y shrinks. The reason for the difference is illustrated qualitatively using typical heat distributions occurring directly after a compaction step (see fig. 4.6). In comparison to a sample compacted with $m = 14$, the heat distribution of a sample compacted with $m = 8$ is clearly more inhomogeneous. This inhomogeneity stems from larger pores, which cut off current paths as discussed before. Since a compaction step usually densifies one pore, we conclude that with $m = 8$ several hot spots create various large cracks, where some remain after compaction. The black line in fig. 4.5 corresponds to the average conductivity $\overline{\sigma}_R(L_y)$ derived from 100 different configurations created by randomly placing particles on empty sites for given L_y. The number of particles $N = 6000$ and the length L_x are fixed. Close to the percolation threshold (large L_y) we observe $\overline{\sigma}_0 > \overline{\sigma}_R$, which indicates that the selective motion of particles in current bottlenecks and the following extinction of large pores is slightly more advantageous for enhanced conductivity than using random configurations. With shrinking L_y, multiple pore growth for $m = 8$ lead to a weaker increase of $\overline{\sigma}_0$ than of $\overline{\sigma}_R$.

Recapping the previous argumentation, we name three mechanisms affecting the conductivity at a given time as plotted in fig. 4.2:

- The amount of samples which reached a final state, since those are very likely to be homogeneous and highly conductive. To clarify the significance of this argument we emphasize that between two compaction steps the conductivity may vary up to a factor 4 (see fig. 4.4). σ_0 increases by about the same factor while densifying from $L_y = 95$ to $L_y = 80$ (see fig. 4.5).

- The conductivity after compaction $\overline{\sigma_0}$, which is controlled by m via the number of large pores (see fig. 4.5).

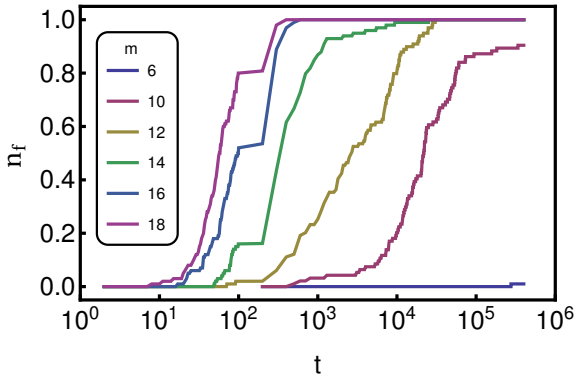

Figure 4.7: Amount of samples n_f in final state over time for various m. 100 samples were taken into consideration.

- The density and related to it the distance between both electrodes.

Finally, we comment on the likelihood of reaching final states. Therefore we consider the number of systems in final state $n_f(t)$ over time. In fig. 4.7 $n_f(t)$ is shown, whereby 100 samples have been taken into account. All curves in range $10 < m < 20$ are characterized by the same steep increase. For smaller mobilization thresholds, the simulation time is not sufficient to let systems reach a final state. Note that the size of the cross section area strongly affects the time scale, due to the lower possibility of depleting a large cross section area.

4.3 EXTENDED NETWORK MODEL

4.3.1 *Model details*

As an improvement of model S, we include the Onsager network model as introduced in section 3.1. Most importantly, we obtain a more realistic temperature evolution in time, allowing for continuous current injection. Furthermore, additional effects beside Joule heating are introduced. On the one hand, Peltier heating/cooling occurs at interfaces of different materials, which involves astonishing consequences as presented in the following. On the other hand, heat flow smears out hot spots, and internal temperature differences lead to additional currents due to Seebeck voltages.

For a given configuration, electrochemical potential μ_i and temperature T_i are derived for all particles i, as explained in section 3.1. After each integration it is checked whether the mobilization condition $T_i > T_m$ is fulfilled and if so, the same mechanisms as in model S are applied: particles become mobile, recrystallize, and as soon as percolation is interrupted, the upper electrode and particles connected to it are moved downwards. The temperature of a recrystallized particle is set slightly below T_m. The model extension requires new boundary conditions: The electrodes are kept at fixed temperatures T_{HB} and the current is flowing constantly through the sample. In the following, this model will be called model E. So far, the only heat sinks in

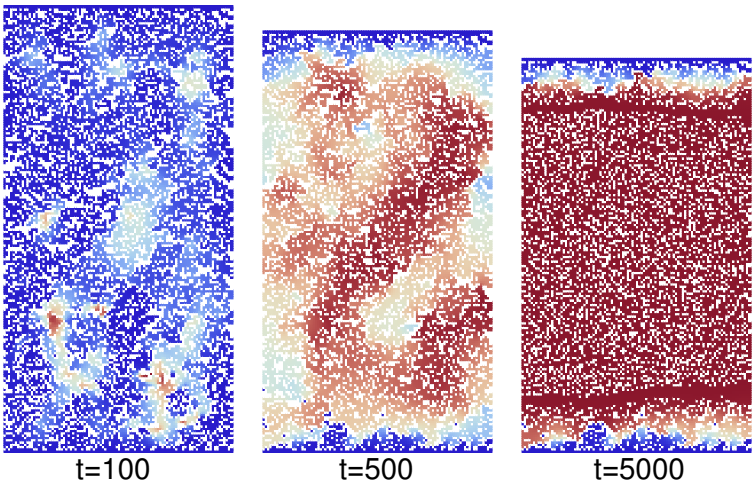

Figure 4.8: Temperature development with time in model E, where temperature increases from blue to red. As initial configuration we used a 100×200 system with density $\rho = 0.6$. The applied current is $I = 1$ and $K_{\text{env}} = 0$.

the model are the electrodes. However, it will turn out to be helpful to introduce further heat sinks. Therefore, we couple each particle to the environment at temperature T_{HB} via the heat conductance K_{env}.

In the present section, the particle diameter d, the heat conductance $K_{ij} = K = 1$, the specific heat $C_i = C = 1$, the electrical conductance $G_{ij} = G = 1$ and the environment temperature $T_{\text{HB}} = 1$ are used as natural units. In appendix B we show the derivation of all units necessary in this section. E. g. time is given in $[C/K]$ and the current in $[\sqrt{KGT_{\text{HB}}}]$.

Two important time scales should be mentioned: the time scale of heat exchange between neighboring sites $t_{\text{exc}} = C/K$ and the time scale on which the mobilization temperature is reached $t_{\text{heat}} = CG(T_m - T_{\text{HB}})/I^2$.

4.3.2 *Comparison between model S and model E*

For the following comparison we set $\alpha_i = 0$. At first we consider the temperature evolution of model E with $K_{\text{env}} = 0$ and $t_{\text{exc}}/t_{\text{heat}} = 1$ (see fig. 4.8). At the beginning, isolated hot spots are present, which are blurred with time, and finally, heat accumulates in the center. In 2d almost all particles are connected or have been connected to the percolating cluster after a few compaction steps. As a consequence, all particles inside the sample have reached a high temperature at $t = 5000$, and a notable temperature gradient occurs exclusively close to the electrodes. We find that almost all internal particles are mobile and move randomly. At this point, it is very unlikely that a cross section is depleted. Therefore, further compression is inhibited. We stress that this behavior is by no means expected to appear in an experiment. Too much heat would melt the particles completely, which

results in a loss of the nanostructure. We verified that the heat accumulation also occurs for $t_{\mathrm{exc}}/t_{\mathrm{heat}} = 0.1$, $t_{\mathrm{exc}}/t_{\mathrm{heat}} = 0.01$ and further system shapes. The cold, loose regions directly at the electrodes and the hot, loose internal region are separated by densified parts. Those emerge where heat flow and Joule heating balance each other at elevated density, such that temperatures do not exceed the threshold anymore once a certain density is reached.

With model E, the strong correlation between heat deposition and electric current, which are inherent to model S, appear just at the beginning of the process and eventually, the relation between density and conductivity becomes trivial: the larger ρ, the higher σ.

In order to compare the results of model S and model E we characterize their behavior by $\sigma(\rho)$. The data for model S are identical to those discussed in section 4.2.2. Regarding model E, we consider a 100×100 grid with an initial density of 0.6 and investigate the cases $K_{\mathrm{env}} = 0$ and $K_{\mathrm{env}} = 10$ with the parameters taken from table 3. For both models we varied T_m.

In fig. 4.9, we show $\sigma(\rho)$ for a time at which the characteristic behavior has evolved. Considering model S (blue line and circles), each circle represents different values of m, where in the lower left corner large m are located. Between $m = 12$ and $m = 8$, we recover the unexpected behavior discussed in section 4.2.2 as a region where σ decreases with increasing ρ. In contrast, model E (yellow line and diamonds) is characterized by monotonically increasing $\sigma(\rho)$. Each symbol (diamonds) corresponds to different mobilization temperatures.

By adding a coupling to the environment (red line and squares), the strong correlation between heat and current can be restored and model E produces a similar characteristic $\sigma(\rho)$ as the Schwesig model. We emphasize that especially in the increasing branch both models behave equally. As a reference, $\sigma(\rho)$ of random configurations is shown as well (black line). The configurations are created by placing $N = 6000$ particles on a square grid of dimensions $L_x = 100$ and L_y, which is adjusted to the given density. We observe that model S and model E with $K_{\mathrm{env}} = 10$ produce samples with enhanced conductivity at low densities $\rho \lesssim 0.7$ compared to random configurations. Large pores, present in the initial configuration, are amplified by the process until percolation is interrupted, which is followed by an extinction of large pores such that a configuration with reduced amount of large pores is created. However, with decreasing m or T_m, respectively, the process amplifies more than one pore, while usually

	K_{env}	N_{samples}	I
setup 1	0	16	1
setup 2	10	8	10

Table 3: Parameters used in the present section for the simulation of model E. The current is given in units of $[\sqrt{KGT_{\mathrm{HB}}}]$.

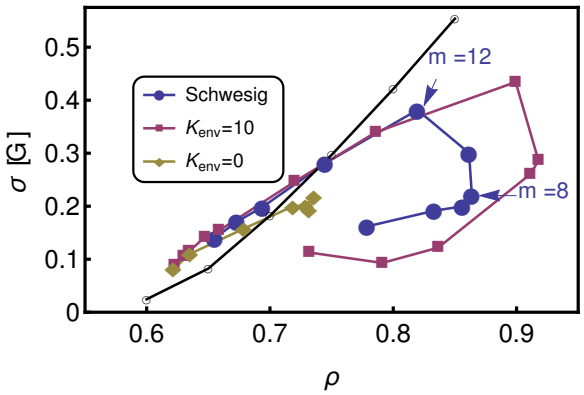

Figure 4.9: Plotting the conductivity against the density as a characteristic enables a comparison between the model S and model E. Each symbol represent another mobilization threshold m in the case of the model S and T_m for model E. The black line is derived using 100 random configurations for each data point.

one is removed in the compaction step and several remain implying a reduced conductivity.

4.3.3 *Self-organization in heterogeneous mixture*

Combining particles of different materials with CAPAD enables the creation of products with distinguished properties [87].

A simple estimation shows that in heterogeneous mixtures the interparticle Peltier effect may play an important role during CAPAD. The total current passing a sample with radius of 0.01 m is in the order of 1 kA leading to the current density $j \approx 3 \cdot 10^6\,\mathrm{A/m^2}$. With particle diameter $d = 50\,\mathrm{nm}$, contact area $\approx d^2$ and a specific conductivity $\sigma = 10^5\,\mathrm{S/m}$, the deposited Joule heating is in the order of $P_J \approx 10^{-14}\,\mathrm{W}$. At a temperature of 1000 K and with a Seebeck coefficient difference of $10^{-4}\,\mathrm{V/K}$ the Peltier heat at an interface amounts to $P_P \approx 10^{-9}\,\mathrm{W}$. We therefore expect the Peltier effect to be notable in a typical sample of good thermoelectric materials.

To visualize the impact of the Peltier effect, we simulate a binary mixture on a 200×200 square lattice with initial density $\rho = 0.6$. We use two different types of particles, with identical properties except the Seebeck coefficient. Natural units are the same as in section 4.3.2, and we set $T_m = 1.1$. The current $I = 1$ is flowing from bottom to top electrode (for units see appendix B). Now, we estimate the values of the current I and of the Seebeck coefficient α. We consider a good thermoelectric material with $\sigma = 10^5\,\mathrm{S/m}$ and $\kappa = 1\,\mathrm{W/K}$. Neglecting interface effects, we derive the electrical and heat conductance between neighboring particles as $G = \sigma d$ and $K = \kappa d$, with particle diameter d. For a temperature of 1000 K we conclude that the unit of the Seebeck coefficient is $[\alpha] = [K^{1/2}(T_{\mathrm{HB}}G)^{-1/2}] = 10^{-4}\,\mathrm{V/K}$. Similarly, we derive the unit of the electrical current $[I] = [(KGT_{\mathrm{HB}})^{1/2}] = 10^{-3}\,\mathrm{A}$, which corresponds to a rather high current density of $j \approx 10^8\,\mathrm{A/m^2}$. We observed the basic effects presented in the following as well with $I = 0.1$, although less pronounced. In-

tentionally, we applied a high current in order to highlight our observations. Note that the Peltier effect adds an additional timescale $t_{\text{pelt}} = C(T_m - T_{\text{HB}})/(\Delta\alpha I)$, representing the time to reach the mobilization temperature due to Peltier heating.

Snapshots of particle configurations are shown in fig. 4.10. Blue marked particles (B-particles) have $\alpha_B = 1$ and orange marked particles (O-particles) are characterized by $\alpha_O = 0$. The initial configuration is created by sequentially placing a particle B with probability $p_B = \rho/2$, a particle O with $p_O = \rho/2$ or a void with $p_V = 1 - \rho$ on each site.

While in the initial configuration particles are homogeneously distributed, we recognize a slight segregation at $t = 500$ (see fig. 4.10b). In the center, a strong intermixing of particles is observed, and some areas exhibit a checkerboard-like pattern (CBP), which will be quantified below. At $t = 2000$ the strength of segregation has increased even further (see fig. 4.10c) and is clearly visible. Particles with the higher Seebeck coefficient (blue) are located above the low Seebeck coefficient particles (orange). Taking into account the current flowing from the bottom to the top, we find that Peltier cooling occurs at the interface of the segregated areas. We checked that those patterns solely arise in mixtures with distinct Seebeck coefficients (see below) and can certainly attribute them to the interface Peltier effect.

This process of self-organization is driven by higher stability of resulting patterns, where stability is strongly related to temperature and local density, since particle movement requires exceeding the mobilization temperature and empty neighboring sites. The basic mechanism of the pattern evolution can be understood as follows: Due to the Peltier effect, particles constituting a O-B-interface in current direction are cooled, while B-O-interfaces are heated. B-B- or O-O-interfaces do not experience any interface Peltier effect. As a consequence, it is more likely that particles at an B-O-interface become mobile. The following motion is undirected, but if the next position is stable, the particle does not move back. However, in fig. 4.10c we still find regions with CBP, which suggests that the CBP is stable as well. Considering a minimal CBP, a B-particle surrounded by O-particles (or vice versa), and assuming isothermal conditions, we deduce that due to current conservation the Peltier heating and cooling at the four interfaces exactly neutralize each other. In our model, temperature differences across a single particle cannot be maintained and vanish quickly. Temperature differences between adjacent particles can be maintained, because the interface heat conductivity is believed to be much smaller than the particle heat conductivity. In general, temperatures in neighboring particles differ, leading to a net cooling or heating of the center particle in a CBP. As we will show below, cooled configurations are more likely. Starting from the initial, random configuration, the creation of a CBP allows to get rid of Peltier heating or may even lead to a cooling with very little particle restructuring.

Nonetheless, we recognize from fig. 4.10 that the extend of CBP decays in favor of segregation. To understand this, we discuss the influence of the Seebeck coefficient difference $\Delta\alpha = \alpha_B - \alpha_O = \alpha_B$ and

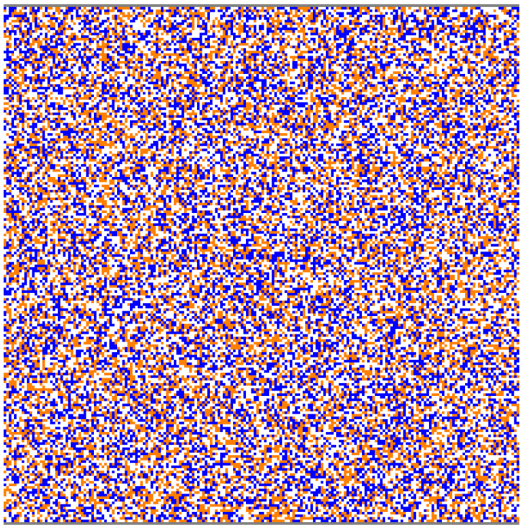

(a) $t = 0$

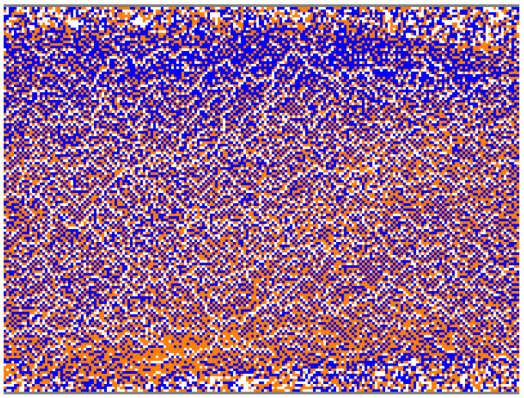

(b) $t = 500$

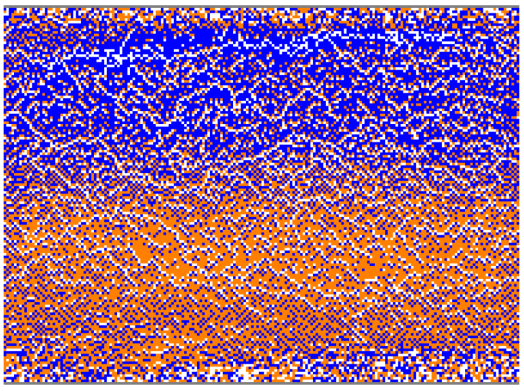

(c) $t = 2000$

Figure 4.10: Configurations of a CAPAD simulation with two different particle types, type B (blue) and type O (orange). We choose $\alpha_B = 1$ and $\alpha_O = 0$, while all other transport parameters are equal. The number of particles of type B and of type O are equal. The current I is flowing from the bottom to the top. Time is measured in units of [C/K].

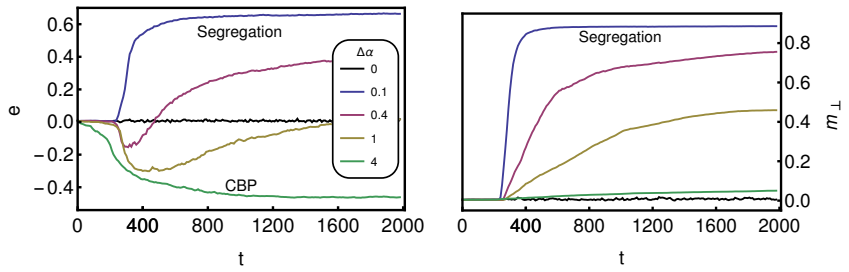

Figure 4.11: The left figure quantifies the strength of the CBP according to eq. (4.8). For large α_B the CBP occurs rapidly and is maintained for the whole simulation time, while for intermediate α_B the CBP vanishes with time. The right figure characterizes the segregation using eq. (4.9). For small α_B particles segregate rapidly, while for large α_B the process works much slower.

show that depending on $\Delta\alpha$ the self-organization leads to different configurations. It is useful to characterize the structure by two quantities originally defined in spin systems. Hence, we map all particles to spins, which can take two values $s_i = \pm 1$. O-particles are assigned to up spins ($s_i = 1$), B-particles to down spins ($s_i = -1$) and voids are not taken into consideration. The CBP is the ground state of the antiferromagnetic Ising model, and it is reasonable to characterize the extent of CBP by the energy per contact of the antiferromagnetic Ising model

$$e = \frac{1}{C} \sum_{\langle ij \rangle} s_i s_j, \tag{4.8}$$

where C corresponds to the number of contacts of a given configuration. The sum runs over all neighboring particles, where voids and electrodes are neglected. e measures the amount of contacts between different particle types, and equals -1, if all contacts are between distinct particle types. In contrast, e approaches 1 in a completely segregated configuration. Since e is not able to capture the orientation of the stripes, we introduce a second quantity to show that the orientation of the segregated areas is as indicated in fig. 4.10. Segregated configurations resemble the ground state of a driven lattice gas [115]. Hence, we use its order parameter as defined in [116]

$$m_\perp = \frac{1}{2} \sin\left(\frac{\pi}{L_y}\right) \left| \sum_{y=1}^{L_y} e^{2\pi i y / L_y} \frac{1}{N_x(y)} \sum_{x=1}^{L_x} s_{x,y} \right| \tag{4.9}$$

for characterization. L_x and L_y correspond to the dimensions of the sample and $N_x(y)$ is the number of particles in the row at position y.

In the initial configurations approximately half of the contacts are between equal and the other half between distinct particles such that $e(t = 0) \approx 0$ (see fig. 4.11, left) and $m_\perp(t = 0) \approx 0$ (see fig. 4.11, right). If both particles have the same Seebeck coefficient, here $\alpha_O = \alpha_B = 0$, none of the two patterns are created and $e(t > 0) \approx 0, m_\perp(t > 0) \approx 0$. For $\Delta\alpha \neq 0$, both quantities change significantly at $t \approx 220$ for all α_B except $\alpha_B = 4$, where strong Peltier heating leads to a faster decrease of e. Considering $\alpha_B < 4$, e drops first, but increases again, which

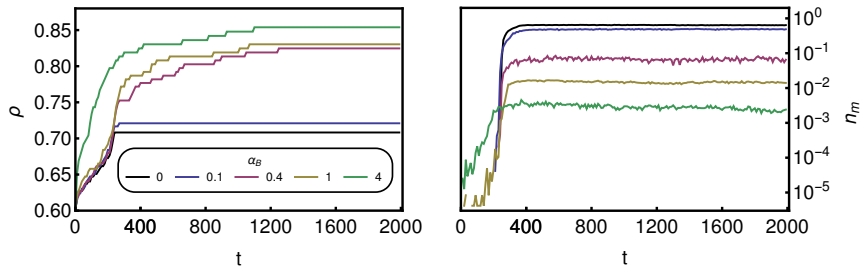

Figure 4.12: Density ρ (left) and amount of mobile particles n_m (right) in dependence of time for various α_B.

agrees well with the observations from the snapshots in fig. 4.10 ($\alpha_B = 1$). Figures 4.10 and 4.11 suggest that segregation zones and CBP occur simultaneously for intermediate α_B. Interestingly, the smallest and the largest Seebeck coefficient difference enable the fastest restructuring. An explanation of this observation is provided below. Concerning the stationarity of the configurations, it is reasonable to assume that the configuration for $\alpha_B = 0.1$ does not change further, while all other cases are in non-stationary state. However, we let a simulation with $\alpha_B = 4$ run up to $t = 40000$ and did not observe any further changes in e and $m_\perp$, suggesting that the CBP is stable.

In order to understand the pattern evolution, it is instructive to consider the time dependence of density ρ and the amount of mobile particles n_m (see fig. 4.12). In the beginning, two different behaviors are present: one strongly affected by Joule and the other by Peltier heating. For small Seebeck coefficients ($\alpha_B \lessapprox 1$), ρ and n_m coincide with the reference simulation ($\alpha_B = 0$). Although Joule heating prevails, the Peltier effect has a non-negligible impact on the densification as can be concluded from e and $m_\perp$. Considering large $\alpha_B = 4$, a Peltier-driven compaction is observed. Particles are mobilized rapidly due to the large Peltier effect, leading to a strong and fast densification at the beginning of the process. Peltier heated connections are unstable and vanish, but Peltier cooled contacts remain withdrawing heat from the sample, which keeps the total amount of mobile particles relatively small. In contrast, for small α_B (including $\alpha_B = 0$) the amount of mobile particles increases strongly, which inhibits a further compaction as discussed in section 4.3.2. However, low density permits high mobility allowing for rearrangement and segregation.

We underline the role of Peltier cooling by examining the mean heat per particle distinguishing between average Peltier heat $\overline{P}_p$ and average Joule heat $\overline{P}_j$. For each particle, we sum up the interface contributions, and average the results over all particles. Moreover, we take into account 10 different initial configurations. In fig. 4.13 (left), $\overline{P}_j$ and $-\overline{P}_p$ are depicted for $t = 2000$. The configuration arranges such that by averaging over all particles one obtains $\overline{P}_p < 0$. For large α_B, $\overline{P}_j$ and $-\overline{P}_p$ are of the same magnitude, which explains the low n_m. In combination with the high density, this prohibits further restructuring and CBP becomes a stationary pattern.

We already pointed out that for low α_B, rearrangement is enabled by low densities and large number of mobile particles. In order to

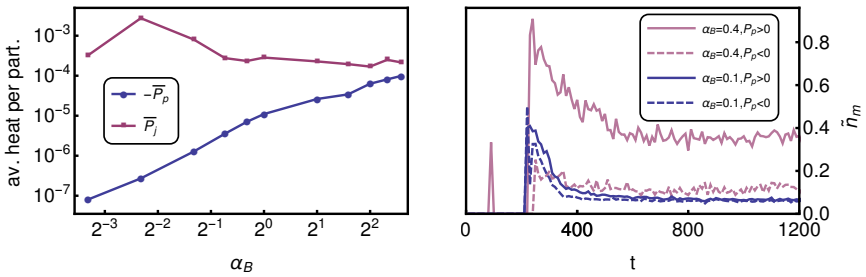

Figure 4.13: Average Joule heat per particle (red) and negative average Peltier heat per particle (blue) in dependence of α_B calculated at $t = 2000$ (left). On the right, the amount of mobile particles itemized according to the sign of Peltier heat is shown.

show that it is the Peltier effect, which triggers substantial configurational changes, we consider the relative amount of mobile particles $\tilde{n}_m$ classified according to the sign of $P_{p,i}$ (see fig. 4.13, right). This quantity is derived by counting the number of particles i for which $P_{p,i} > 0$ or $P_{p,i} < 0$ and dividing those by the total number of mobile particles. And indeed, even for very low $\alpha_B = 0.1$ there is a notable difference $\tilde{n}_m(P_p > 0) - \tilde{n}_m(P_p < 0) > 0$ in the time frame, where the restructuring takes place. After the strong segregation starting at $t \approx 300$ and accumulation of heat, the influence of Peltier heating vanishes and $\tilde{n}_m(P_p > 0) \approx \tilde{n}_m(P_p < 0)$. For larger α_B the influence of P_p remains after the slighter segregation. Although we pointed out similarities to the purely Joule-driven compaction, Peltier heating still triggers massive restructuring for low α_B.

To understand why CBP configurations vanish, we have to realize that high mobility leads to a variety of configurational changes, which influence the local heat production and heat currents. Those, in turn, affect particle temperatures and a cooled CBP configuration may turn into a heated one. Such a switching only ceases after segregation. For large α_B, CBP remains for two reasons: Configurational changes are less likely due to low n_m and the stronger cooling lead to lower temperatures such that a temporary switching to a heated CBP may not be sufficient to exceed T_m.

In this section, we explained the influence of the Peltier effect on particle configurations. The question arises, in how far strong particle mixing and segregation affect further quantities like conductivity and density.

4.3.4 *Peltier effect in unipolar samples*

Beside the Peltier effect inside a mixture, it has been pointed out by means of simulation and experiment that the Peltier effect at the electrode sample interface can have a significant impact on the compacted powder [74]. For metallic powders this effect is negligible, but for semiconductors with large Seebeck coefficients, high temperatures ($\approx 1000\,\mathrm{K}$) and current densities of several $\mathrm{kA/cm^2}$, the Peltier effect can reach more than 10% of the total Joule heat deposited in the sample [110].

Peltier heat is withdrawn from the interface on one side and deposited on the other. This can lead to strongly inhomogeneous samples [74]. Usually, the process is temperature controlled, while the temperature is in most cases measured at the top or bottom of the sample. This can just give an estimation for the internal temperature, but if the Peltier effect comes into play, this temperature is even more misleading.

To avoid Peltier heating/cooling one may use ac currents or electrodes made from a material with a Seebeck coefficient similar to the powder.

4.4 MOLECULAR DYNAMICS MODEL

The studies on CAPAD presented above revealed interesting effects, however, the underlying models incorporate several drawbacks: First of all, the unphysical motion bound to a lattice lacks any physical force and particles are allowed to diffuse through the system. Furthermore, the compaction criteria implicates that systems with large cross sections, which includes 3d systems, can hardly be simulated, because an interruption of percolation becomes unlikely.

A more realistic model shall be presented in this section. We combine the previously presented network model with a realistic particle motion based on the discrete element method (DEM), which is an accepted tool for the simulation of the behavior of nanopowders under external mechanical forces [117, 118].

Parts of the following work have been published in [109].

4.4.1 *Model details*

The particle motion is simulated by a modified version of the molecular dynamics code LAMMPS [119]. Each particle is presented by soft spheres (disks) with diameter d_i, mass m_i and the position of its center of mass $\mathbf{r}_i$. The particles trajectory is calculated numerically by solving $m_i\ddot{\mathbf{r}}_i = \sum_j \mathbf{F}_{ij}$ and $\dot{\mathbf{L}}_i = \sum_j \mathbf{M}_{ij}$, where j runs over all particles interacting with particle i and $\mathbf{F}_{ij}$, $\mathbf{M}_{ij}$ are the force and torque acting on contact ij. $\mathbf{L}_{ij}$ is the corresponding angular momentum.

A variety of complex and sophisticated contact models have been developed to account for various material properties (elastic, viscoelastic, elasto-plastic). Our aim is to study the influence of the temperature induced viscous motion of particles on the compaction of a powder. Hence, we restrict ourselves to the most basic contact model. The force F_{ij} is decomposed into a normal part F_n and a tangential part F_t with respect to the contact normal. F_n is given by a linear spring dashpot model [120] and a short-ranged attractive force. Being a function of the $\xi_{ij} = (d_i + d_j)/2 - \left|\mathbf{r}_i - \mathbf{r}_j\right|$ the normal force reads

$$F_n(\xi) = \begin{cases} -F_c(1 + \xi/d_0) & -d_0 \leq \xi < 0 \\ -F_c + \dot{\xi}\gamma_n + k_n\xi & \xi \geq 0 \end{cases} \tag{4.10}$$

with the maximal adhesion force F_c, the normal damping constant γ_n, the normal stiffness parameter k_n and the attraction range d_0 of the adhesion force. A finite elastic interaction enables Coulomb and rolling friction. Hence, sliding is suppressed as long as the Coulomb criterion $F_t \leq \mu_c |F_n + F_c|$ is satisfied. This is done by a linear spring dashpot as well (for details see [120]). Analogous laws hold for rolling and torsion resistance

We consider monodisperse packings, and as natural units we use the particle diameter d, the mass density ρ_{mass} of the particles, the maximal cohesion force F_c, the total current I flowing through the powder and the mobilization temperature T_m. The units of all derived quantities are specified in appendix B and will not be given explicitly in this section. Throughout this section we use the following parameters: The attraction range is $d_0 = 10^{-4}$, $k_t/k_n = 2/7$ with $k_n = 10^6$. To suppress microscopic oscillations, we set $\gamma_{\text{n/t}} = 2\sqrt{k_{n/t} m^*}$ with the reduced mass $m^* = m_i m_j/(m_i + m_j)$. The Coulomb friction coefficient is set to $\mu_c = 0.3$ for sticking and sliding and the rolling friction coefficient is set to $\mu_r = 0.3$.

Contacts with positive overlap are regarded as electrically and thermally conductive. Thus, we determine a network constituted by overlapping particles, where particle centers correspond to sites and contacts to bonds. Thermoelectric transport is described by the network model from section 3.1. However, in the following work we neglect Seebeck and Peltier effect by setting $\alpha_i = 0$. For simplicity, we assume that all particles have the same specific heat $C = C_i$, the same mobilization temperature T_m and that the conductances, $K_i = K$ and $G_i = G$ of all contacts are equal as well. Furthermore, all parameters are temperature independent. As in section 4.3, all particles are thermally coupled to the environment via K_{env}.

If a particle's temperature exceeds T_m a back coupling of the thermoelectric network on the force network occurs. Mobile particles are modeled by a vanishing Coulomb, rolling and torsion friction. In contrast to the network models, in the MD simulation all particles can move. Nevertheless, for consistency the term mobile denotes particles whose temperature exceed T_m. Since we assume very low relative particle velocities, a contribution of viscous friction is neglected here. Note that the temperature of a mobile particle is set slightly below T_m. Once, a mobile particle has lost enough heat by heat transport to its neighbors, such that the temperature decreases below the threshold T_m it freezes and friction mechanisms are re-established.

Uniaxial compaction is realized by a downwards moving piston (y-direction), driven by a constant stress p, while the position of the lower wall is fixed. The mass of the piston equals the total particle mass. The interaction law between wall and particle is the same as between particles. As walls also serve as electrode and heat bath, a cohesion force improves the coupling to the particles. Furthermore, we use periodic boundary conditions in the direction perpendicular to the piston motion (x-direction). As soon as the velocity of the piston drops below the threshold $v < v_c = 10^{-8}$ the simulation terminates.

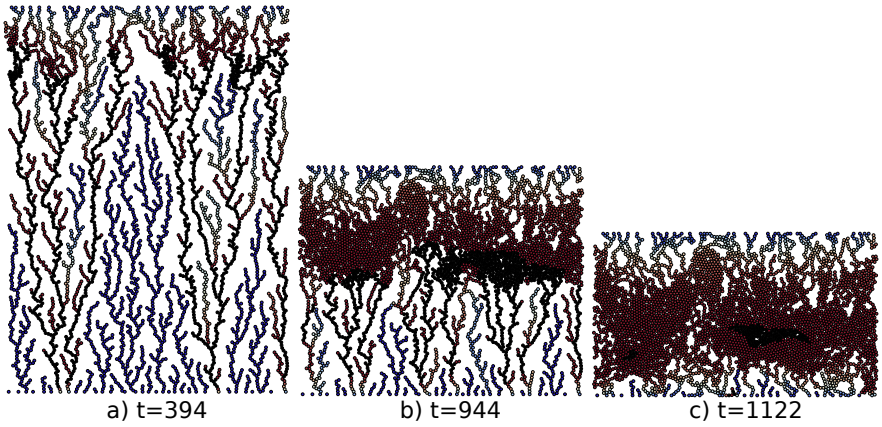

Figure 4.14: Snapshots of particle configuration at different time steps during a compaction process driven by a slight stress $p = 0.0064$. The left figure shows a configuration shortly after starting the simulation and the right configuration is taken shortly before terminating the simulation. The color represents particle temperatures, where the temperature increases from blue to red. Mobile particles are printed in black.

Due to structural changes the local potentials are time-dependent and they are recalculated each time the percolating cluster changes.

Beside the timescales specifying the thermal behavior ($t_{\text{th}} = C/K$ and $t_{\text{he}} = (CT_mG)/I^2$) two more time scales connected to the particle motion become important: the inertial time $t_i = \sqrt{m^*/(dp)}$ (in 2d) and the collision time $t_c = \sqrt{m^*/k_n}$.

4.4.2 *First results*

As a proof of concept, we compare the results of two different simulation setups: On the one hand, a ballistic deposit (BD) is used as initial configuration with $K_{\text{env}} = 0$ and a initial density $\rho_i = 0.22$, and on the other hand, a cluster-cluster aggregate (CCA) [121] serves as initial configuration with $K_{\text{env}} = K$ and $\rho_i = 0.45$.

We choose parameters, such that $t_{\text{th}} = 1$ ($C = 1$, $K = 1$), while the contact time is about $t_c \approx 10^{-3}$. To point out the effect of heating and mobilization, we varied the heating time via the electrical conductance G. Moreover, the electrode temperature is set to $T_{\text{HB}} = 0.5$

We start with considering particle and temperature distributions depicted in fig. 4.14 for a system consisting of $N = 4133$ particles, applied stress $p = 0.0064$ and $t_{\text{he}} = 1$ ($G = 1$) at different times of the compaction process. Especially in the beginning of the simulation, when tree like structures of the configuration are still present, mobile particles are most likely found in bottlenecks, carrying a large part of the current, but conducting heat poorly (see fig. 4.14a). Due to missing tangential forces, mobile particles are displaced and, being monodisperse, partly arrange in a crystalline structure. Apart from that, we observe a self-regulating mechanism resulting from the fact that dense regions are characterized by a high conductance leading more heat to the electrodes and producing less Joule heat per particle

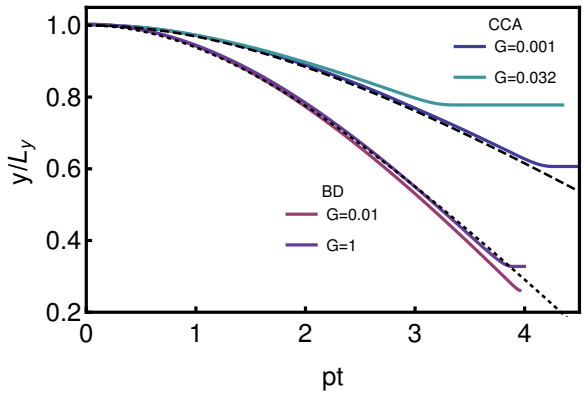

Figure 4.15: In the limit of small heating times, the piston position can be well described by eq. (4.11) (black, dotted and dashed lines) with $p_0 = 0$, although various system properties and parameters are different.

due to lower current density. The densification starts close to the upper electrode until the density is high enough to prevent further mobilization in this region. Thus, mobile particles and the strongest rearrangement of particles are found slightly below the dense region (see fig. 4.14b).

Although low pressures are applied, the snapshots fig. 4.14 exhibit strong similarities to shock compaction, which is characterized by a dense region close to the piston and an undensified region below [122]. Here, the particles very close to the piston do not exceed T_m such that a further loose region is located directly at the piston. Following the ideas presented in [122] we derive the time-dependence of the piston position (see appendix C) as

$$y(t) = L_y + \tilde{L} - \sqrt{\tilde{L}^2 + \frac{p - p_0}{\tilde{\rho}} t^2} \quad \text{with} \tag{4.11}$$

$$\tilde{L} = L_y \frac{\rho_d}{\rho_d + \rho_0} \quad \text{and} \quad \tilde{\rho} = \left(1 + \frac{\rho_0}{\rho_d}\right) \rho_0,$$

with the initial density ρ_0, the density of the compacted region ρ_d, which is assumed to be equal to the final density, and the consolidation pressure p_0 up to which the lower, uncompressed region can withstand an external stress. Particles in a force chain exposed to p are likely to conduct electrical current. For $t_{\mathrm{he}} \ll t_{\mathrm{th}}$ it is justified to assume that those particles become mobile. Having no tangential forces, mobile particles slide relative to each other even with infinitesimal external pressure as long as the density is low enough to provide space for the particle's motion. Under those circumstances the consolidation pressure is zero. Setting $p_0 = 0$ in eq. (4.11), a convincing agreement with simulation results is achieved (see fig. 4.15). Due to the low number of current carrying paths, the description of the BD works well even for $t_{\mathrm{th}} = t_{\mathrm{he}}$ ($G = 1$). Since all particles of the CCA are connected to the heat bath via K_{env}, lower electrical conductances are required to obtain large number of mobile particles. Note that the prediction of the piston velocity eq. (C.6) describes the simulation

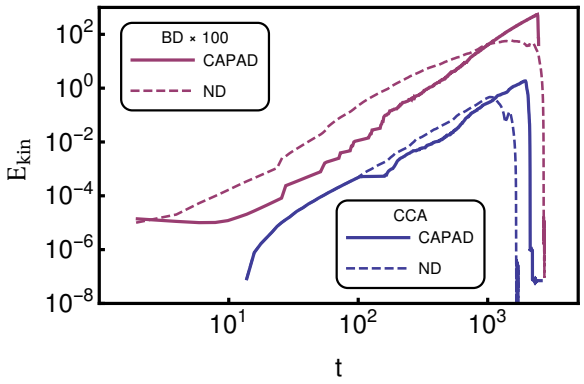

Figure 4.16: Comparison of the time dependency of kinetic energy E_{kin} for different piston pressure for CAPAD and normal densification (ND). For the BD we used $p = 0.0016$, $G = 0.01$ ($t_{\text{he}} = 0.01$) and for the CCA $p = 0.001$, $G = 0.001$ ($t_{\text{he}} = 0.001$).

results nicely. However, the simulation terminates prior to the regime of constant velocity.

Let us now discuss the agglomeration of particles close to the piston by means of the dimensionless pressure $\tilde{p} = (p - p_0)/p_0$. For $\tilde{p} \leq 0$, the powder is not compacted. If $\tilde{p} \ll 1$ and $\tilde{p} > 0$ are fulfilled, quasi-static compaction is enabled, while $\tilde{p} \gg 1$ evokes an impact compaction. Taking into account the vanishing consolidation pressure, we suppose that in a sufficiently mobilized structure always agglomeration of particles close to the piston occurs.

Next, we consider the time evolution of the total kinetic energy E_{kin} of the particles, which describes particle motion and the acceleration process. In fig. 4.16, we compare CAPAD and normal pressure-driven densification (ND) for pressures $p = 0.001$ and $p = 0.0016$ for CCA and BD, respectively. Both pressures alone just lead to weak compaction, while in combination with current, high densities can be reached. In general, the kinetic energy increases with time until final packing fraction is reached and particle motion stops. While the curve is smooth for ND, a stepwise increase of $E_{\text{kin}}(t)$ is found when CAPAD is applied. Steps are particularly pronounced for the BD (red), which can be identified with the onset of sliding of whole particle branches. This occurs, if mobilized particles far from the upper piston start to move and the cluster connected to it follows. In the beginning of the simulation, just a few mobile particles close to the piston are accelerated resulting in a reduced E_{kin} compared to ND, where whole branches are accelerated. For ND, the good force transmission related to the motion of particle chains, is promoted by the high rolling resistance [118]. In the much denser CCA configurations, steps of E_{kin} are smaller, but still notable.

Referring to the application of CAPAD to create nanostructured thermoelectric bulk material, we investigate the electrical conductivity σ. Note that the heat conductivity just differs by a factor determined by the bond conductances. Since σ affects the process itself it is instructive to consider the time dependence (see fig. 4.17). As a common feature of BD and CCA, we recognize that CAPAD implies

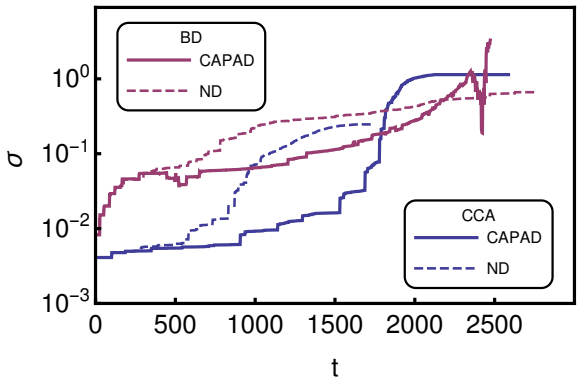

Figure 4.17: Electrical conductivity σ during the compaction process with CAPAD and as a comparison without mobilization (ND) for BD and CCA. For the BD we used $p = 0.0016$, $G = 0.01$ ($t_{\text{he}} = 0.01$) and for the CCA $p = 0.001$, $G = 0.001$ ($t_{\text{he}} = 0.001$).

a weaker increase of σ with time than ND. The strongest increase is observed, when the front of the densified region reaches the lower electrode, since σ is mainly dictated by the porous region. This general feature entails two beneficial consequences: First, for fixed current, more heat is inserted into the specimen, and second, the heat is mainly deposited in the porous region. For ND structural changes in terms of contact creations affect the whole system, leading to better interconnections, which is reflected by an elevated conductivity. Considering the final state, the higher density reached by CAPAD implies a higher conductivity compared to ND. In contrast to the network models, we found for both structures that the conductivity monotonically increases with the density.

Eventually, the influence of heat and pressure on the final configuration is studied using BD data. For this purpose, we vary the heating time by using different electrical conductances G. Fig. 4.18 shows the final density ρ_f for a broad range of loads p. Applying a current and mobilizing particles strongly reduces the consolidation pressure and leads to a much lower porosity. For small heating times ($t_{\text{he}} < 0.1$), particles are mobilized quickly, and although a small porosity is accompanied by an enhanced electrical/thermal conduction, a majority of particles are still mobile in final stages of the simulation. In combination with high loads $p \approx 10^{-1}$, the final density almost reaches the closest packing of monodisperse circles $\rho_{\text{cpd}} \approx 0.9$. The dependence of ρ_f on the applied load is weak for small t_{he}, since almost no stabilizing tangential forces act and even slight loads have a strong impact. Raising the heating time leads to enhanced final porosity as well as an enhanced influence of the applied pressure.

4.5 CONCLUSION

In this chapter we presented the evolution of a simulation model for current-activated pressure-assisted sintering in three steps.

The first two models provided thought-provoking impulses based on fundamental principles. In particular, we were interested in the

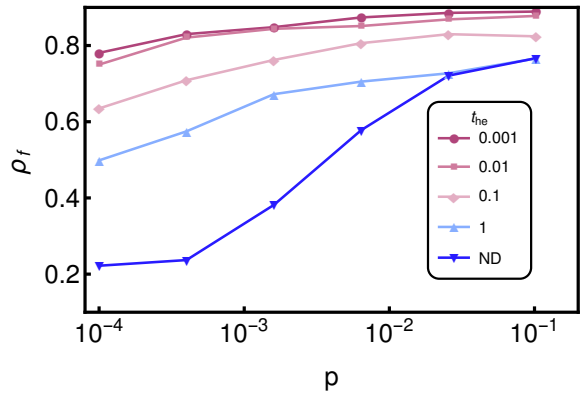

Figure 4.18: The final density ρ_f in dependence of the piston pressure p in a double-logarithmic plot for CAPAD and normal densification (ND) is shown.

effect of local heating controlled by the microstructure and on the interplay between both. A further point we worked out, is the effect of Peltier heating/cooling at particle interfaces in binary mixtures. A phenomenological model provides useful and interesting insights to the basic effects without disturbing influences. However, in doing so, we tolerate unphysical particle motion bounded to a lattice, ignore grain growth and atomic scale processes like segregation of oxides, for example. As a drawback, no direct comparison to real experiments nor the prediction of material parameters is possible.

Using model S we elaborated the intriguing effect of pores growing parallel to the electrodes implying that the highest conductivity derived from a ensemble average at a given time does not occur at the highest density. While those anticorrelations were explained before, we detected the importance of the time evolution between two compaction steps of a single sample as well as the effect of the temperature related parameter m. In contrast to previous results, we found out that predicting the occurrence of stationary states, meaning configurations in which current is well enough distributed, such that no mobilization occurs anymore, is not possible.

For model E, we included the Onsager network model into the CAPAD simulation model. This allows for a continuous current injection and a proper time evolution of the particle temperatures implying Fourier heat, Joule heat, Seebeck and Peltier effect. We found that the strong correlations between current and heat responsible for the results obtained with model S are blurred by the heat current to neighboring particles. Furthermore, heat accumulation inside the sample leads to a vast amount of mobile, randomly moving particles, which represents an unphysical behavior. However, the model allows us to investigate CAPAD with binary mixtures of two different particle species. We discovered an interesting effect of mixing or segregation depending on the Peltier coefficient difference of both materials. Within our model, the Peltier heat created at particle interfaces determines the stability of a local configuration. If the Peltier effect predominantly cools a particle, its position is more likely to be stable and vice versa. This basic effect together with the total amount of

mobile particles and the density determines, whether strong particle intermixing or segregation is observed.

As a final proof of principle, we combined molecular dynamics simulations and a network model in order to provide a proper particle motion. First simulations revealed a strong influence of local heating on the mechanical properties of a nanopowder and on the process itself.

5

HARMAN METHOD FOR INHOMOGENEOUS MATERIALS

The Harman method [123, 124] is a sophisticated and educative measurement technique allowing the determination of all three transport parameters σ, κ, α, and hence, the figure of merit zT within one single measurement procedure. It has been successfully applied to bulk material [125, 126], but is also used for the investigation of microstructured bulk material [127], thin films and superlattices [17, 128, 129, 130, 131].

First, we introduce the basic principles of the Harman method. Then, we investigate its applicability to segmented structures and binary particle mixtures by means of an analytical treatment and simulations.

The following chapter is mainly taken from [77].

5.1 HARMAN METHOD

The sample under investigation is connected to two leads on opposing sides, and in order to reduce heat losses the sample is placed into a vacuum chamber [132]. However, the leads also act as a connection to a heat bath with ambient temperature. A known dc current I is applied and the voltage across the sample U as well as the electrode temperatures are monitored over time. Due to Peltier heating at one electrode-sample boundary, cooling at the other and additional Joule heating, the temperatures at the electrodes change. After reaching a steady state, the current is switched off and the slower response time of the thermally induced Seebeck voltage is used to distinguish it from the resistive voltage. A typical time dependence of $U(t)$ is depicted in fig. 5.1 (blue line). Furthermore, the slower thermal response can be seen from the electrode temperatures (red), whose time dependence evolves almost symmetrically around the ambient temperature $T = 300\,\mathrm{K}$. Asymmetry is caused by the different Peltier coefficients, which depend on temperature.

Starting with a homogeneous temperature distribution the electrical conductance and the electrical conductivity can be determined from a measurement of the voltage U_σ (see fig. 5.1) via

$$G' = \frac{I}{U_\sigma}. \tag{5.1}$$

In the following, primed quantities represent Harman measurement results. In experiments, the measurement of G' might be difficult, as the Peltier effect and Joule heating immediately affect the temperature distribution [124]. Those problems can be circumvented by applying an ac current (eg. [132]). However, during the simulations we

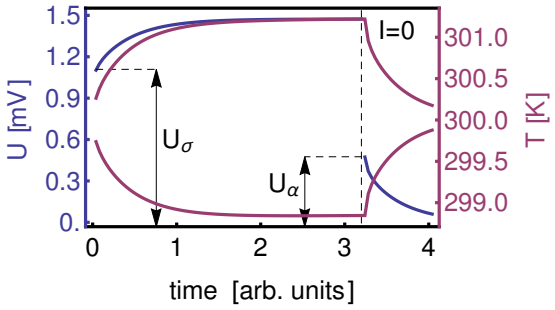

Figure 5.1: A simulated time dependence of the voltage between the electrodes and the electrode temperatures are shown. Parameters chosen for the simulation are taken from table 1

can avoid such a problem by recording U_σ before updating the temperatures. After switching off the current, the remaining temperature difference between the electrodes $\Delta T = T_L - T_0$ gives rise to a Seebeck voltage, which allows the determination of the Seebeck coefficient

$$\alpha' = -\frac{1}{q}\left(\frac{\mu_L - \mu_0}{T_L - T_0}\right) = \frac{U_\alpha}{\Delta T}, \tag{5.2}$$

where the index 0 reflects the position of the left electrode-sample interface, e. g. $T(0) = T_0$, and L represents the position of the right interface. From the energy balance condition in the steady state the total heat conductance is determined as

$$K' = \frac{\alpha'\overline{T} + (\bar{\mu} - \bar{\mu}_{\mathrm{env}})/q}{T_L - T_0} I - \frac{K_{\mathrm{env}}}{2}, \tag{5.3}$$

where K_{env} is the heat conductance between the heat bath and the electrodes. Quantities with bars are averages of the values at $x = 0$ and $x = L$, e. g. $\overline{T} = (T_0 + T_L)/2$. $\mu_{\mathrm{env},L}$ and $\mu_{\mathrm{env},0}$ correspond to the electrochemical potential in the lead at the electrode-sample interface. From eqs. (5.1) and (5.3) we obtain the effective conductivities $\kappa'_{\mathrm{eff}}, \sigma'_{\mathrm{eff}}$ determined with the Harman method.

Following the ideas of T. C. Harman [124], we recall the derivation of eq. (5.3). In the framework of the one-dimensional CPM the energy current $I_e = \mu I/q + I_q$ inside the sample at $x = 0$ reads

$$I_e(0) = \left(\alpha T_0 + \frac{\mu_0}{q}\right) I - K\left(T_L - T_0\right) - \frac{I^2}{2G} \tag{5.4}$$

and at $x = L$

$$I_e(L) = \left(\alpha T_L + \frac{\mu_L}{q}\right) I - K\left(T_L - T_0\right) + \frac{I^2}{2G}. \tag{5.5}$$

The energy currents in the lead at the electrode-sample interfaces are

$$I_{\mathrm{e,env}}(0) = \frac{\mu_{\mathrm{env},0}}{q} I - K_{\mathrm{env}}\left(T_0 - T_{\mathrm{HB}}\right) + \frac{I^2}{G_{\mathrm{env}}} \tag{5.6}$$

and

$$I_{\mathrm{e,env}}(L) = \frac{\mu_{\mathrm{env,L}}}{q} I - K_{\mathrm{env}}\left(T_{\mathrm{HB}} - T_L\right) - \frac{I^2}{G_{\mathrm{env}}}. \tag{5.7}$$

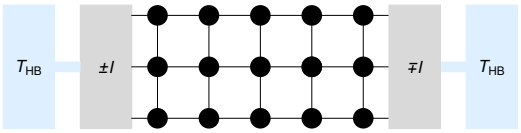

Figure 5.2: Two-dimensional example of the setup used to simulate the Harman method. The material grid is located between the electrodes, where the current I is injected or withdraw. The heat conductance K_{env} connects the electrodes to heat baths of temperature T_{HB}.

Equations (5.6) and (5.7) are obtained from CPM description of the leads assuming a vanishing Seebeck coefficient. G_{env} is the electrical conductance of the leads, which are assumed to be equal, just as the heat conductances K_{env}. Energy conservation requires equality of eq. (5.4) and eq. (5.6) as well as eq. (5.5) and eq. (5.7), and adding the resulting equations leads to eq. (5.3). In case K_{env} is unknown, the subtraction results in a second equation facilitating the derivation of K_{env}. $\bar{\mu} - \bar{\mu}_{env}$ represents the average contact potential differences between leads and sample, which can be neglected in the following simulations, since we do take a contact resistance into account. In experiments, additional losses via convection and heat radiation can be incorporated into eq. (5.3) via correction terms (e.g. [124, 133]).

A slow thermal relaxation time is required to properly measure the Seebeck voltage. Thus, it is useful to consider the limit $K_{env} \to 0$. Furthermore, assuming negligible contact resistance $\mu_0 - \mu_{env,0} = \mu_L - \mu_{env,L} = 0$, we obtain

$$\lim_{K_{env} \to 0} K' = \frac{\alpha I \bar{T}}{(T_L - T_0)}. \tag{5.8}$$

Hence, the figure of merit can simply be expressed by the quotient of Seebeck voltage and resistive voltage:

$$z = \frac{\alpha^2 G}{K} = \frac{U_\alpha}{U_\sigma \bar{T}}. \tag{5.9}$$

The simulation setup consists of a sample grid with attached electrodes and heat baths of temperature T_{HB} thermally connected to the electrodes via K_{env} (see fig. 5.2). Their temperatures develop according to eq. (3.13), where the connection to the heat bath solely allows for Fourier heat transport. The electrodes are characterized by the same transport parameters as the adjacent material. Thus, temperatures and potentials can be read off the electrode site without being influenced by electrode properties. Applying the Harman method to a CPM we found that electric conductivity σ', heat conductivity κ' and Seebeck coefficient α' of a homogeneous material measured with the Harman method exactly agree with the predefined values σ and α.

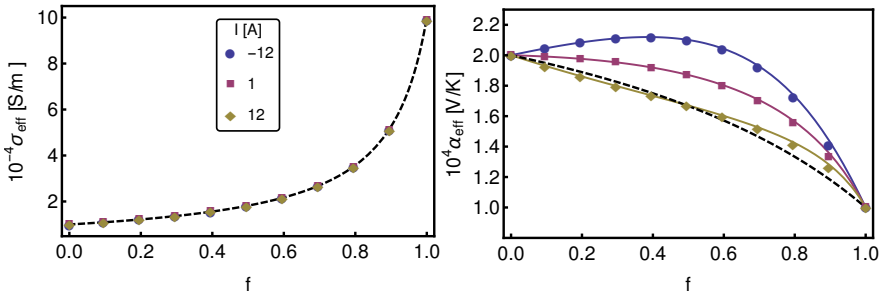

(a) electric conductivity

(b) Seebeck coefficient

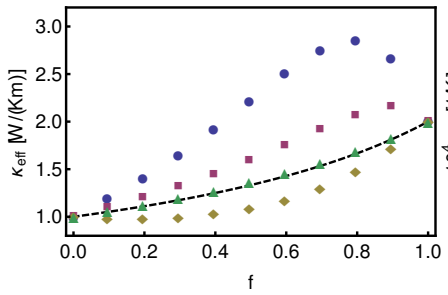

(c) heat conductivity

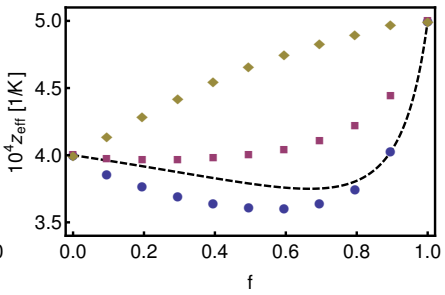

(d) figure of merit

Figure 5.3: The effective transport coefficients and the figure of merit z_{eff} in dependence of the fraction f of material A. $K_{\text{env}} = 0.01\,\text{W/K}$ is used for the simulation. The dashed lines represent the corresponding effective values eqs. (5.10) to (5.12), while the dots are simulation results obtained for different currents I. The solid lines in the upper right figure are analytic results discussed in the text. The green triangles in fig. 5.3c stem from eq. (5.16), a corrected equation for the Harman heat conductivity of segmented thermoelectrics.

5.2 HARMAN METHOD APPLIED TO SEGMENTED MATERIALS

A segmented TE as depicted in fig. 3.6 is used to present the basic problem of the Harman method when applied to inhomogeneous media. Therefore, we compare Harman method simulation results to analytic expressions of the transport coefficients.

In isothermal conditions, the electric conductivity can be derived as a connection in series

$$\sigma_{\text{eff}} = \frac{qjL}{\mu_0 - \mu_L} = \frac{\sigma_A \sigma_B}{\sigma_A(1-f) + \sigma_B f}, \tag{5.10}$$

where f represents the fraction consisting of material A.

Imposing open circuit conditions, $j = 0$, the effective heat conductivity is derived similarly to σ_{eff} as

$$\kappa_{\text{eff}} = \frac{j_q L}{T_0 - T_L} = \frac{\kappa_A \kappa_B}{\kappa_A(1-f) + \kappa_B f}. \tag{5.11}$$

and the Seebeck coefficient is defined as

$$\alpha_{\text{eff}} = -\frac{1}{q}\left(\frac{\mu_L - \mu_0}{T_L - T_0}\right) = \frac{\kappa_A(1-f)\alpha_B + \kappa_B f \alpha_A}{\kappa_A(1-f) + \kappa_B f}, \tag{5.12}$$

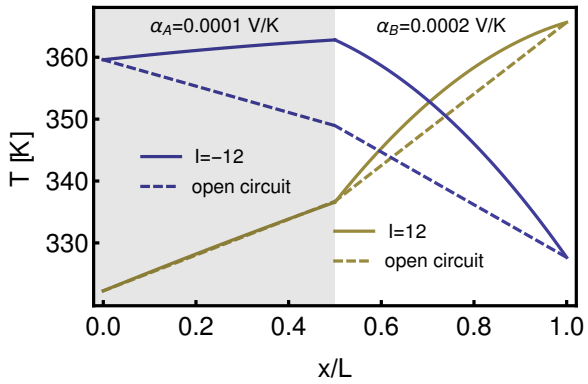

Figure 5.4: The figure shows the temperature distribution for $f = 0.5$, $I = -12\,\mathrm{A}$ (blue, solid line) and $I = 12\,\mathrm{A}$ (yellow, solid line). Additionally, the temperature distribution in open circuit conditions (dashed lines) with the same boundary temperatures are plotted.

which corresponds to a series connection of Seebeck voltages created from material A and B.

The simulation parameters are given in table 4, the dimensions of the cubic sample are $L = 0.01\,\mathrm{m}$ and the number of sites is $N_x = N = 100$. Moreover, we choose $K_{\mathrm{env}} = 0.01\,\mathrm{W/K}$ and $T_{\mathrm{HB}} = 300\,\mathrm{K}$. Fig. 5.3 shows a comparison between eqs. (5.10) to (5.12) and simulation results. As expected, the electric conductivity obtained by the Harman method coincides perfectly with eq. (5.10) (see fig. 5.3a). However, the Seebeck coefficient α'_{eff} (see fig. 5.3b), the heat conductivity κ'_{eff} (see fig. 5.3c) and z'_{eff} (see fig. 5.3d) depend on the current applied before measuring U_α and deviate strongly from the open circuit calculations. Just in the limiting cases $f \to 1$ and $f \to 0$ differences vanish. The differences between α'_{eff} and α_{eff} arise from the influence of the Peltier heating/cooling at the interface on the temperature distribution (see fig. 5.4). It causes the dependence of the temperatures $T_0, T_L, T(x_f) = T_{\mathrm{AB}}$ on the electrical current. Consequently, the thermopower

$$U_\alpha = \alpha_A \left(T_{\mathrm{AB}} - T_0\right) + \alpha_B \left(T_L - T_{\mathrm{AB}}\right) \tag{5.13}$$

is affected by the electrical current as well. Comparing the analytic temperature distributions $T(x)$ for $f = 1/2$ created by the external current $I = 12\,\mathrm{A}$ (yellow line) and $I = -12\,\mathrm{A}$ (blue line) to the respective open circuit distributions (dashed lines) with the same boundary temperatures, a much better agreement, particularly of the interface

	$\alpha[\mathrm{V/K}]$	$\sigma[\mathrm{S/m}]$	$\kappa[\mathrm{W/(Km)}]$
material A	$1 \cdot 10^{-4}$	10^5	2
material B	$2 \cdot 10^{-4}$	10^4	1

Table 4: The parameters used for the simulations of the Harman method applied to segmented thermoelectric material. The parameters are the same as in table 2 from chapter 3. Furthermore, we choose $K_{\mathrm{env}} = 0.01\,\mathrm{W/K}$ and $T_{\mathrm{HB}} = 300\,\mathrm{K}$.

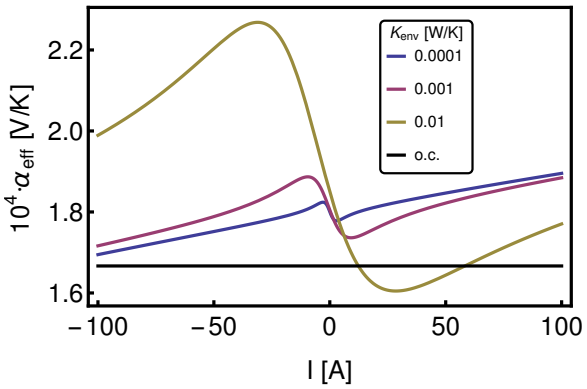

Figure 5.5: The Seebeck coefficients of an segmented thermoelectric material which consists of two equal sized parts ($f = 0.5$) measured by the Harman method and with open circuit conditions (black line). As the current approaches $I = 0$ the difference between Harman method result and true open circuit value does not vanish.

temperature T_{AB}, is found for $I = 12\,\mathrm{A}$. Here, Joule heating is nearly compensated by Peltier cooling. This explains why α'_{eff} and α_{eff} almost coincide for $I = 12\,\mathrm{A}$ at $f = 1/2$, while for $I = -12\,\mathrm{A}$ the Seebeck coefficient is strongly overestimated, since the larger temperature drop is across the material with the higher Seebeck coefficient.

Note that by using eq. (5.13) and applying analytically derived temperatures T_0, T_{AB}, T_L, we get an expression for the Seebeck coefficient measured by the Harman method (solid lines in fig. 5.3b), which coincide well with simulation results. The calculation of T_{AB} for fixed boundary temperatures is shown in section 3.2.2. A detailed calculation for arbitrary number of segments and with attached heat baths implying variable temperatures T_0 and T_L is presented in appendix A.

Although the Seebeck coefficient is measured at $I = 0$ when using the Harman method, it depends strongly on the previously applied electrical current (see fig. 5.5), since the temperature profile in inhomogeneous samples acts as a memory. Remarkably, even for arbitrarily small currents $|I|$ the Harman measurement gives a Seebeck coefficient which deviates from the true open circuit value. Note that the application of small currents correspond to the usual operation mode, which keeps the temperature difference between the electrodes small and reduces parasitic losses. In this limit, Joule heating is negligible as well as the influence of the temperature on the Peltier coefficient, such that the three interface temperatures depend linearly on the current. As a consequence, the relation between the temperature differences across material A and B becomes independent of I for $I \to 0$.

We elaborate this argument by calculating α'_{eff} analytically. For this purpose the temperature distribution $T(x)$ is derived as shown in appendix A and then fed into eq. (5.13). We expand the temperature distribution around $j = 0$, which leads to the compact expression

$$\alpha'_{eff} - \alpha_{eff} = \frac{(\alpha_A - \alpha_B)^2 (1-f) f (\kappa_{eff} + K_{env} L/(2S))}{\alpha_{eff}((1-f)\kappa_A + f\kappa_B)} + \mathcal{O}(j), \tag{5.14}$$

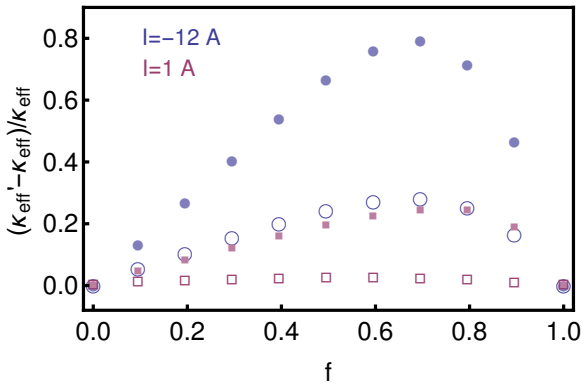

Figure 5.6: The relative deviation between the heat conductivity measured by the Harman method κ'_{eff} and the open circuit value κ_{eff} in dependence of f. The filled symbols are derived using the Seebeck coefficient determined by the Harman method and empty symbols are derived with the open circuit Seebeck coefficient eq. (5.2). Blue symbols are calculated for $I = -12\,\text{A}$ and red for $I = 1\,\text{A}$.

with the cross section area of the sample S. From eq. (5.14) we obtain that $\alpha'_{\text{eff}} = \alpha_{\text{eff}}$ for $f = 0$ and $f = 1$. Except those special cases, the numerator in eq. (5.14) is always positive, while the denominator has the same sign as α_{eff}. We conclude that in the limit of small electrical currents the Harman method systematically overestimates the absolute value of the effective Seebeck coefficient.

This overestimation is reflected by the heat conductance, which depends linearly on the Seebeck coefficient (see eq. (5.3)). But its influence is not sufficient to explain the relative deviations $(\kappa'_{\text{eff}} - \kappa_{\text{eff}})/\kappa_{\text{eff}}$ as indicated in fig. 5.6, where we show $\kappa'_{\text{eff}}(\alpha'_{\text{eff}})$ (filled symbols) and $\kappa'_{\text{eff}}(\alpha_{\text{eff}})$ (open symbols). For $I = -12\,\text{A}$ (blue) roughly a half of the deviation stems from α'_{eff}, while the other half originates from assuming a CPM for the calculation of eq. (5.3). For $I = 1\,\text{A}$ (red) the error is smaller and almost vanishes when using α_{eff} (red empty squares).

The latter agrees well with the result of the following calculation. We present a possibility to infer the true open circuit heat conductivity eq. (5.11) from the Harman method requiring α_{eff} , which can be obtained from Harman measurements using eq. (5.14). Therefore, we basically repeat the derivation of K' from section 5.1 for a double segment structure. The energy currents are determined at $x = 0$ and $x = L$ using the temperature distribution and its derivative as presented in eq. (3.22). The resulting energy currents are expanded to first order around $j = 0$ and their average reads

$$\bar{I}_e = \frac{K_{\text{env}}\alpha_{\text{eff}}T_{\text{HB}}jS}{2K + K_{\text{env}}} + \frac{\mu_0 + \mu_L}{2q}jS + \mathcal{O}(j^2) \tag{5.15}$$

Following the arguments of section 5.1 this must be equal to the average of eqs. (5.6) and (5.7), which leads to

$$\kappa'_{\text{eff}} = \frac{\alpha_{\text{eff}}T_{\text{HB}}L}{T_0 - T_L}j - \frac{K_{\text{env}}L}{2S} + \mathcal{O}(j), \tag{5.16}$$

where we have set $\mu_0 - \mu_{\text{env},0} = \mu_L - \mu_{\text{env},L} = 0$. Using T_0 and T_L explicitly in eqs. (5.6) and (5.7), but not in eq. (5.15) is not inconsistent

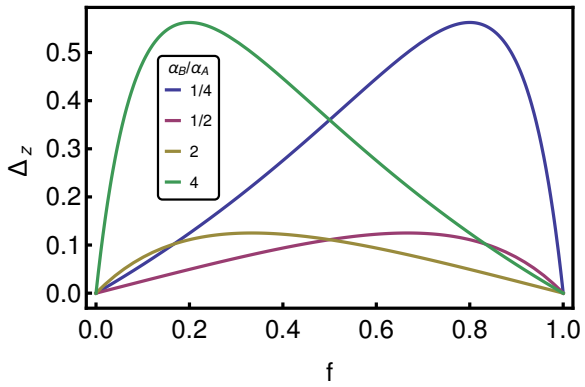

Figure 5.7: Δ_z in dependence of f for various α_B/α_A. We choose $\alpha_A = 0.0001\,\mathrm{V/K}$, $\sigma_A = 1.1 \cdot 10^5\,\mathrm{S/m}$,$\kappa_A = 1.2\,\mathrm{W/(Km)}$, $\sigma_B = 7 \cdot 10^4\,\mathrm{S/m}$ and $\kappa_B = 2\,\mathrm{W/(Km)}$.

at all. In fact, we avoid products of the form $(T_0 - T_{\mathrm{HB}})j$ or $(T_L - T_{\mathrm{HB}})j$, which are of second order in j, since $(T_0 - T_{\mathrm{HB}})$ and $(T_L - T_{\mathrm{HB}})$ scale with j. The application of eq. (5.16) leads to a satisfying agreement as shown by the green triangles in fig. 5.3c for $I = 1\,\mathrm{A}$.

Above discussed errors enter z'_{eff} (see fig. 5.3d) and for large currents z'_{eff} can be strongly over- or underestimated. We derive z'_{eff} using eqs. (5.10) and (5.14) and the heat conductivity from eq. (5.3) with α'_{eff}, which results in

$$z'_{\mathrm{eff}} - z_{\mathrm{eff}} = \frac{\alpha'^2_{\mathrm{eff}} - \alpha^2_{\mathrm{eff}} \frac{\kappa_{\mathrm{eff}}+\kappa_c}{\kappa_{\mathrm{eff}}}}{\kappa_{\mathrm{eff}} + \kappa_c} \sigma_{\mathrm{eff}} + \mathcal{O}(j), \tag{5.17}$$

with $\kappa_c = (\alpha'_{\mathrm{eff}} - \alpha_{\mathrm{eff}}) T_{\mathrm{HB}} j/(T_L - T_0)$. Considering the limit $K_{\mathrm{env}} \to 0$ leads to

$$z'_{\mathrm{eff}} - z_{\mathrm{eff}} = \frac{(\alpha_A - \alpha_B)^2 (1-f) f \sigma_{\mathrm{eff}}}{(1-f)\kappa_A + f\kappa_B} + \mathcal{O}(j) > 0. \tag{5.18}$$

In the limit of vanishing current and weak heat coupling to the environment the Harman method always overestimates the figure of merit. The relative deviation

$$\frac{z'_{\mathrm{eff}} - z_{\mathrm{eff}}}{z_{\mathrm{eff}}} = \Delta_z = \frac{(1-f) f \kappa_A \kappa_B \left(\alpha_A - \alpha_B\right)^2}{((1-f)\kappa_A \alpha_B + f \kappa_B \alpha_A)^2 + \mathcal{O}(j)}. \tag{5.19}$$

is affected by four material parameters and the ratio f. Figure 5.7 depicts how Δ_z depends on f and the Seebeck coefficients α_A and α_B. The position $f_{\max}$ of the maximum $\Delta_z(f_{\max})$ and its height strongly depend on α_B. The heat conductivities κ_A, κ_B just change the position $f_{\max}$ and the maximal deviation

$$\Delta_z(f_{\max}) = \frac{(\alpha_A - \alpha_B)^2}{4\alpha_A \alpha_B} \tag{5.20}$$

is independent of the heat conductivity. $\Delta_z(f_{\max})$ can become very large. E. g. for $\alpha_A = 4 \cdot 10^{-4}\,\mathrm{V/K}$ and $\alpha_B = 10^{-4}\,\mathrm{V/K}$ we find that $\Delta_z(f_{\max}) = 0.5625$ and the Harman method overestimates z_{eff} by 56.25%.

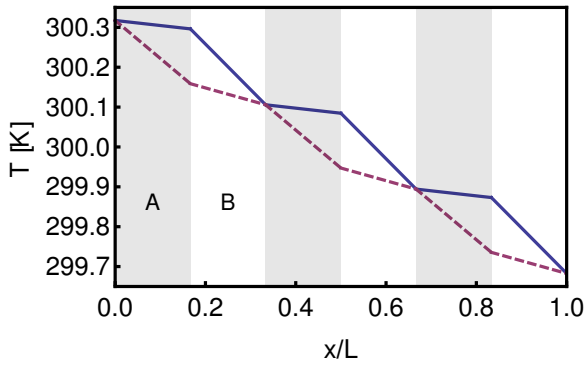

Figure 5.8: Temperature distribution in a superlattice consisting of six alternating layers A and B for open circuit conditions (red) and for a small current (blue).

Experimental hints for errors produced by the Harman method were found by M. A. Korzhuev and E. S. Avilov in segmented thermoelectrics [134]. They reported a change of the Harman figure of merit, when the cross section of one of two segments is reduced and related it to the change of the heat and electrical conductance in a segment, which affects the temperature drop across the segments.

We now argue that the above discussed errors occur in the experimentally more relevant superlattice systems consisting of hundreds of layers of alternating material. It is challenging to simulate a superlattice, since the error related to the approximation for a bond Seebeck coefficient increases with the number of interfaces. However, as shown in appendix A, the calculation for a structure consisting of two segments can easily be extended to n segments. Moreover, in the limit of $j \to 0$ and for even number of segments n, we are able to straightforwardly explain that the double segment equations are recovered. Therefore, let us first consider the temperature distribution for given $T_0 > T_L$ in open circuit conditions (see fig. 5.8). The temperature difference across each AB double segment equals $2(T_0 - T_L)/n$. This is true as well for the first order approximation around $j = 0$, which neglects Joule heating and temperature dependence of the interface Peltier effect. As a consequence, each double segment creates the same deviation from the open circuit Seebeck coefficient. This in turn equals the error of the whole superlattice, since the total voltage scales with the number of AB double segments, just as the total temperature difference. For odd numbers of segments, an additional correction term which vanishes as $1/n$ has to be taken into account.

Knowing α'_{eff} of a superlattice, we consider the Harman heat conductance. A superlattice and a double segmented structure with the same dimensions and made of the same material, are characterized by the same transport parameters. Then, measuring the heat conductivity according to (5.3) delivers an identical result, since α'_{eff} and the total temperature difference are equivalent. As a consequence eq. (5.20) holds for superlattices.

Superlattices attracted a lot of interest and a record $zT \approx 2.4$ was found in Bi_2Te_3/Sb_2Te_3 superlattices [17], which has not been repro-

duced so far. The individual segments are very thin: Bi_2Te_3 segments have a thickness of 1 nm and Sb_2Te_3 have a thickness of 5 nm implying $f = 1/6$. Neglecting quantum effects and using $\alpha_{BiTe} \approx 2.2 \cdot 10^{-4}\,V/K$ [59], $\alpha_{SbTe} \approx 0.9 \cdot 10^{-4}\,V/K$ [135], $\kappa_{BiTe} = 2\,W/mK$ [136] and $\kappa_{SbTe} = 1.8\,W/mK$ [136] results in $\Delta_z(1/6) = 0.18$ corresponding to 18% overestimation of the figure of merit. Note that this result is obtained by a phenomenological theory neglecting quantum and interface effects. Further examples for the application of the Harman method on superlattice structures with potential overestimation of zT can be found in [128, 129, 131].

5.3 HARMAN METHOD APPLIED TO COMPOSITE MATERIALS

Composite materials attract attention in the field of thermoelectrics and are believed to bear a huge potential for further improvements [41]. We discuss the application of the Harman method to random particle composites consisting of two distinct materials by comparing the Harman transport coefficients to the ones obtained under open circuit conditions and from an effective medium theory.

The composites are modeled by two-dimensional square grids and its sites are randomly occupied by metal-like particles A and by semiconductor-like particles B. Interface contributions as e. g. interface resistances are neglected. The fraction f of the metal-like material (A) is varied and for each f at least 10 different setups were averaged. Additionally, the setups are exposed to open circuit conditions with an applied temperature difference between the opposing electrodes in order to determine open circuit values. Parameters are taken from table 5 and the dimensions of the samples are $L = 0.01\,m$. Parameters for each bond connecting the electrode site with material sites are derived individually, namely such that the bond is always regarded as bond between sites of the same material. Thereby, we avoid to introduce additional electrode properties.

In contrast to a segmented thermoelectric, the number of interfaces between different materials is large and the error produced by the approximation eq. (3.9) becomes relevant. A first approach to improve the approximation, is to weight the Seebeck coefficients α_i and α_j with K_i and K_j according to

$$\alpha_{ij} = \frac{K_i\alpha_j + K_j\alpha_i}{K_i + K_j}, \tag{5.21}$$

	σ [S/m]	κ [W/K m]	α [V/T]
material A	$1.3 \cdot 10^5$	3	0.0001
material B	100	1	0.002

Table 5: The parameters used for the simulation represent a metal-like (A) and a semiconductor-like (B) material. The heat bath temperature is $T_{HB} = 300\,K$ and the applied electrical current is $I = 1\,A$.

which is similar to eq. (5.12) with $f = 1/2$. By doing so, we obtain a proper bond value for open circuit conditions. However, applying a small current would require a determination of α_{ij} according to eq. (5.14) or an even more complex expression to cover the case of large currents. This in turn is difficult, since we would have to solve Kirchhoff's law and eq. (5.14) self-consistently. Nonetheless, we checked the influence of eq. (5.21) and found an increase of α'_{eff} in the order of 13% in comparison to the application of eq. (5.12). The increase is caused by the distinct heat conductivities κ_A, κ_B. However, we keep eq. (3.10) for the following simulations as a lower approximation of the error.

An effective medium theory has been developed for the transport parameters in a two component composite. The effective electrical conductivity[1] is given by [137]

$$(1-f)\frac{\sigma_B^{1/t} - \sigma_{\text{eff}}^{1/t}}{\sigma_B^{1/t} + A\sigma_{\text{eff}}^{1/t}} + f\frac{\sigma_A^{1/t} - \sigma_{\text{eff}}^{1/t}}{\sigma_A^{1/t} + A\sigma_{\text{eff}}^{1/t}} = 0 \tag{5.22}$$

and an analogous equation holds for the heat conductivity. The parameter $A = (1 - f_c)/f_c$ is connected to the percolation threshold f_c. In another work [138], an equation for the Seebeck coefficient was derived, which reads

$$\alpha_{\text{eff}} = \alpha_B + (\alpha_A - \alpha_B)\,\frac{\kappa_{\text{eff}}/\sigma_{\text{eff}} - \kappa_B/\sigma_B}{\kappa_A/\sigma_A - \kappa_B/\sigma_B}. \tag{5.23}$$

This theory was confirmed in Al-Ge films [137] using effective medium theory eq. (5.22) for σ_{eff} and κ_{eff}. Equation (5.23) holds for segmented thermoelectrics as well, and inserting eqs. (5.10) and (5.11) in eq. (5.23) we obtain eq. (5.12).

As discussed before, the electrical conductivity can be determined accurately by the Harman method. Fitting eq. (5.22) to the simulation data enables the determination of $f_c = 0.594(2)$ and $t = 1.315(8)$. Note that f_c is close to the expected percolation threshold 0.592764 for site percolation on a square lattice. The effective medium theory expressions for σ_{eff} and κ_{eff} with the above fitting parameters are fed into eq. (5.23) and compared to the Harman method and open circuit conditions results.

The Seebeck coefficient α'_{eff} deviates strongly from open circuit conditions results and effective medium theory, especially below the percolation threshold (see fig. 5.9b). This phenomena can be understood by looking at the temperature and current distributions at the moment the Seebeck coefficient is measured. For $f = 0.8$, far from the percolation threshold, the temperature and current distribution appear homogeneous (see Fig. 5.10a) leading to a good match of the Harman and the open circuit measurements. In another sample at $f = 0.5$ (see Fig. 5.10b and 5.10c), however, a path of well conducting material A almost percolates, and thus, carries a majority of the current. In the region the path is interrupted by material B a strong

1 In this thesis, the index "eff" represents different composites of inhomogeneous materials.

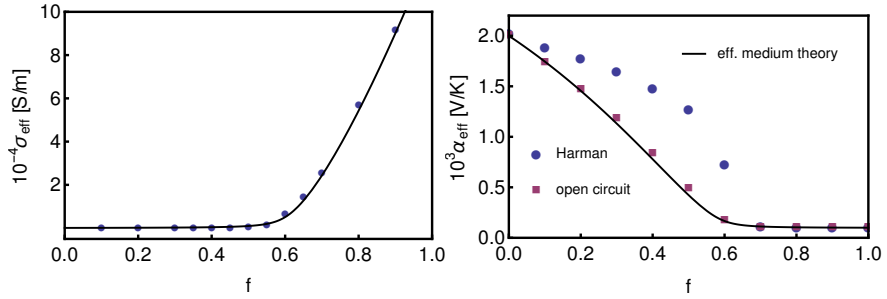

(a) electric conductivity

(b) Seebeck coefficient

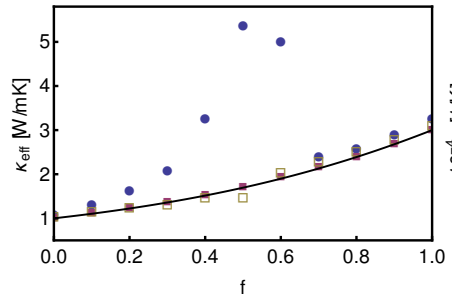

(c) heat conductivity

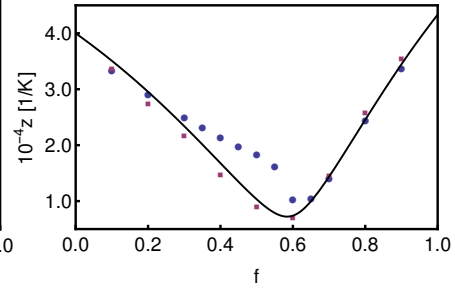

(d) figure of merit

Figure 5.9: The transport parameters in dependency of the fraction f of material A. The solid line always represents the corresponding analytic expression, while the dots are simulation results obtained by Harman method (blue) and open circuit measurements (red).

Peltier heating/cooling appears. This together with the inhomogeneous heat current generates a strongly inhomogeneous temperature and potential distribution. A big part of the temperature drop is located across material B, which is characterized by a higher $\alpha_B > \alpha_A$ resulting in an enhanced effective Seebeck coefficient determined by the Harman method close to the percolation threshold.

The heat conductivity (see fig. 5.9c) is severely affected by the overestimated Seebeck coefficient. Around the percolation threshold the Harman method delivers results up to three times larger than the true open circuit heat conductivity. By using the effective medium theory result, eq. (5.23), instead of the measured Seebeck coefficients, a rather good agreement to the open boundary conditions measurement is found (yellow squares in fig. 5.9c). We conclude that for small currents ($I = 1\,\text{A}$) a big part of the deviations $\kappa'_{\text{eff}} - \kappa_{\text{eff}}$ are caused by α'_{eff}.

5.4 CONCLUSION AND OUTLOOK

In this chapter we demonstrated that the Harman method applied to inhomogeneous media exhibit substantial systematic errors, which may easily exceed 100%. The errors are caused by the temperature distribution created by the required current and the related interface Peltier effect.

In order to understand the effect, we discussed a one-dimensional segmented material. We found out that an interesting self-organization

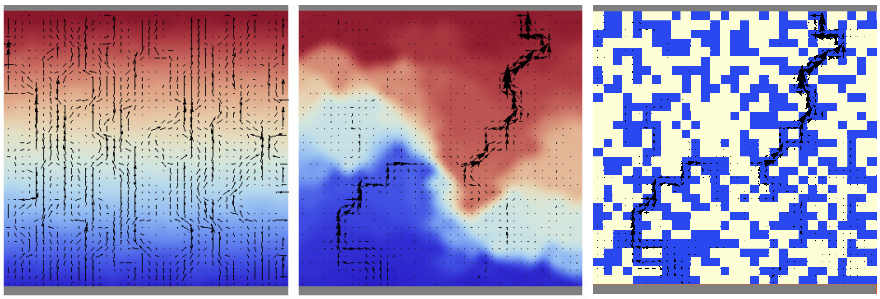

(a) $f = 0.8$ (b) $f = 0.5$ (c) $f = 0.5$

Figure 5.10: Temperature and current distribution close to ($f = 0.5$) and far from ($f = 0.8$) the percolation threshold for an example setup consisting of 40×40 lattice sites in a Harman setup at the moment of the Seebeck measurement. Temperature increases from blue to red. The electrodes are printed in gray, while the black arrows indicate the strength and the direction of the current. Fig. 5.10c shows the particle distribution and blue squares represent metal-like and yellow squares represent semiconductor-like material.

of the temperature distribution takes place. In comparison to open circuit conditions the temperature difference across the material with larger absolute Seebeck coefficient is increased, while it is decreased across the other segment. The temperature distribution is memorized until the voltage measurement and leads to an enhanced Seebeck coefficient. For segmented structures including superlattices we supported our observations by an analytical treatment and its results can be used as correction terms. The calculation shows that in the relevant limit of small currents and weak heat coupling to the environment, the absolute value of Seebeck coefficient and the figure of merit are always overestimated. Motivated by this fact one might get the idea that an enhancement of the thermopower can be observed in actual devices made of inhomogeneous media. But in fact, usually quite the opposite is true, as will be shown in chapter 6. An overestimated Seebeck coefficient causes an overestimation of the heat conductivity, as well. Nonetheless, for segmented structures we obtained a corrected Harman expression leading to the true open circuit heat conductivity. The same errors are recovered in two dimensional particle mixtures, which are solely accessible by simulations. Here, we considered semiconductor-metal composites, which exhibit strong inhomogeneities around the percolation threshold. The large difference between the respective Seebeck coefficients causes the strong deviations from the open circuit value. We conclude that applying the Harman method to inhomogeneous structures as done in e. g. [17, 128, 129, 131] is tricky, and the inhomogeneity of the sample has to be properly accounted for.

At this point we want to stress again that our analysis has been done using the phenomenological Onsager-de Groot-Callen theory, which does not resolve quantum effects. Moreover, it neglects the influence of the structure on the phonon contribution to the heat con-

ductivity. To what extent our findings can be recovered in small structures like superlattices with nm sized segments, is an open question.

Neglecting heat losses parallel to the current directions implies that a cross section is characterized by a constant temperature, which allows a one-dimensional description. However, in the experimental setup, heat losses/gains at the surface due to heat radiation are unavoidable. Already T. C. Harman showed that this heat leak should be taken into account when deriving the heat conductance [124]. Here we have to ask, whether the Seebeck voltage is affected by a radial temperate gradient. We assume that the ends of the sample are at constant temperatures T_h and T_c, while the environment temperate is somewhere in between (as assumed in Harman's calculation as well). It is clear that the Seebeck coefficient of a homogeneous sample is not affected by the heat leak at the surface. However, considering a segmented sample, we suppose that a lower surface temperature can reduce the strength of our observation: The interface temperature T_{AB} (causing the overestimation of the Seebeck coefficient) is affected by the interface Peltier effect and by heat radiation. If $T_{\mathrm{AB}} > T_{\mathrm{env}}$, heat radiation lowers T_{AB} at the surface and vice versa. In both cases, the strength of the observed overestimation might be reduced. We believe that this effect is negligible, especially if the sample is short compared to the cross sectional diameter. But clearly, this point deserves further investigations.

Finally, we comment on the neglect of interface resistances. If two distinct materials are joined, imperfection at the interface give rise to an interface heat resistance. But even at atomically perfect interfaces between two materials a thermal interface resistance exists, which is also called Kapitza resistance [139, 140]. It arises from a mismatch of phononic properties in both constituents. To give an idea of the effect of an interface layer, we performed additional calculations. Therefore, we considered an AiB structure, where i represents the interface segment, which has a low heat conductivity σ_q. If its thickness tends towards zero, we recover the Harman Seebeck coefficient of an AB structure eq. (5.14). However, the interface region gains influence as its thickness rises in comparison to the thickness of material A and B, respectively. Note that only the thermal boundary resistance influences the effective Seebeck coefficient, but not the electrical interface resistance.

6 INHOMOGENEOUS MATERIAL FOR DEVICES

In this chapter, we scrutinize the thermoelectric performance of two simple structures, segmented and parallel thermoelectrics. The enhanced thermopower discovered in the context of the Harman method (see chapter 5) inspires the work on segmented structures, while a new generator architecture (see chapter 7) exhibits similarities to a parallel assembly. First, we review recent accomplishments related to the efficiency improvement of inhomogeneous materials.

6.1 OVERVIEW

In a theoretical work Bergman and Levy proved that the figure of merit $z_{\text{eff}}T$ of an isotropic composite thermoelectric cannot exceed zT of the single components [138], which are assumed to be constant. On the other hand, the power factor $\alpha_{\text{eff}}^2\sigma_{\text{eff}}$, can become larger than both single component power factors [141]. When changing the fraction f of the material composition, it is reasonable to assume that $\alpha_{\text{eff}}(f)$ and $\sigma_{\text{eff}}(f)$ behave inversely. The product of those monotonic functions can have a maximum larger than the limiting values at $f = 0$ and $f = 1$. Neglecting interface effects, $\kappa_{\text{eff}}(f)$ and $\sigma_{\text{eff}}(f)$ change equally with f, such that their dependence on f cancels out in $z_{\text{eff}}T$ and a monotonic function proportional to $\alpha_{\text{eff}}^2(f)$ remains.

The temperature dependence of transport properties implies that each material can be employed most efficiently in a certain temperature range. For large temperature differences it is desirable to use segmented generators with optimal material properties in each segment [142, 21]. This concept is called functional grading, which is related to the concept of compatibility. Compatibility aims to give an understanding of thermoelectric processes from a local point of view. It was developed by Snyder and Ursell [143, 142] and recently attracted interest, especially in connection with optimal thermoelectric coolers [68, 144, 145, 146]. Snyder and Ursell emphasized the importance of the compatibility factor (here for a generator)

$$s = \frac{\sqrt{1+zT}-1}{\alpha T} \tag{6.1}$$

as a second quantity, beside zT, to characterize thermoelectrics. s follows from the local efficiency of an infinitesimal segment of length dx [142, 32]

$$\eta_{\text{loc}} = \frac{\mathrm{d}T}{T}\eta_r \tag{6.2}$$

with the local Carnot factor $\mathrm{d}T/T$ and the reduced efficiency

$$\eta_r = \frac{(\alpha - u\kappa/\sigma)u}{\alpha u + 1/T} \tag{6.3}$$

which is written in terms of the relative current density

$$u = -\frac{j}{\kappa \partial_x T}. \tag{6.4}$$

Now, for $u = s$ eq. (6.3) is maximized. Note that s depends on x even for constant transport parameters $s = s(x)$. If $u(x)$ differs significantly from $s(x)$, then the thermoelectric material is not working efficiently at x. Applying this concept to a segmented structure, it was pointed out that s of both materials should not differ by more than a factor of 2 [143]. Even for a single material leg it is desirable to run it such that $u = s$ is fulfilled at each point, which is denoted as self-compatibility. Therefore it is mandatory to develop materials with distinct function $\alpha(T)$, which is obtained by writing the heat production, eq. (2.34), in terms of u under the condition that $u = s$. The resulting differential equation can be solved for $z = \text{const}$ and $zT = \text{const}$ [142, 68].

Subsequently, it was shown that a self-compatible cooler, for which s slightly differs from eq. (6.1), outperforms a CPM cooler with the same $z = \text{const}$ [68]. Not only does a self-compatible cooler work much more efficiently, but it also reaches larger temperature differences. In fact, the temperature difference is not limited, since $\varphi(u = s) > 0$ for all ΔT. Its great performance is evoked by the Thomson effect, where the Peltier effect is responsible for cooling in a CPM device. Similar results were found for constant zT material [144].

It turns out that the efficiency of a generator does not profit from self-compatibility to the same degree as the cooler does [147]. This can be seen from optimal $\alpha(T)$ derived for $z = \text{const}$ and $zT = \text{const}$, which solely exhibit weak deviations from constant transport parameters.

6.2 SEGMENTED THERMOELECTRICS

Let us consider a double segment consisting of material A and B as depicted in fig. 3.6. Applying the Harman method to such a structure, we find that the imposed current creates a current dependent, and in comparison to open circuit conditions, enhanced Seebeck voltage. We now ask, whether this enhancement can be recovered in a generator, which would lead to an increased performance. The answer is not obvious, because of a fundamental difference between generator and Harman setup: The current in a generator is created by a temperature difference, where during the Harman method an imposed current causes a temperature gradient.

We compare the actual electric power P'_{eff} generated by a segmented single leg with the power one would expect from a generator with the effective parameters eqs. (5.10) and (5.12), which reads

$$P_{\text{eff}} = \alpha_{\text{eff}}(T_0 - T_L)I - I^2 \frac{L}{\sigma_{\text{eff}} S}, \tag{6.5}$$

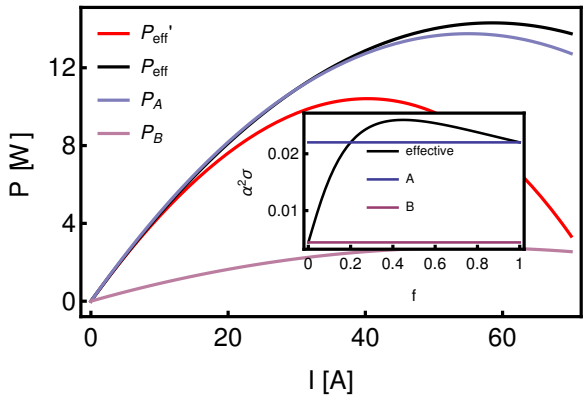

Figure 6.1: The electrical power for several materials: P'_{eff} refers to the actual power of a double segmented thermoelectric, while P_{eff} is expected from the respective effective material parameters. P_A and P_B correspond to the power created by a generator made of material A and B, respectively. The inset shows the power factor of material A,B and the effective power factor of a segmented composition of both.

with the length of the leg L, the cross-section area S and the boundary temperatures $T(0) = T_0$ and $T(L) = T_L$. To derive $P'_{\text{eff}} = UI$, the voltage is calculated from

$$\frac{\partial_x \mu}{q} = -\frac{j}{\sigma(x)} - \alpha(x)\partial_x T, \tag{6.6}$$

with step-wise functions $\alpha(x)$ and $\sigma(x)$. Integrating along the leg leads to

$$\begin{aligned} U &= \frac{\mu_L - \mu_0}{q} \\ &= -\frac{jfL}{\sigma_A} - \alpha_A(T_{\text{AB}} - T_0) - \frac{jL(1-f)}{\sigma_B} - \alpha_B(T_L - T_{\text{AB}}), \end{aligned} \tag{6.7}$$

where the interface temperature T_{AB} is derived as described in section 3.2.2. Note that due to large ΔT the first order approximation used previously, cannot be applied in the context of a generator. Exemplarily, in fig. 6.1 we show the power P_{eff} and P'_{eff} for $f = 0.9$ together with single material generator power P_A and P_B (parameters are taken from table 6). Two interesting information can be obtained from the figure. First, we recognize that P_{eff} is larger than P_A and P_B, which is due to the previously mentioned fact that the effective power factor (see inset of fig. 6.1) can be larger than those of the single materials. Second, P'_{eff} is significantly smaller than P_{eff}. This is an important result, because P_{eff} is the quantity one would expect after correctly measuring effective coefficients of the segmented material. But instead of P_{eff}, the much lower P'_{eff} is delivered by the generator. As we will explain below, the temperature distribution, depicted for maximal power in fig. 6.2, is responsible for the power reduction. The electrical current I is flowing from hot to cold and heating the AB interface due to different Peltier coefficients (blue line). As a consequence, the temperature drop across material A with $\alpha_A > \alpha_B > 0$

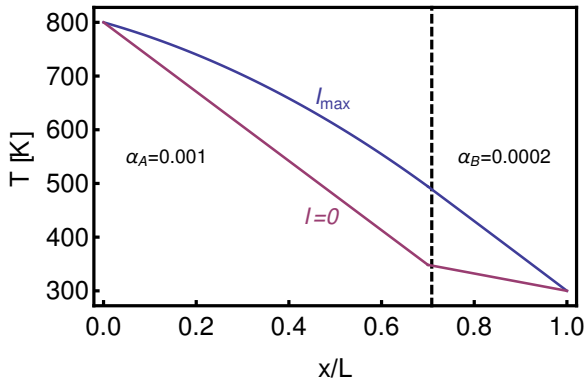

Figure 6.2: Temperature distribution of a segmented generator made from material A and B (see table 6) with $f = 0.7$ operated at maximum power output (blue). As a comparison the open circuit temperature distribution is plotted (red), which leads to α_{eff}.

is reduced in comparison to the open circuit temperature profile (red line) from which α_{eff} is determined. Accordingly, the Seebeck voltage of the AB generator is smaller than the one of a generator made by a homogeneous material with the same effective transport coefficients. The reduction is intrinsic to the generator mode and is not simply avoided by a change of the configuration. Exchanging the order of material A and B is accompanied by a Peltier cooled interface, which again lowers the temperature difference across material A. The argumentation holds for n-type segments as well. As an example, we consider $T_0 > T_L$ and $0 > \alpha_B > \alpha_A$. The electrical current is flowing from $x = L$ to $x = 0$ and heats the interface such that the temperature drop across material A is decreased, which is characterized by the higher absolute Seebeck coefficient. Taking solely Peltier cooling/heating into consideration we find $P'_{\text{eff}} < P_{\text{eff}}$.

Now, we demonstrate exemplarily for p-type material that $P'_{\text{eff}} > P_{\text{eff}}$ can be realized in a small parameter range. Therefore we expand $P'_{\text{eff}} - P_{\text{eff}}$ to first order around $f \to 0$ and $f \to 1$ at maximal current density, which is approximated by

$$j_{\text{max,eff}} = \frac{\alpha_{\text{eff}}(T_0 - T_L)\sigma_{\text{eff}}}{2L}, \tag{6.8}$$

	σ [S/m]	κ [W/(K m)]	α [V/T]
material A	10^4	0.5	0.001
material B	10^5	2	0.0002

Table 6: Parameter used for the simulation of segmented generators. The temperatures of the heat bathes are set to $T_0 = 800\,\text{K}$ on the hot and $T_L = 300\,\text{K}$ on the cold side. The dimension of the cubic generator leg is $L = 0.01\,\text{m}$.

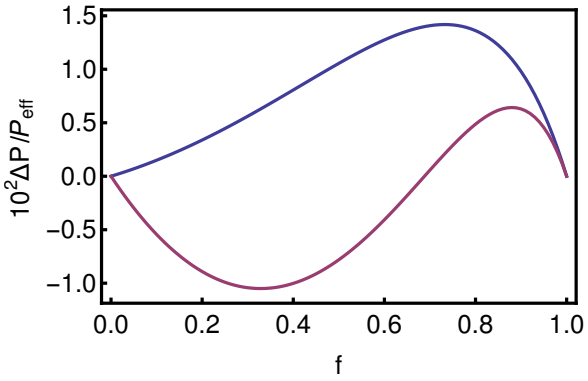

Figure 6.3: The relative power enhancement of a segmented generator, where both conditions, eqs. (6.11) and (6.12), are fulfilled for the blue curve. For the red curve $\Delta P > 0$ at $f \to 1$ and $\Delta P < 0$ at $f \to 0$.

the maximal current density of P_{eff}. The expansion around $f = 1$ reads

$$\begin{aligned}\Delta P &= P'_{\text{eff}} - P_{\text{eff}} \\ &= (1-f) S \sigma_A^2 \alpha_A^2 \Delta\alpha \Delta T^2 \frac{4\alpha_B T_L - \alpha_A (T_0 + 3T_L)}{16 \kappa_B L} + \mathcal{O}((1-f)^2)\end{aligned} \tag{6.9}$$

and for the expansion around $f = 0$ we get

$$\begin{aligned}\Delta P &= P'_{\text{eff}} - P_{\text{eff}} \\ &= f S \sigma_B^2 \alpha_B^2 \Delta\alpha \Delta T^2 \frac{\alpha_B (3T_0 + T_L) - 4\alpha_A T_0}{16 \kappa_A L} + \mathcal{O}(f^2)\end{aligned} \tag{6.10}$$

with $\Delta T = T_0 - T_L$ and $\Delta\alpha = \alpha_A - \alpha_B$. Requiring $\Delta P > 0$, we obtain from eqs. (6.9) and (6.10) the conditions

$$\frac{4T_L}{T_0 + 3T_L} \alpha_B < \alpha_A < \alpha_B \quad \text{for} \quad f \to 1 \tag{6.11}$$

$$\frac{3T_0 + T_L}{4T_0} \alpha_B < \alpha_A < \alpha_B \quad \text{for} \quad f \to 0. \tag{6.12}$$

Note that for $T_0 - T_L < 0$ or n-type material the relations read slightly different. For all parameter sets leading to $\Delta P > 0$, Peltier cooling occurs at the interface, which is overcompensated by Joule heating and Fourier heat, such that T_{AB} is elevated compared to open circuit conditions (see fig. 6.4). Notably, the conditions eqs. (6.11) and (6.12) are independent of the conductivities.

Choosing α_A according to eqs. (6.11) and (6.12) and deriving P'_{eff} close to $f = 1$ or $f = 0$, small enhancements $\Delta P / P_{\text{eff}} \approx 1\%$ can be found for the parameters shown in table 7. Equations (6.9) and (6.10) elucidate that the relative enhancement can be larger for material with better thermoelectric performances (large Seebeck coefficients, large electrical conductivities and small heat conductivities).

Now, we investigate in how far the conditions hold for intermediate f. Therefore, we use material parameters from table 7, for

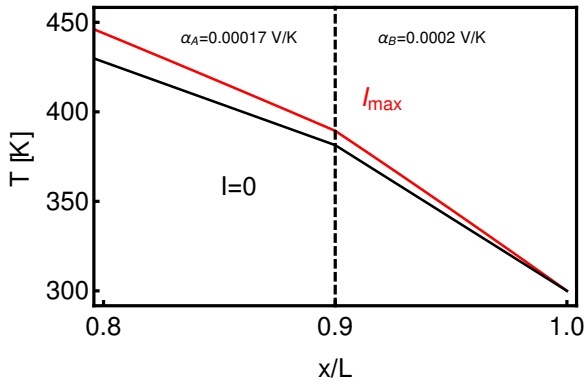

Figure 6.4: Temperature distribution around the interface for $\Delta P > 0$. Although the interface is cooled by the Peltier effect, Joule heating and Fourier heat increase the interface temperature such that the temperature drop across the material with the larger Seebeck coefficient is enhanced. Parameters are taken from table 7.

which the maximal effective power factor is larger than the maximal power factor of its constituents. If we choose α_A such that it obeys both, eqs. (6.11) and (6.12), the relative enhancement $\Delta P/P_{\text{eff}}$ is maximized for an intermediate $f \approx 0.7$ (see fig. 6.3, blue line). Although eqs. (6.11) and (6.12) are obtained from special cases they keep their validity for intermediate f (at least for the applied parameters). We also choose α_A such that at $f \to 1$ an enhancement is obtained, while for $f \to 0$ $\Delta P < 0$ (red line).

Finally, we briefly comment on the efficiency. Detecting an improved power may also lead to a better efficiency and using parameters from table 7, we also find a slightly enhanced efficiency $\eta'_{\text{eff}} > \eta_{\text{eff}}$ (see fig. 6.5). Additionally, we derived the efficiency of self-compatible material [147]

$$\eta_{\text{sc}} = 1 - \frac{(1+\sqrt{1+z_{\text{eff}}T_L})^2}{(1+\sqrt{1+z_{\text{eff}}T_0})^2} \exp\left(\frac{2(1-\sqrt{1+z_{\text{eff}}T_0})}{zT_0} - \frac{2(\sqrt{1+z_{\text{eff}}T_L}-1)}{z_{\text{eff}}T_L}\right). \tag{6.13}$$

Interestingly, we find $\eta_{\text{sc}} < \eta'_{\text{eff}}$, which is caused by the fact that the electrical current in subtly arranged segmented thermoelectrics leads to $z'_{\text{eff}} > z_{\text{eff}}$.

In a recent publication, the same system was investigated by analytic means under the assumption of negligible Joule heating, which led to compact expressions of power output and figure of merit [148]. It was also stressed that the output voltage is lowered by the fact that

	σ [S/m]	κ [W/(K m)]	α [V/T]
material A	$1.8 \cdot 10^5$	1.4	0.00017(blue)/0.00015(red)
material B	$1.2 \cdot 10^5$	0.8	0.0002

Table 7: Parameters, which yield an enhanced power output and efficiency in comparison to the expected open circuit values.

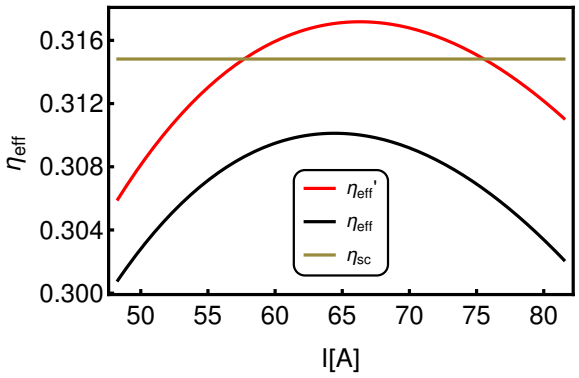

Figure 6.5: The real efficiency of a segmented leg η'_{eff} and the expected efficiency η_{eff}. Parameters are taken from table 7. Additionally, the maximal efficiency of a self-compatible material with z_{eff} is indicated (yellow line).

the temperature difference across the material with the lower Seebeck coefficient is amplified by the electric current. This is reflected by reduced power and figure of merit. A possible enhancement of power and efficiency is not observed in their model. However, an efficiency increase in a segmented system beyond the efficiencies of its constituents was report in another recent publication [149]. Their analytic model accounted for all effects, and Yang et al. derived optimally matched parameters for a given BiTe material leading to $\approx 1\%$ efficiency increase.

In the present work we added new insight to the problem in the form of a simple condition for the Seebeck coefficients and boundary temperature yielding a higher power and explained the origin of the deviations.

6.3 PARALLEL THERMOELECTRICS

Instead of stacking two segments on top of each other, here we consider a parallel arrangement shown in fig. 6.6. We are particularly interested in such a structure due to its similarities to a new generator configuration (see chapter 7), where the p- and n-type legs are directly put together. In contrast to the pn generator, electrodes are located at the hot and cold side, where in the generator configuration electrodes are solely connected to the cold side.

Similar analysis have recently been published (e. g. [150, 151, 152]). However, some new aspects are presented, which are motivated by a comparison between analytic results and simulation.

We first derive the electrical power of the structure characterized by constant properties $\alpha_i, \sigma_i, \kappa_i$ with $i = \{A, B\}$. The layers are connected in parallel to electrodes with temperatures T_0, T_L and electrochemical potentials μ_0, μ_L. A two-dimensional analytic solution of the equation $\mathbf{j} = -\sigma(\nabla\mu/q + \alpha\nabla T)$ is not feasible. Instead, we assume that both parts of the parallel thermoelectric are treated independently in a one-dimensional CPM approach, where both legs have the same

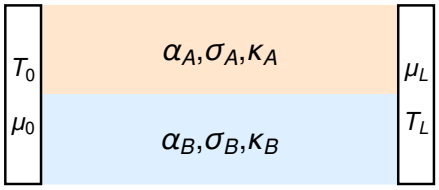

Figure 6.6: Setup of the parallel thermoelectric consisting of two species. The temperature gradient is parallel to the interface.

boundary conditions T_0, T_L and μ_0, μ_L. Hence, the difference $\mu_L - \mu_0$ is obtained by integrating along each leg:

$$\frac{\mu_L - \mu_0}{q} = -\frac{j_i}{\sigma_i} L - \alpha_i \left(T_L - T_0\right) = -\frac{I_i}{G_i} + \alpha_i \Delta T, \tag{6.14}$$

where $\Delta T = (T_0 - T_L)$ and G_i represents the total conductance of leg i, which can be expressed as $G_A = \sigma_A f S/L$ or $G_B = \sigma_B (1-f) S/L$ with total cross section area S. $f = S_A/S$ represents the amount of material A, where S_A is the cross section area of material A. Using that the voltage across both legs are equal and $I = I_A + I_B$ we obtain

$$I_A = \frac{I G_A}{G_A + G_B} + \frac{G_A G_B}{G_A + G_B} \Delta\alpha \Delta T, \tag{6.15}$$

where $\Delta\alpha = \alpha_A - \alpha_B$, from which we derive

$$P_{\text{eff}}(I) = \alpha_{\text{eff}} \Delta T I - \frac{I^2}{G_A + G_B} \tag{6.16}$$

with

$$\alpha_{\text{eff}} = \frac{G_A \alpha_A + G_B \alpha_B}{G_A + G_B} = \frac{\sigma_A \alpha_A f + \sigma_B \alpha_B (1-f)}{\sigma_A f + \sigma_B (1-f)}. \tag{6.17}$$

Equation (6.16) displays similarities to the simple CPM power eq. (2.43), including Joule heating and thermovoltage due to effective Seebeck coefficient α_{eff}, which is always smaller than the larger of α_A and α_B. In the parallel configuration, α_{eff} is weighted by electric conductances, while it is weighted by heat conductances in the segmented structure. Note that eq. (6.17) can be derived from the previously discussed eq. (5.23) for a two component bulk system using $\sigma_{\text{eff}} = f\sigma_A + (1-f)\sigma_B$ and $\kappa_{\text{eff}} = f\kappa_A + (1-f)\kappa_B$.

From eq. (6.16) the maximum of the parabola can easily be determined as

$$P_{\max} = \frac{\Delta T^2 (G_A \alpha_A + G_B \alpha_B)^2}{4(G_A + G_B)}. \tag{6.18}$$

Interestingly, assuming that $\alpha_A < \alpha_B$, the maximum power output can be increased by decreasing G_A. In contrast, considering a CPM, decreasing its electrical conductance would lead to a lower maximal power output.

To derive the total heat current $j_{q,0} S = j_{q,0,A} f S + j_{q,0,B} (1-f) S$ at the left side, we add up contributions from both parts

$$j_{q,0} S = \alpha_{\text{eff}} T_0 I - \frac{I^2}{2(G_A + G_B)} + K_{\text{eff}} (T_0 - T_L), \tag{6.19}$$

where we have used the CPM temperature distributions eq. (2.37). The effective heat conductance reads

$$\begin{aligned} K_{\text{eff}} &= (K_A + K_B)\left(\frac{(\alpha_A - \alpha_B)^2 G_A G_B \overline{T}}{(G_A + G_B)(K_A + K_B)} + 1\right) \\ &= \frac{S\,(f\kappa_A + (1-f)\kappa_B)}{L}\left(\frac{(\alpha_A - \alpha_B)^2 \sigma_A \sigma_B \overline{T}}{\left(\frac{\sigma_A}{1-f} + \frac{\sigma_B}{f}\right)\left(\frac{\kappa_A}{1-f} + \frac{\kappa_B}{f}\right)} + 1\right) \end{aligned} \tag{6.20}$$

with $\overline{T} = (T_0 + T_L)/2$. Again, the similarity to the corresponding CPM result eq. (2.42) is apparent. Remarkably, with open boundary conditions, the heat current is not only governed by the Fourier heat $(K_A + K_B)(T_0 - T_L)$, but also by the sum of the Peltier heat carried by the currents $I_A = -I_B$. The electrical currents always transport (Peltier) heat from the hot to the cold side such that $K_{\text{eff}} > (K_A + K_B)$. Note that the effective heat conductivity eq. (6.20) bears a resemblance to the closed circuit heat conductivity eq. (2.28).

Using eqs. (6.16) and (6.19) and $M = R_l/R$ the efficiency can be determined as

$$\eta_{\text{eff}}(M) = \frac{\Delta T}{T_0}\frac{M}{M + 1 - \frac{\Delta T}{2T_0} + \frac{(M+1)^2}{z_{\text{eff}} T_0}}. \tag{6.21}$$

with the effective figure of merit

$$\begin{aligned} z_{\text{eff}} &= \frac{\alpha_{\text{eff}}^2 G_{\text{eff}}}{K_{\text{eff}}} = \frac{(G_A\alpha_A + G_B\alpha_B)^2}{(\alpha_A - \alpha_B)^2 G_A G_B \overline{T} + (G_A + G_B)(K_A + K_B)} \\ &= \frac{(f\sigma_A\alpha_A + (1-f)\sigma_B\alpha_B)^2}{(1-f)f\left((\alpha_A - \alpha_B)^2\sigma_A\sigma_B\overline{T} + \left(\frac{\sigma_A}{1-f} + \frac{\sigma_B}{f}\right)\left(\frac{\kappa_A}{1-f} + \frac{\kappa_B)}{f}\right)\right)}. \end{aligned} \tag{6.22}$$

In the limits $f \to 0$ and $f \to 1$ we obtain the figure of merit of material A and B, respectively. From the fact that $\alpha_{\text{eff}} < \max(\alpha_A, \alpha_B)$ and $\sigma_{\text{eff}} < \max(\sigma_A, \sigma_B)$, while the effective heat conductivity is larger than $\kappa_A + \kappa_B$, which behaves just as σ_{eff}, we conclude that $z_{\text{eff}} < \max((\alpha_A^2\sigma_A/\kappa_A), (\alpha_B^2\sigma_B/\kappa_B))$.

In a recent publication G. D. Mahan [152] also calculated the maximum efficiency based on the idea of independent legs, which are coupled via the temperatures and the potentials at the electrodes. He defines two figures of merit

$$Z_{\text{AB}} = \frac{\sigma_A\sigma_B\left(\alpha_A - \alpha_B\right)^2}{\left(\kappa_A + \kappa_B\right)\left(\sigma_A + \sigma_B\right)} \quad \text{and} \quad Z_b = \frac{\sigma_A\alpha_A^2 + \sigma_B\alpha_B^2}{\kappa_A + \kappa_B}. \tag{6.23}$$

In contrast to eq. (6.22), his interpretation benefits from the temperature independent figure of merits. On the other hand, our viewpoint facilitates a direct comparison to CPM. Moreover, the temperature-dependence of K_{eff} can be well understood by taking into account the ring currents.

In the following we compare eqs. (6.16), (6.19) and (6.21) to simulation results. Therefore a cubic parallel thermoelectric with dimensions $L = 0.01\,\text{m}$ is simulated on a two-dimensional grid with parameters from table 8. As for random composites (see section 5.3), we

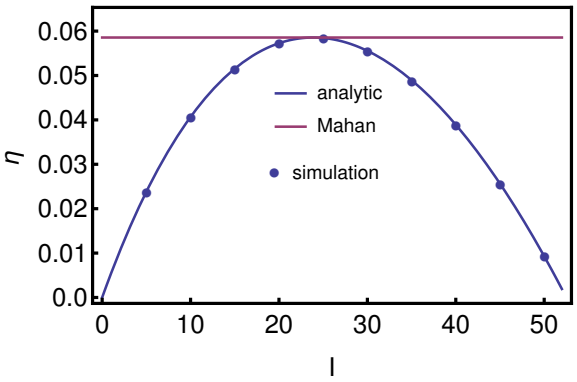

Figure 6.7: The efficiency produced by an parallel thermoelectric. A 40×40 grid has been used for the simulation and the electrode properties are modified as explained in the text. Furthermore, analytic results from this work and from [152] are shown.

avoid Peltier heating/cooling at the sample-electrode interface by assigning the respective material values to the sample-electrode bonds.

The efficiency resulting from the simulation, shown in fig. 6.7, agrees well with eq. (6.21). Additionally, Mahan's result for maximum efficiency coincides with our calculation. Apparently, the efficiency of a parallel structure is well described by the above approximation. A more detailed analysis reveals that both electrical powers coincide perfectly. This good agreement is inasmuch surprising, as the assumption of separated legs and constant current parallel to the temperature gradient are not fulfilled in the simulation. We checked this by deriving I_A and I_B by summing up the components of the current parallel to the interface. From cold to hot the current in the good conducting material A, I_A, increases, while I_B decreases, such that the total current is constant. As a consequence the simulated temperature and potential distribution differ from the ones derived within the analytic approach. We elucidate the good matching between the simulated power and eq. (6.16) by considering a minimal example shown in fig. 6.8a. The nodes a and d correspond to the electrodes, while the material is characterized by two nodes, b and c. Nodes are connected by a conductance G_{ij} and a voltage source $U_{\mathrm{ij}} = \alpha_{ij}(T_i - T_j)$. Now, we are interested, whether the properties of bond bc affect the electrical power $P = IU_{\mathrm{ad}}$, with the voltage between a and d. We

	σ [S/m]	κ [W/K m]	α [V/T]
material A	10^5	5	0.0001
material B	$5 \cdot 10^4$	1	0.0005

Table 8: Parameter used for the simulation of parallel generators. The temperatures of the heat bathes are set to $T_0 = 600\,\mathrm{K}$ on the hot and $T_L = 300\,\mathrm{K}$ on the cold side. The dimension of the cubic generator leg is $L = 0.01\,\mathrm{m}$.

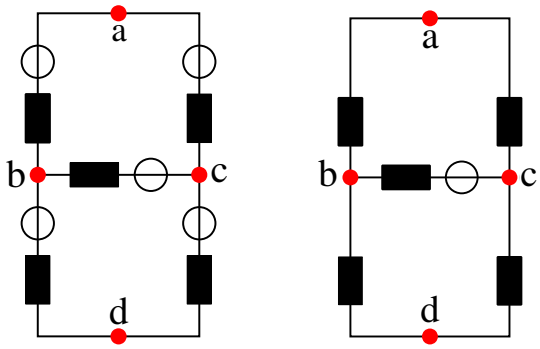

Figure 6.8: Figure 6.8a is a minimal example of a parallel thermoelectric consisting of electrode terminals a and d as well as material nodes b and c. The superposition principle allows to investigate the influence of a single voltage source in fig. 6.8b.

assume that $G_{ab} = G_{bd} = G_A$ and $G_{ac} = G_{cd} = G_B$, and using Kirchhoff's first law we find

$$U_{ad} = \frac{2I - G_A(U_{ab} + U_{bd}) - G_B(U_{ac} + U_{cd})}{G_A + G_B}, \tag{6.24}$$

which is independent of properties of bond bc, although $U_{bc} \neq 0$. I is the external current entering node a and leaving node d, or vice versa. In order to get a better understanding of the influence of U_{bc}, we use the superposition principle for linear electrical circuits [1]. The response of a system consisting of more than one independent source, is the sum of the responses provoked by each source. Hence, we remove all other voltage sources except U_{bc} ending up with the network in fig. 6.8b. If conductances are chosen as above, the analysis shows that U_{bc} does not affect U_{ad}. The reason is a symmetry between the circuits abc and bcd. In both, the relation between the conductances on the left and right side is equal. Hence, the potentials at a and d must be equal as well. However, setting G_{ab} to a different value breaks the symmetry, and U_{bc} and G_{bc} have an influence on the voltage U_{ad}. As a consequence, for temperature-dependent material the bond bc cannot be neglected.

Extending the minimal example is straight forward, and using Kirchhoff's voltage law, one can always argue that the potential difference between the electrodes due to sources at the interface is zero.

As related to the heat current, the analytical model and the simulation deviate slightly. Here, additional contributions have to be taken into account: First, Peltier and Joule heat are different, second Peltier heat at the interface occurs and third a further contribution from the divergence of the Fourier heat, which has an additional contribution due to changing of the heat conductance.

1 components are independent of electrical current

In this section, we examined the thermoelectric performance of two simple compounds: segmented and parallel arrangement of two different materials.

It turns out, that in most cases, the segmented thermoelectric produces less power and has a lower efficiency than expected from the the effective parameters. This is caused by the influence of the current on the temperature distribution. For the generator mode, usually the temperature difference across the material with the lower absolute Seebeck coefficient is enlarged compared to open circuit conditions. This in turn, decreases Seebeck voltage, electrical power and efficiency. However, we derived conditions for a power enhancing regime. Here, Peltier cooling occurs at the interface, but Joule heating and Fourier heat elevate the interface temperature such that the temperature difference across the material with the higher absolute Seebeck coefficient is enhanced.

The application of segmented material in a cooling device has not been explored in this thesis. But, it has been shown that a staircase Seebeck profile leads to better cooling performances [153]. A generalization of the presented ideas leads to the Thomson cooler, which is characterized by a continuously increasing Seebeck coefficient from cold to hot [68].

The investigation of the parallel arrangement of two materials was motivated by its similarities to a new generator configuration discussed in chapter 7. Placing both electrodes at the cold side, the generator can not be treated analytically, while the parallel thermoelectric can. Therefore, we, and before us further authors, approximated that both materials are just coupled via the electrodes. We showed by comparison to simulations that the approximation is sufficient to describe the electrical power exactly if materials A and B are constant. In contrast to the segmented structure, the parallel arrangement is less performant than the better of its constituents. Moreover, we indicated an enhanced heat transport due to ring currents even in open circuit conditions. We will recover this enhanced effective heat conductivity in the new generator setup, where it is clearly a disadvantage.

7

SIMULATION OF A NOVEL GENERATOR CONCEPT

After the discovery of thermoelectric effects, it took approximately a century until the first thermoelectric generator (TEG) was employed outside of a laboratory environment in 1948 [154]. As explained before, due to the low efficiency TEGs remained reserved for niche applications requiring low maintenance. Just recently, new fields of applications emerged. Especially recovering waste heat is of high interest, enhancing the efficiency of engines or power plants and thereby shrinking the fossil energy consumption and pollution. Already a zT of 2 enables a worthwhile application of TEG in industrial applications like cement production and aluminum smelting [1].

New fields of application may not only be opened by novel or improved materials, but also device research can do its part [155]. With this in mind we support the exploration of a new device concept, which is realized experimentally by A. Becker [156] and R. Chavez [23]. As a basis we use the Onsager network model from chapter 3 and extend it in order to approach experimental results. Initially, we present the basics of the conventional TEG.

7.1 CONVENTIONAL THERMOELECTRIC GENERATOR

A TEG is depicted in fig. 7.1. Alternating p- and n-type material legs are connected by metal bridges such that they are electrically in series. Thermally, however, all legs are in parallel, since heat is flowing from the top to the bottom.

The power P and the efficiency η of a single leg in the framework of the CPM are given by eqs. (2.45) and (2.46), respectively. Extending the efficiency for a whole device is straightforward. For this purpose the material figure of merit z is replaced by the device figure of merit Z including geometry and contact resistances. The dependence of P and η on the the ratio $M = R_l/R$ is depicted in fig. 7.2. As discussed in section 2.2.3, impedance matching is obtained by $M = 1$, while the efficiency is maximized by $M = \sqrt{1 + z\overline{T}}$ with $\overline{T} = (T_h + T_c)/2$. Due

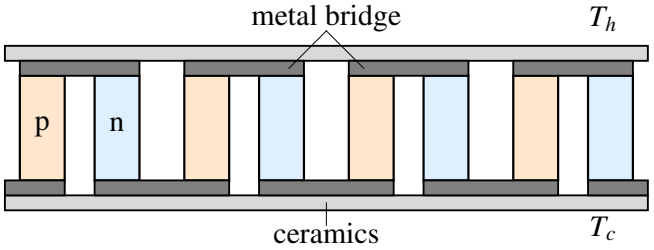

Figure 7.1: A conventional device is constructed by placing p- and n-type legs in an alternating sequence and connecting them such that they are electrically in series and thermally in parallel.

to irreversible effects stemming from heat leakage and Joule heating η is way below the Carnot efficiency.

Besides, Carnot described an idealized cyclic heat engine, which has to work infinitely slowly to avoid all sources of irreversibility. As a consequence, it does not produce power at all. More realistic approaches are comprised in the framework of finite-time thermodynamics. Coupling a heat engine to a cold and a hot reservoir via heat conductances $K_{\text{hot}}, K_{\text{cold}}$ a finite-rate heat transfer is ensured. Even if we assume that the working medium does not produce entropy, the heat flow from the reservoirs does. For such a machine, which is denoted as endoreversible, Curzon and Ahlborn [157] derived the efficiency at maximum power output

$$\eta_{\text{CA}} = 1 - \sqrt{\frac{T_c}{T_h}}. \tag{7.1}$$

Interestingly, eq. (7.1) is independent of the heat conductances K_{hot} and K_{cold}, and solely depends on the heat bath temperatures, although the working medium does not reach the heat bath temperatures T_h and T_c.

Now, let us regard a TEG as an endoreversible and a non-endoreversible ($K \neq 0, G \neq 0$) thermodynamic engine. We consider the heat flux in CPM approximation at the interface between the thermoelectric material and the connections to the heat conductances K_{hot} and K_{cold}, respectively [158, 159, 160]:

$$K_{\text{hot}}\,(T_h - T_{h,1}) = \alpha T_{h,1} I - \frac{I^2}{2G} + K(T_{h,1} - T_{c,1}) \tag{7.2}$$

$$K_{\text{cold}}\,(T_{c,1} - T_c) = \alpha T_{c,1} I + \frac{I^2}{2G} + K(T_{h,1} - T_{c,1}). \tag{7.3}$$

Equations (7.2) and (7.3) are solved for the interface temperatures $T_{h,1}$ and $T_{c,1}$, which are subsequently used to derive expressions for $P = I_{\text{q,h}} - I_{\text{q,c}}$ and $\eta = P/I_{\text{q,h}}$ independent of $T_{h,1}$ and $T_{c,1}$.

First, we discuss an endoreversible engine requiring reversible TE material with $K = 0$ and $G = 0$. A meaningful characterization of a heat engine is delivered by its power versus efficiency curve: P and

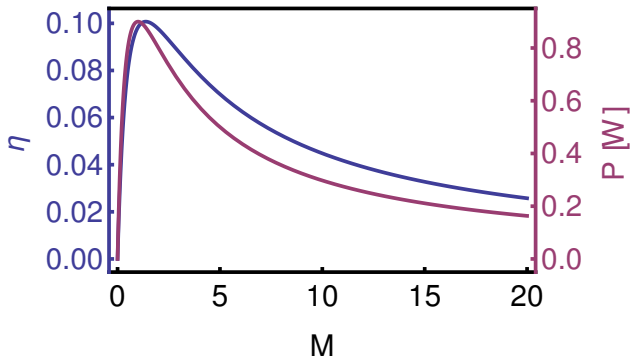

Figure 7.2: Power and efficiency in dependence of M for $T_h = 600\,\text{K}$, $T_c = 300\,\text{K}$, $Z = 0.002\,\text{K}^{-1}$, $G = 1000\,\text{S}$ and $K = 0.02\,\text{W/K}$.

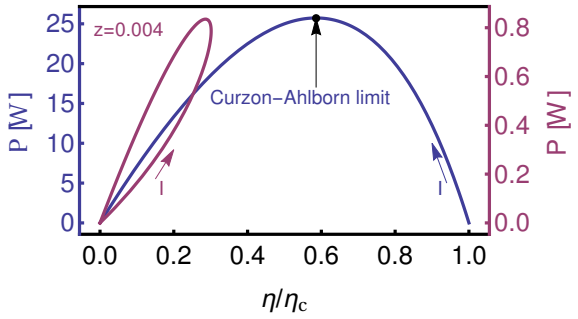

Figure 7.3: Power versus efficiency characteristics for an endoreversible TEG (blue) and for a non-endoreversible TEG (red). For both cases reasonable values are chosen: $T_h = 600\,\mathrm{K}$, $T_c = 300\,\mathrm{K}$, $\alpha = 0.0002\,\mathrm{V/K}$ and $K_{\mathrm{hot}} = K_{\mathrm{cold}} = 1\,\mathrm{W/K}$. Additionally, the non-endoreversible TEG is characterize by $G = 1000\,\mathrm{S}$ and $K = 0.01\,\mathrm{W/K}$.

η are parameterized by another variable, here the current I, and then plotted against each other. The power versus efficiency curve for the endoreversible machine is depicted in blue in fig. 7.3. For $I = 0$, which correspond to infinitely slowly working cyclic heat engines, we find $\eta = \eta_c$, but $P = 0$. With increasing current the maximum power output is passed at η_{CA}. Letting I rise further the Peltier effect cools down the hot and heats up the cold side until $T_{h1} = T_{c1}$ and $\eta = 0$, $P = 0$. If even higher currents are applied, the engine starts to consume power. Furthermore, it has been pointed out that the power output of an endoreversible TEG is larger than the one produced by the Curzon-Ahlborg engine, since the latter works in steps, while a TEG works continuously [159].

Let us now take into account internal dissipation due to electrical and heat resistance (non-endoreversible TEG). Similar derivations, although within approximations, can be found in [158, 160]. Starting from eqs. (7.2) and (7.3) we perform the same calculation as for the endoreversible TEG, but with finite K and G. As a result we obtain the red colored power versus efficiency curve in fig. 7.3. Note that, although $z = 0.004\,\mathrm{K}^{-1}$ is a high value, the efficiency stays way below η_C. The shape of the characteristic is influenced by all occurring conductances $G, K, K_{\mathrm{hot}}, K_{\mathrm{cold}}$ and by z.

For the non-endoreversible TEG further interesting properties are derived by Apertet et al. [160]. They assumed that $T_h - T_c$ is small enough to neglect the produced power in comparison to the heat flow. First, it is shown that electric impedance matching is not obtained at $M = 1$, but rather by an expression larger than unity depending on $K_{\mathrm{hot}}, K_{\mathrm{cold}}$. Furthermore, the importance of thermal impedance matching is emphasized. The latter targets a proper adjustment of thermal contact conductance and internal heat conductance.

7.2.1 *Basic idea*

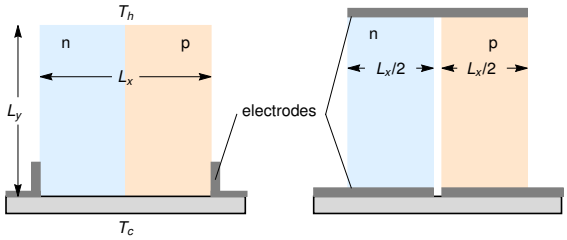

Figure 7.4: A two-dimensional sketch of a pn junction used as a generator, which is denoted as PNG (left) and a conventional thermoelectric generator (TEG) on the right. For the following comparison, we choose the dimensions of TEG and PNG as indicated in the figure.

Instead of separated p- and n-type legs, a pn junction, whose interface is aligned to the temperature gradient is used as a generator element (see fig. 7.4). We denote this type of generator as PNG. Originally, the idea was proposed by G. Span and M. Wagner, who studied pn junctions as thin film devices in a series of publications [161, 162, 163, 22, 164]. Their research aimed to increase the efficiency due to additional charge carriers gained from the space charge region (SCR) as explained below. However, our priority is to simulate bulk-like devices fabricated from nanostructured bulk silicon, while neglecting effects of charge carrier separation. Nevertheless, the usage of a pn junction has substantial advantages: electrical contacts on the hot side are needless. In a conventional TEG T_h is limited by the stability of the hot side contacts, but by their dismissal higher temperature regimes are made available and new fields of application open up. The missing hot side metal bridge may also be a benefit for power and efficiency, since a temperature drop across the substrate is avoided and the thermoelectric material experiences an enhanced hot side temperature.

7.2.2 *Literature overview*

First, we present the method and some basic results from G. Span and M. Wagner, who inspired our research. They performed simulations based on a drift-diffusion model with the MINIMOS NT software package [165]. Their simulation solves iteratively continuity equations including generation and recombination, Poisson's equation and an equation describing the electric current according to the Onsager-de Groot-Callen theory. The temperature is derived from a differential equation, similar to eq. (2.35), but taking into account generation and recombination [75].

Their simulations of pn and pin structures, a pn junction separated by an intrinsic layer, showed an enhancement of power and efficiency, if thermally generated charge carriers are taken into account [22]. An

explanation emanates from the temperature gradient, which drives charge carriers from hot to cold disturbing the local carrier balance. In the depleted SCR on the hot side, an enhanced charge carrier generation is observed, while on the cold side stronger recombination takes place [163, 166]. If not recombining, charge carrier pairs produced in the SCR are separated by the built-in potential such that electrons flow towards the n-type and holes towards the p-type semiconductor. Moreover, there is also the possibility that charge carriers generated inside the neutral region diffuse into the depletion zone, are separated by the SCR and become additional majority charge carriers [166, chap. 13.9]. To some extent the production of additional charge carries exhibit a similarity to solar cells, but instead photonic energy, thermal energy is exciting charge carriers. It is assumed that the additional charge carriers superimpose those driven by the Seebeck effect resulting in a better overall performance.

In subsequent investigations it has been shown that especially small devices with a length smaller than 1 mm profit from missing hot side contacts, because the temperature drop across the active material decreases with the length, which can be counterbalanced by removing the hot side contacts [22]. The temperature distribution has been optimized by using Si/SiGe structure leading to a shallow slope in the hot regime and a steep one at the cold side. Indeed, this leads to an amplified carrier generation and subsequently to better performances [161, 164]. Furthermore, tailoring the SCR and the existence of trapping states were found to be important parameters for device optimization.

Beside the above mentioned investigations there are a few further publications on pn junctions in relation to thermoelectricity. Effects of a temperature gradient parallel to a pn interface have been studied by Fu et al. [167] employing a drift-diffusion model, where position dependent transport parameters were derived from Boltzmann transport equation. For open circuit conditions they found two current vortices, one in the p- and one in the n-type layer, which are separated by a highly resistive SCR. Close to and within the SCR current is flowing in the direction predefined by the Seebeck voltage and far away from the junction the direction is reversed. According to their explanation, the low carrier concentrations in the SCR results in a high Seebeck coefficient driving the current in the expected direction. Regarding the SCR as one layer and the neutral zone as another we recognize that the situation is similar to a parallel thermoelectric (see section 6.3). Concerning the heat conductance, it is argued that the Joule heating produced by current loops, which is assumed to be redistributed in equal parts to hot and cold side lowers the effective heat conductivity. This consideration does not take into account the Peltier heat αTI transported by the charge carriers. For parallel TE, it was pointed out by Apertet et al. [151], and similarly shown in this work, that the heat conductance is actually enhanced by an electric current flow (see eq. (6.19) and the following explanation).

The influence of a cut along the interface of a PNG was investigated in [168]. A similar experiment shall be presented in this work and details are discussed in the corresponding section 7.3.7.

An investigation of a diode like structure with a large (∼mm) intrinsic layer revealed enhanced conversion efficiency [169, 170]. Particularly, it was observed that a thin (∼µm), heavily doped emitter layer increases the open circuit voltage and the short circuit current by a factor 2-3 above the corresponding values of the intrinsic layer alone, which are of thermoelectric nature. Nonetheless, it is believed that the physics of such a structure are not well understood [56].

In another work it was shown that the current voltage characteristics of a pn junctions made of BiSbTe and created by sintering behave diode-like in the forward direction, while reversed bias is not accompanied by blocking behavior [171]. A comparable behavior is found in nanostructured silicon [172, 23] and an explanation follows in section 7.4.

7.2.3 *Experimental realization*

Experimental realizations of the PNG were produced by A. Becker [172, 156] and R. Chavez [23, 173]. Their samples were built in a bottom-up approach from highly doped silicon. In a first step the respective raw material, highly doped nanopowder, is fabricated. The n-type material is manufactured by plasma synthesis [60]. A microwave reactor creates a plasma, which is fed by silane (SiH_4) and phosphine (PH_3). The p-type powder is synthesized in a hot-wall reactor, which uses silane and diborane (B_2H_6) as precursors. Silane is split into silicon and hydrogen and subsequently, Si particles grow due to nucleation, condensation and sinter processes. Therefore a supersaturated vapor is required, which is thermodynamically instable such that nucleation and condensation take place. It is possible to produce spherical, highly crystalline, soft-agglomerated particles with small diameters between 4-50 nm. The particles are just connected via point-like contacts.

The highly porous powder is densified by current-activated pressure-assisted densification to which chapter 4 is devoted. It is worth mentioning that processing under air allows oxygen to react with the silicon before densification. From the sinter pellet pn junction samples are cut into the desired shape and electrodes are attached in a multi-stage process [174].

7.3 SIMULATION OF THE PN-GENERATOR

We start our investigations with simulation of a PNG neglecting the influence of the diode structure at the interface, and different doping is solely reflected by the sign of the Seebeck coefficient, which is chosen such that it has the same absolute value in p- and n-type material $\alpha = \alpha_p = -\alpha_n$.

Ideas presented in this section have been published in [173].

7.3.1 *Simulation setup*

The general appearance of the simulation setup is depicted in fig. 7.4 (left). Due to translation invariance in z-direction, which is pointing out of plane, a two dimensional simulation setup is sufficient, and we discretize the generator by a square lattice. If not stated differently, we take the parameters from table 9.

The electrodes are located at the cold side and their height is $L_y/5$. They are characterized by the same parameters as the adjacent material and their temperatures develop according to

$$\dot{T}_i = \frac{1}{C}\sum_j \left(-I_{q,ij} + I_{ij}\frac{(\mu_i - \mu_j)}{2q} \right) - \frac{\kappa_b L_y L_z}{5}(T_i - T_c), \tag{7.4}$$

taking into account thermoelectric heat production as discussed in section 3.1. Additionally, a coupling via the boundary heat conductivity κ_b to a heat reservoir with temperature T_c, to which all sites at the bottom are contacted as well. Sites at the top are connected to a heat reservoir with T_h. The corresponding heat conductance is derived as $K_b = \kappa_b L_x L_z / N_x$. Hence, the heat current flowing into the PNG is derived from

$$I_{q,h} = \sum_j K_b(T_h - T_j), \tag{7.5}$$

where j runs over all sites connected to the hot side heat bath. On the cold side we have to take into account the heat flowing from the electrodes into the heat bath resulting in

$$\begin{aligned} I_{q,c} = &\sum_j \big(K_b(T_j - T_c)\big) \\ &+ \frac{\kappa_b L_y L_z}{5}(T_{e_1} - T_c) + \frac{\kappa_b L_y L_z}{5}(T_{e_2} - T_c). \end{aligned} \tag{7.6}$$

Here j runs over all sites connected to the cold side heat bath and T_{e_1} and T_{e_2} represent the electrode temperatures. In the following we choose $\kappa_b = 10^5\,\mathrm{W/(Km^2)}$, which assures a small temperature drop between reservoirs and device.

7.3.2 *Finite size behavior*

We investigate the finite size behavior of the PNG simulations. Therefore the maximum power $P_{\max} = P(I_{\max})$ and the heat current into the system $I_{q,h}(I_{\max})$ are derived for different number of supporting

$L_x = L_y = L_z\,[\mathrm{m}]$	$\sigma\,[\mathrm{S/m}]$	$\kappa\,[\mathrm{W/(Km)}]$	$\alpha_{\mathrm{p/n}}\,[\mathrm{V/K}]$
10^{-2}	10^5	2	$\pm 2 \cdot 10^{-4}$

Table 9: If not stated otherwise, we use this simulation parameters in the present chapter. A positive Seebeck coefficient represents p-type material and a negative Seebeck coefficient stands for n-type material. Moreover, the temperature difference is set to $\Delta T = 700\,\mathrm{K}$.

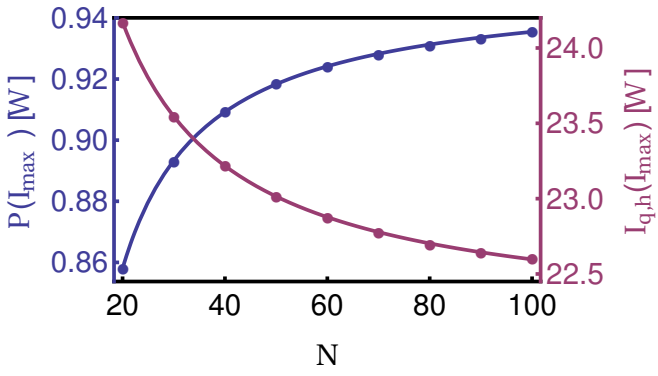

Figure 7.5: The maximum Power output $P_{\max} = P(I_{\max})$ (blue) and the heat current from the hot heat bath into the PNG at maximum current $Q_h(I_{\max})$ are shown in dependence of the number of supporting sites $N = N_x = N_y$

sites $N = N_x = N_y$ of the square grid, while all other parameters are fixed (see fig. 7.5). $P_{\max}$ exhibits a dependence on N, which we partly refer to an effect observed and investigated in 1d segmented thermoelectric(see section 3.2.2): due to the approximated interface temperature the voltage and consequently the power contain errors, which vanish as N^{-1}. A further finite size effect is caused by the curved electrical current flow approximated by the grid. Fitting $P_{\max}(N)$ to

$$f_{\mathrm{P/Q}}(N) = \frac{a}{b \pm N} + c \tag{7.7}$$

and using the minus sign, we get the blue line in fig. 7.5, which is an adequate description. From the fit we derive $\lim_{N\to\infty} f_P(N) = 0.951$. Using the plus sign in eq. (7.7), we find that the heat current $I_{q,h}(I_{\max})$ approaches $\lim_{N\to\infty} f_Q(N) = 22.162$. Again, grid effects influencing the heat current vanish for large N.

In the following, simulations are performed with 60×60 grids, which is a good trade-off between simulation time and accuracy.

7.3.3 *Power and efficiency*

At first, we compare power and efficiency of a PNG and a TEG, which allows us to assess PNG's applicability. The TEG consists of two legs, and each of them is described in the framework of a 1d CPM connected by perfect electrical contacts with vanishing resistance. Transport parameters, which are equal for both generators, are defined in section 7.3.2, and for a proper comparison the dimensions of PNG and TEG have to be equal (see fig. 7.4). Those conditions are fulfilled for each following comparison between TEG and PNG.

Power and efficiency of the PNG (points and lines in fig. 7.6) are strongly reduced compared to corresponding TEG quantities (dashed lines). The origin of this difference can be understood by considering the electrochemical potential distribution $\mu(\mathbf{r})/q$, which is shown in fig. 7.7. In order to understand $\mu(\mathbf{r})/q$, imagine a TEG as described above. In open circuit conditions μ/q increases from hot to cold for

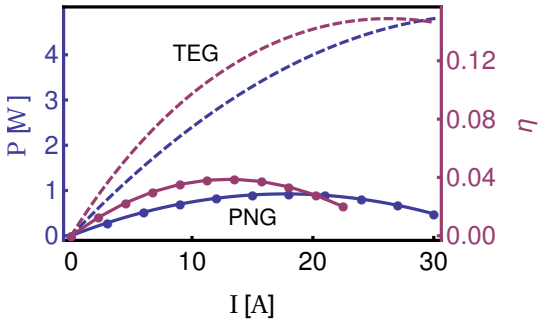

Figure 7.6: Power (blue) and efficiency (red) of a PNG (dots and lines) and a TEG (dashed lines) for $\Delta T = 700\,\mathrm{K}$. A basic PNG performs significantly worse than a TEG.

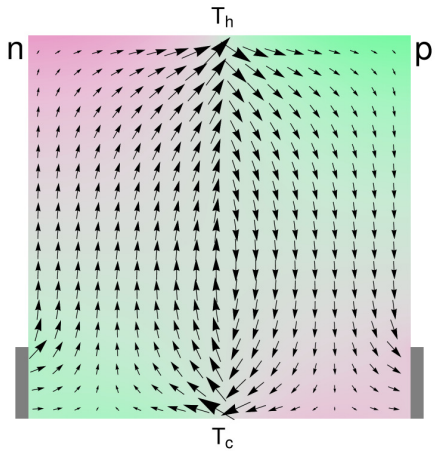

Figure 7.7: Electrical current (black arrows) and potential distribution $\mu(\mathbf{r})/q$ in a PNG with $\alpha = 1.28 \cdot 10^{-4}\,\mathrm{V/K}$. μ/q increases from green to pink. Strength of current is indicated by arrow size. The current entering and leaving the electrodes amounts to $I = 12.8\,\mathrm{A}$.

p-type and vice versa for n-type material, while the electrochemical potentials coincide at the top due to the perfect electrical contacts. Removing the latter and uniting both legs we obtain a PNG. Here, the potential has to change. Otherwise a strong current would flow on the cold side from p- to n-type. To counterbalance this current the line of equal potential shifts from the hot side to $y \approx L_y/2$. Without a detailed investigation, which is presented below, we directly realize that this leads to a lower output voltage reducing P and η. Even if we assume that the potential difference between top and bottom on each side is the same as in a TEG, the voltage between the PNG-electrodes will at most be half of the TEG voltage.

Such a potential distribution gives rise to current vortices as depicted in fig. 7.7 (black arrows, technical current direction is used), which are even present in open circuit conditions. A similar effect occurs in the parallel configuration discussed in section 6.3. Of course, this current distribution strongly affects Joule heating and Peltier heating at the interface. In open circuit conditions cooling occurs at the hot side, while the cold side is heated.

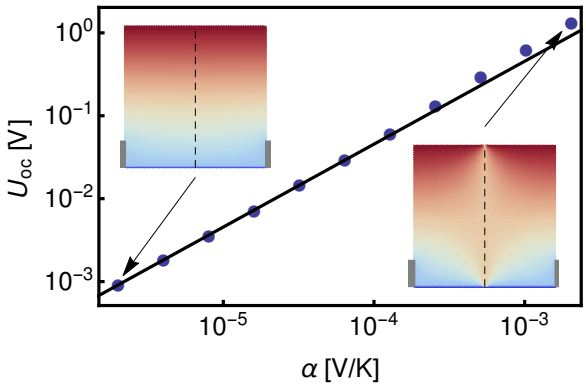

Figure 7.8: The open circuit voltage U_{oc} in dependence of α. The black line represents the function $f(\alpha) = 440 \cdot \alpha$, which perfectly characterize U_{oc} for small α. For $\alpha \gtrsim 10^{-4}\,\mathrm{V/K}$ deviations from the linear behavior are found. The insets depict the spatial temperature distribution for two values of α.

Further insight can be obtained by a detailed analysis of the power P. It is quantified by effective parameters according to

$$P(I) = U_{oc} I - R_{eff} I^2. \tag{7.8}$$

Indeed, eq. (7.8) is derived in a 1d CPM, but we validated that it yields an excellent description of P in the interesting, power producing regime $P > 0$ for all chosen parameters. Just as an example, the blue line in fig. 7.6 stems from a fit with $U_{oc} = 0.1042(3)\,\mathrm{V}$ and $R_{eff} = 0.00293(5)\,\Omega$, while for the TEG $U_{oc,TEG} = \alpha\Delta T = 2 \cdot \alpha\Delta T = 0.28\,\mathrm{V}$ and $R_{TEG} = 0.004\,\Omega$. In the present example, the slight reduction of resistance is not able to compensate for the losses of the open circuit voltage.

7.3.4 *Analysis of U_{oc}*

In eq. (7.8) U_{oc} represents a fitting parameter, however, we verified that it corresponds to the open circuit voltage. We will work out by which parameters it is affected and in how far U_{oc} bears potential for improvement.

As expected, the Seebeck coefficient influences U_{oc}. We vary α such that $\alpha = \alpha_p = -\alpha_n$ and show its effect in fig. 7.8. For small α the open circuit voltage increases as

$$U_{oc} = \Delta T_{eff} \cdot \alpha, \tag{7.9}$$

where the constant ΔT_{eff} is regarded as an effective temperature difference. For the exemplarily data, $\Delta T_{eff} = 440\,\mathrm{K}$, which is much smaller than the real temperature difference $\Delta T = 700\,\mathrm{K}$ between hot and cold side. For large α, deviations occur, which are caused by strong Peltier heating at the interface close to the cold side. With increasing α the strength of the Peltier heating/cooling rises, and in addition to it more current is flowing in circular way through the PNG, which is crossing the interface and enhances the heating/cooling even further. Thereby a temperature gradient increasing from the electrodes

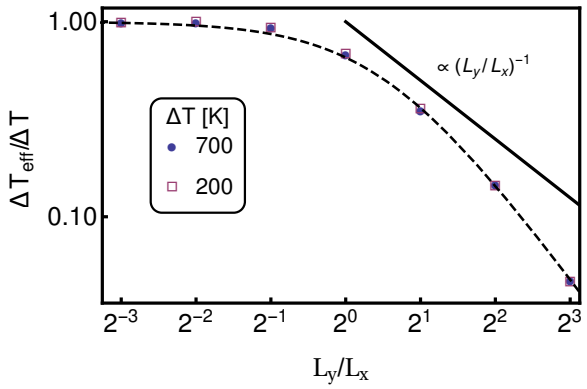

Figure 7.9: The effective temperature ΔT_{eff} in dependency of the ratio L_y/L_x for total temperature drop $\Delta T = 700\,\text{K}$ (blue points) and $\Delta T = 200\,\text{K}$ (red squares). The dashed line is produced by a fit further described in the text.

towards the interface is created (see insets of fig. 7.8) and the corresponding Seebeck voltage enhances U_{oc}. Details of this effect shall be discussed below.

Now, we examine which parameters affect ΔT_{eff}. It turns out that device shape has a strong influence on ΔT_{eff}. In order to analyze this, we change L_y, while keeping $L_x = L_z = 0.01\,\text{m}$ constant. Furthermore, electrode sizes are always $L_y/5$. For each shape, α is varied and ΔT_{eff} determined. We choose $\alpha \lesssim 10^{-4}\,\text{V/K}$ to avoid non-linear behavior. We checked that the simulation of a non-cubic device is not affected by the number of sites in x- and y-direction, and subsequent simulations are performed with a 60×60 grid.

The results are summarized in fig. 7.9. For broad PNGs, $L_y \ll L_x$, ΔT_{eff} saturates and tends towards ΔT, while it decreases for elongated devices, $L_y \gg L_x$. A fit with

$$f(L_y/L_x) = 1 - \frac{1}{1 + a(L_y/L_x)^{-b}} \tag{7.10}$$

leads to a convincing description using $a = 2.0(1)$ and $b = 1.80(5)$. In the following, we try to clarify the limit $(L_y/L_x) \to 0$. Given a ΔT, a TEG delivers $U_{\text{oc,TEG}} = 2\Delta T\alpha$, since each of the two separated legs produce the voltage $|\alpha\Delta T|$. However, the voltage generated by a broad PNG is a factor 2 less. It is helpful to look at the potential distribution $\mu(\mathbf{r})/q$ in a PNG depicted in fig. 7.10 (upper, left). Although fig. 7.10 shows $\mu(\mathbf{r})/q$ for varying length L_y, we choose the aspect ratio to be one, which allows for a compact presentation. For reasons discussed before, the interconnection of p- and n-type material entails that the line of equal potential is shifted away from the hot side. In open circuit conditions and for sufficiently small α, the temperature distribution $T(\mathbf{r}) \approx T(y)$ (see inset of fig. 7.8). Moreover, the temperature gradient is approximately constant implying $T(L_y/2) = (T_h + T_c)/2$. Looking at $\mu(\mathbf{r})/q$ for $L_y/L_x = 0.125$, we recognize that inside the single materials, $\mu(\mathbf{r})/q$ is hardly affected by the interface. Therefore, the voltage is built up from $y \approx L_y/2$

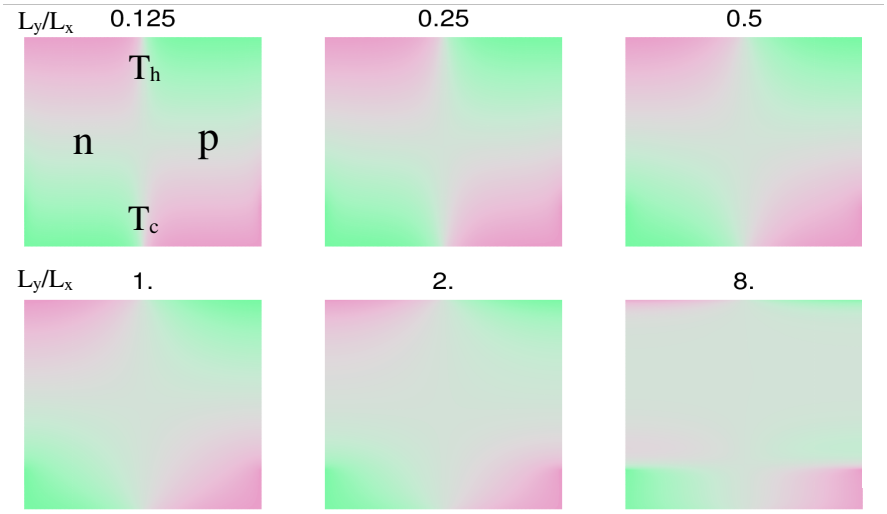

Figure 7.10: The potential distribution $\mu(\mathbf{r})/q$ in PNGs for varying ratios L_y/L_x. In order to obtain a clear presentation, the figures are rescaled to a square-like appearance. The color coding does not reflect absolute values, but is relative to the extreme values in each sample.

over $\Delta T/2$ yielding $U_{\text{oc}} = 2\alpha(T_h - T_c)/2 = \alpha(T_h - T_c)$, such that $\Delta T = \Delta T_{\text{eff}}$ in this limit.

From the fit we learned that for $L_y/L_x > 1$ the effective temperature difference decreases significantly faster than $(L_y/L_x)^{-1}$. As a main cause we identified that the temperature gradient and hence the potential gradient in y-direction shrink as L_y/L_x is enlarged. This is irrelevant for the quasi one-dimensional TEG, because the open circuit voltage is determined by ΔT. Here however, decreasing $\partial_y T$ is accompanied by an increase of the transitional zone around the interface leading to a convergence of the potentials in both parts. Thereby a region of very small potential gradient forms and extends further towards the cold side.

Without going into more detail, we comment on the influence of the electrical conductivity. By performing simulations with different conductivities, we found $U_{\text{oc}}(\sigma = 10^5\,\text{S/m}) - U_{\text{oc}}(\sigma = 10^4\,\text{S/m}) \propto \alpha^3$.

7.3.5 *Analysis of* R_{eff}

Now, the second fit parameter R_{eff} shall be discussed. Figure 7.11 shows that for a large range $10^{-6}\,\text{V/K} < \alpha < 10^{-3}\,\text{V/K}$, R_{eff} can be expressed as

$$R_{\text{eff}} = R_{\text{PNG}} + c_I \alpha^2 \tag{7.11}$$

with the isothermal PNG resistance R_{PNG} and a coefficient c_I, which is independent of (L_y/L_x).

In order to understand the quadratic dependence on α we consider a one-dimensional segmented thermoelectric with $\alpha_A = -\alpha_B = \alpha$ and a very large $\sigma = 10^8\,\text{S/m}$ suppressing Joule heating. The interface between p- and n-type material is located in the center. The electrodes are at fixed temperature $T_e = 300\,\text{K}$, and a fixed current I

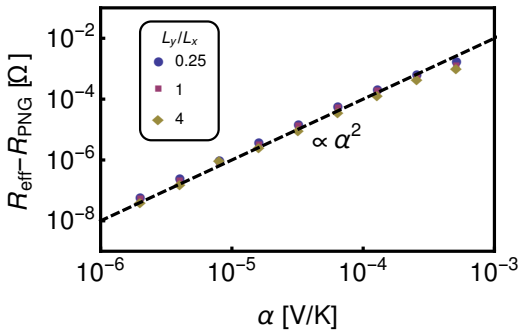

Figure 7.11: The fitting parameter R_{eff} from eq. (7.8) shows a quadratic dependence on α. R_{PNG} is the resistance measured at isothermal conditions.

is forced through the structure. For a large range of I and α, Joule heating is negligible and the temperature distribution is mainly affected by the interface Peltier effect as shown in fig. 7.13. Such a triangle distribution creates Seebeck voltages in series adding up to $U_{\text{if}} = 2\alpha(T_{\text{if}} - T_e) = 2\alpha\Delta T_{\text{if}}$, with the interface temperature T_{if}. The current direction determines, whether heating or cooling takes place at the interface. Thereby the current also causes the sign of U_{if}, which is such that it always adds up to the resistive voltage as indicated by the Thévenin equivalent of the segmented thermoelectric (see fig. 7.12). But most importantly, U_{if} is proportional to I, since $\Delta T_{\text{if}} \propto I$ as shown in fig. 7.14. Since the strength of Peltier effect scales linearly with α, also $\Delta T_{\text{if}} \propto \alpha$ such that the total voltage reads

$$U = U_{\text{if}} + RI = (c\alpha^2 + R)I \tag{7.12}$$

with a constant c. Equation (7.12) clearly implies eq. (7.11). In summary, since the temperature induced voltage $U_{\text{if}} \propto \alpha^2$ is also proportional to I we observe a linear relationship between voltage and current, just as for the resistance.

Now, we state that an equivalent situation, although more complex, is present in a PNG. Again, a temperature difference ΔT_{if} between electrodes and interface and the related Seebeck voltage U_{if} are responsible for the behavior of R_{eff}. We distinguish between open circuit conditions and the case of an attached load. Even in the former case, internal current vortices occur, entailing Peltier heating at the cold side and cooling at the hot side. In contrast to the seg-

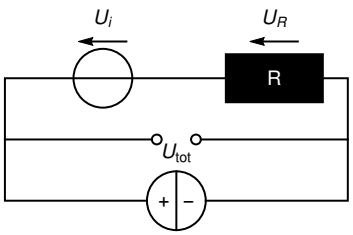

Figure 7.12: Thévenin equivalent of the segmented thermoelectric with an external current source. The induced Seebeck voltage and the resistive voltage are characterized by the same polarity.

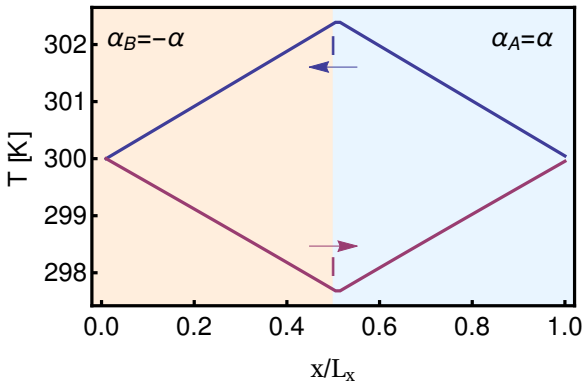

Figure 7.13: The Peltier effect at the interface creates the shown temperature distribution, if Joule heating is negligible. The current direction determines, whether the interface is cooled or heated.

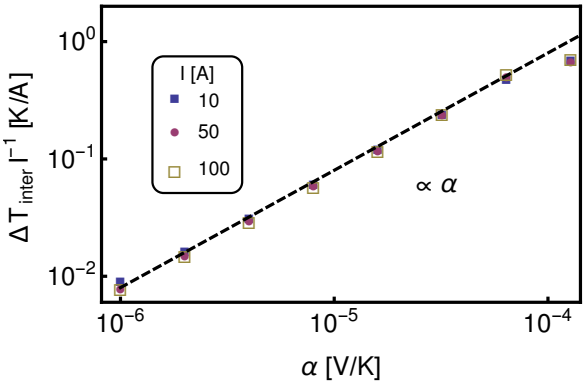

Figure 7.14: The temperature difference $\Delta T_{\mathrm{if}} = T_{\mathrm{if}} - T_e$ is proportional to the current I and to α.

mented thermoelectric, we find that the difference between interface temperature at the cold side $T_{\mathrm{if,c}}$ and electrode temperature T_e scales as $\Delta T_{\mathrm{if}} = T_{\mathrm{if,c}} - T_e \propto \alpha J_{\mathrm{oc}} \propto \alpha^2$. This is because the internal open circuit current density J_{oc} is proportional to α, which we confirmed for each bond at the interface. Note that the same relationship results from eq. (6.15) for the current circling in parallel thermoelectrics with open circuit conditions and $\alpha_A = -\alpha_B$. The relation between the voltage evoked by ΔT_{if} and α in open circuit conditions reads $U_{\mathrm{if,oc}} \propto \alpha \Delta T_{\mathrm{if}} \propto c_{\mathrm{oc}} \alpha^3$. For small α, the effect of $U_{\mathrm{if,oc}}$ on the total open circuit voltage U_{oc} is hardly notable. Just for $\alpha \gtrsim 10^{-4}\,\mathrm{V/K}$ deviations from the linear behavior are large enough to be recognized (see fig. 7.8), and we confirmed the influence of $U_{\mathrm{if,oc}}$ on U_{oc} by scrutinizing $U_{\mathrm{oc}} - \alpha \Delta T_{\mathrm{eff}}$. Presumably, the previously mentioned dependence of U_{oc} on σ enters via $U_{\mathrm{if,oc}}$, because a larger electrical conductivity enhances the electrical currents, which in turn enhances ΔT_{if}.

By attaching a load, the current passing the interface at the cold side is reduced. We observe that the temperature difference between interface and electrodes decreases linearly with the load current I. Accordingly,

$$U_{\mathrm{if}} = U_{\mathrm{if,oc}} + U_{\mathrm{if,I}} = c_{\mathrm{oc}} \alpha^3 - c_I \alpha^2 I \tag{7.13}$$

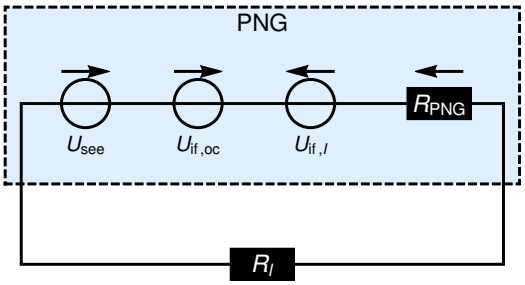

Figure 7.15: Thévenin equivalent of the PNG attached to a load R_l. Seebeck voltage U_{see} and the open circuit interface voltage $U_{if,oc}$ have the same sign. The voltage across the internal resistance R_{PNG} and the part of interface voltage depending on the external current, $U_{if,I}$, point in the opposite direction.

has two counteracting contributions depicted in fig. 7.15. Additionally, the Seebeck voltage U_{see} created from the temperature difference $T_h - T_c$ is superimposed and has the same sign as $U_{if,oc}$. The voltage across the internal resistance points in the opposite direction, as well as $U_{if,I}$. Note that $U_{if,oc}$, which is independent of I, affects U_{oc}, while $U_{if,I}$ is responsible for the quadratic increase of R_{eff} with α.

In summary, we can write the open circuit voltage as

$$U_{oc} = \alpha \Delta T_{eff} + c_{oc} \alpha^3, \tag{7.14}$$

where the second term is negligible for $\alpha \lesssim 10^{-4}$ and ΔT_{eff} depends on (L_y/L_x) (see eq. (7.10)). The effective resistance depends on the Seebeck coefficient as

$$R_{eff} = R_{PNG} + c_I \alpha^2. \tag{7.15}$$

Eventually, the power output of a PNG reads

$$P = (\alpha \Delta T_{eff} + c_{oc} \alpha^3) I - (R_{PNG} + c_I \alpha^2) I^2. \tag{7.16}$$

Deriving P_{max} based on eq. (7.16) leads to

$$\frac{P_{max}}{\alpha^2} = \frac{(\Delta T_{eff} + c_{oc} \alpha^2)^2}{4(R_{PNG} + c_I \alpha^2)}, \tag{7.17}$$

which elucidates the fact that P_{max}/α^2 depends on α.

Let us finally remark on the heat dissipation. In a 1d CPM RI^2 (see eq. (2.43)) can be derived by integrating j^2/σ over the volume. Here, summing up I_{ij}^2/G_{ij} over all bonds, we find

$$\sum_{ij} I_{ij}/G_{ij} = c_J \alpha^2 + R_{PNG} I^2. \tag{7.18}$$

Due to internal current vortices even for $I = 0$ heat is produced. The strength of internal currents is proportional to α, which is also found in parallel thermoelectric (see eq. (6.15)), leading to $c_J \alpha^2$. The current dependent term is proportional to the resistance R_{PNG} and not to R_{eff}.

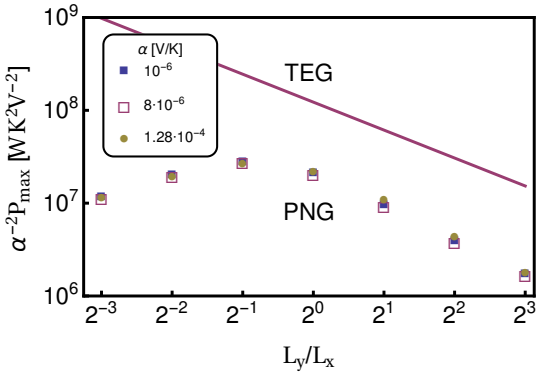

Figure 7.16: $P_{\max}$ is further maximized by an optimal shape $(L_y/L_x)_{\text{opt}} \approx 0.5$. The position of the maximum is independent of α. The red line is derived for a TEG.

7.3.6 *Shape optimization*

Figure 7.10 indicates the influence of the shape on the open circuit voltage. Now, our aim is to find an optimal ratio $(L_y/L_x)_{\text{opt}}$ with highest power output. Therefore, we consider the maximum power obtained by impedance matching

$$P_{\max} = U_{\text{oc}}^2/(4R_{\text{eff}}). \tag{7.19}$$

In fig. 7.16, we rescaled $P_{\max}$ by α^{-2}, which leads to a data collapse signifying that the optimal ratio $(L_y/L_x)_{\text{opt}} \approx 0.5$ is independent of α for $\alpha \leq 1.28 \cdot 10^{-4}\,\text{V/K}$. For small (L_y/L_x) the open circuit voltage reaches its maximum, but the resistance R_{eff} becomes larger as well, while in the opposing limit U_{oc} vanishes and R_{eff} saturates. Increasing (L_y/L_x) in an comparable TEG leads to the red line in fig. 7.16, which follows $(L_y/L_x)^{-1}$ due to the dependence of the resistance on L_y and is considerably higher than the PNG power $P_{\max}^{(\text{PNG})}$. One could ask, with which aspect ratio the power comes closest to the TEG performance. We find that $P_{\max}^{(\text{TEG})}/P_{\max}^{(\text{PNG})} = 5.5(1)$ for $L_y/L_x = 1$ is the smallest quotient.

For large Seebeck coefficients corrections discussed in sections 7.3.4 and 7.3.5 become relevant, and whether it has a positive impact on $P_{\max}^{(\text{PNG})}$ might depend on further parameters like heat conductivity and temperature, partly determining the interface temperature.

7.3.7 *Cut along the interface*

An apparent improvement is achieved by introducing a cut along the pn junction increasing U_{oc} and suppressing current vortices. We expect an optimal cutting length h_{opt} and are interested in how far it depends on system parameters. Beside simulation results experimental findings are presented.

To simulate the cut, we disconnect adjacent sites at the pn junction up to cutting height h (see inset of fig. 7.17). Considering $P_{\max}(h)$ (see fig. 7.17), we find that it is characterized by a maximum, which can

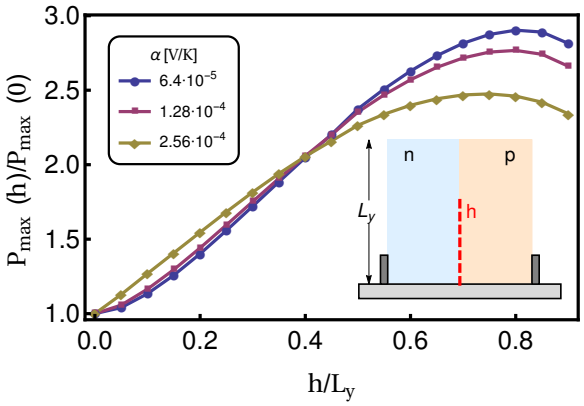

Figure 7.17: The simulated maximum power output $P_{\max}(h)/\alpha^2$ of a PNG in dependence of cutting height h/L_y for varying Seebeck coefficients. Note that the curves do not intersect in a single point, but in two which are close to each other.

be understood as a trade-off between rising resistance and increasing U_{oc}. The resistance tends towards infinity for $h/L_y \to 1$, while the Seebeck voltage almost reaches $2|\alpha|\Delta T$ as also identified in [168]. The open circuit voltage for $h = 0$, intensely discussed in section 7.3.2, is $U_{\text{oc}} \approx 0.7\alpha\Delta T$.

The Seebeck coefficient weakly influences the optimal cutting length h_{opt}. We also observe that α affects $P_{\max}(h_{\text{opt}})/P_{\max}(0)$, which reaches values between 2.4 and 2.9. Note that we detected a slight dependence of c_I and c_0 on h, which is not analyzed further in this thesis.

We also examined, whether further parameters affect position and height of maximum and found that ΔT and σ are insignificant. However, it turns out that the system shape is relevant. Due to the unfavorable electrochemical potential distributions for large (L_y/L_x) (see fig. 7.10), the performance of elongated PNGs can be improved strongly by cutting. Consequently, the power of a cut PNG with large (L_y/L_x) comes closer to the one of a comparable TEG. E. g. with $(L_y/L_x) = 2$ and optimal cut h_{opt} we find $P_{\max}^{(\text{PNG})}/P_{\max}^{(\text{TEG})} = 1.2(1)$. However, in terms of power long devices are unpreferable, and the highest power is obtained by optimizing a PNG with $(L_y/L_x) = 1$ yielding $P_{\max}^{(\text{PNG})}/P_{\max}^{(\text{TEG})} = 1.8(1)$.

We checked that the maximum efficiency does not show any significant differences compared to $P_{\max}(h)$ and the optimal cutting height for largest efficiency gain is $h \approx 0.8$ just as for the electrical power.

R. Chavez and J. Hall did the corresponding experiment [175, 23] by iteratively measuring and cutting a PNG. The experimental data show a maximum power output as well, where the peak position has a strong dependence on ΔT (see fig. 7.18). We attribute this to diode-like behavior of the interface, which will be discussed in the context of an extended simulation model (see section 7.5). A significant enhancement of the power output up to a factor of 3.5 is observed due to cutting in the experiment, where $L_y/L_x \approx 3$. Performing simulations with a similar shape, we almost find the same enhancement, although not all physics are covered by the underlying simulation model.

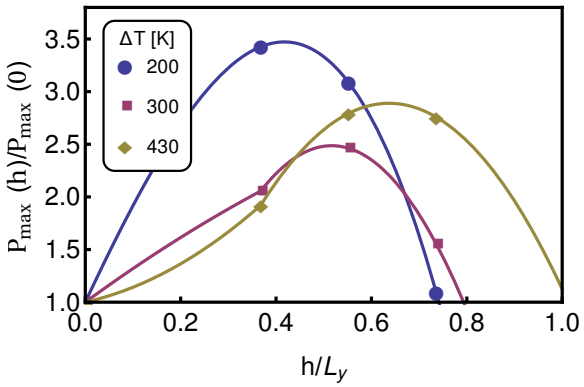

Figure 7.18: Experimental data of $P_{\max}(h/L_y)$ rescaled by the maximum power output of a uncut device for different temperatures. Lines serve as a guide to the eye.

7.3.8 *Heat current and efficiency*

For the sake of completeness, heat currents into and out of the PNG are discussed. Figure 7.19 shows the heat current at hot and cold side of a PNG and a TEG. As in the parallel structure, even for $I = 0$ internal currents are present, which flow such that they raise $I_{\mathrm{q,hot}}$ and $I_{\mathrm{q,cold}}$ in a PNG in comparison to a TEG. In a TEG with open circuit conditions, just Fourier heat is transported hot to cold. Compared to a TEG, the heat currents in the PNG hardly depend on I, which is due to the internal currents already apparent for $I = 0$.

The efficiency is further reduced by the larger heat flow. However, for some applications, larger heat currents may be desirable. E. g. in situations, where a certain amount of heat has to be dissipated as pointed out in [64].

For a thermoelectric cooler and heater, the electrical current has to transport heat from cold to hot. Since internal currents in a PNG counteract this endeavor, a PNG does not have potential as cooler or heater.

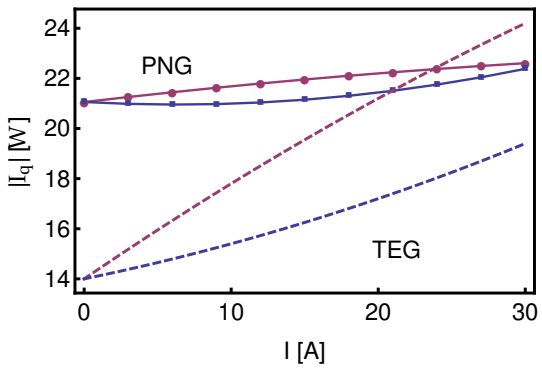

Figure 7.19: Heat current at hot (red) and cold side (blue) are shown for PNG (points and lines) and TEG (dashed lines) at $\Delta T = 700\,\mathrm{K}$.

A more realistic description of a PNG shall be achieved by taking into account pn junction characteristics. Before presenting an extended model, experimental results are summarized.

Parts of the this section have been published in [175, 110].

7.4.1 *Experimental findings*

Experimental investigations of the pn junctions revealed a complex interface structure influenced by particle structure and current-activated pressure-assisted sintering process.

Analysis of the spatially resolved Seebeck coefficient across the interface showed that p- and n-type particles form an intermixed region instead of a sharp interface [176]. Within this region, extending over approximately 100 μm, both particle types are present. In contrast, a sharp interface described by the Shottky model leads to small SCR in the order of $\sim$ 10 nm. The observed broader pn region is due to an intermixing of particles on a micrometer range. The intermixing may happen during the filling of the sinter die as well as during the sinter process itself as has been pointed out in section 4.3.3. Furthermore, overshoots of the Seebeck coefficient at the border of the interface region have been observed. Their occurrence is explained by (partially) melting of particles during CAPAD. If p- and n-doped particles coalesce, their dopants can partially compensate each other, creating regions with very low charge carrier concentration. Low carrier concentrations are related to high Seebeck coefficients observed in the experiment.

Moreover, an Optically Beam Induced Voltage (OBIV) technique was used to characterize the interface on a microscale. For an OBIV measurement the surface of a structure is excited by a light beam, typically a laser, and the voltage across the sample is measured. If the energy of the light exceeds the band gap, electron hole pairs are produced. They may recombine or, if they are created close to the SCR, can be separated, leading to an optically induced voltage. Hence, the OBIV measurement enables us to envision the pn junction, which is by no means a sharp interface, but its position varies over a couple of $\approx 10\mu$m. Additionally, the strength of the voltage indicates that the quality of the diode is strongly position dependent.

We emphasize that handling at atmospheric conditions engender a variety of impurities, which are accompanied by intraband states controlling the overall electrical behavior. The measurement of current-voltage characteristics reveals that diode and ohmic behavior are superimposed [177, 172, 23]. This is expressed by the equivalent circuit fig. 7.20 containing a diode and a shunt conductance. The appearance of a shunt conductance in non-ideal devices is attributed to leak currents, which appear scattered across the interface [178]. Centralizing them in a single conductance is a quite practical and helpful approach. The shunt originates from surface currents, grain bound-

ary effects and high number of gap states created by morphology defects and impurities [178, 177].

Different extensions to the equivalent circuit fig. 7.20 were proposed. As an example, a current source parallel to diode and shunt can be introduced to reflect contributions of charge carriers separated by the SCR. Such an equivalent circuit almost corresponds to those used for the description of solar cells, where charge carriers are excited by photons. Usually, a series resistance is added accounting for material beyond the SCR and metallic contacts. R. Chavez [23] suggested an extension by an additional non-linear shunt conductance, which implies a better description of his data.

7.4.2 *Model details*

For simplicity, we do not take into account the spatial distribution of the interface region and assume all diodes are of the same quality. In order to model a pn junction, we replace a bond connecting p- and n-type material by the structure shown in fig. 7.20. The static diode conductance is derived from the Shockley equation [166, 40]

$$j_d = j_0 \left(\exp\left(\frac{eU}{kT}\right) - 1 \right), \tag{7.20}$$

where U is the voltage across the SCR, k is the Boltzmann constant and e the elementary charge. We assume that the voltage between two sites constituting an interface, is completely dropped across the SCR. Of high importance is the temperature dependence of the saturation current j_0. Within the framework of the Shockley model it reads [166]

$$j_0 = aT^{3+\gamma/2} \exp\left(\frac{-E_g}{kT}\right), \tag{7.21}$$

where E_g is the band gap. In eq. (7.21) the exponential term is most significant, and we choose $\gamma = 2$ and $a = 0.01\,\mathrm{A/K^4}$. With those values as well as with reasonable temperature differences and band gaps, G_{pn} vanishes on the cold side, while it is in the order of the

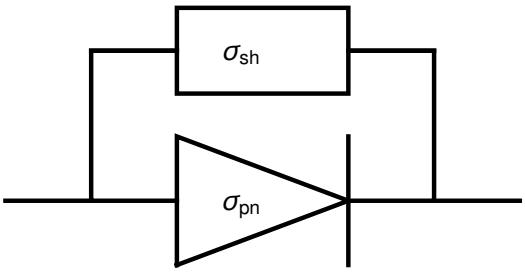

Figure 7.20: Each bond at the interface is replaced by the depicted shunt-diode structure, which is characterized by σ_{sh}, which is constant, and σ_{pn}, which depends on temperature and voltage.

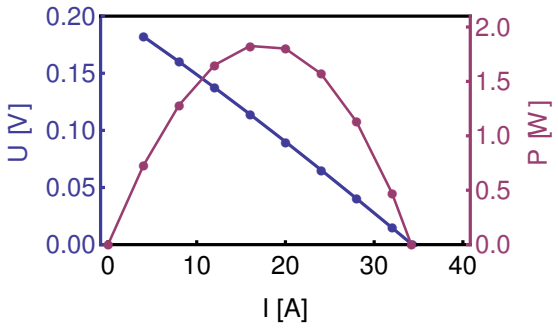

Figure 7.21: The current-voltage characteristic and the power $P(I)$ for $E_g = 0.6\,\mathrm{eV}$. In the power producing regime $P(I) > 0$, $I(U)$ is in most cases linear and the power is well described by a quadratic function. Parameters are taken from table 9. Moreover, we choose $\sigma_{\mathrm{sh}} = 10^6\,\mathrm{S/m^2}$, $T_h = 1000\,\mathrm{K}$ and $T_c = 300\,\mathrm{K}$.

bulk conductance on the hot side (see fig. 7.22). Now, the static conductance of the diode reads

$$G_{\mathrm{pn}} = a\bar{T}_{ij}^{3+\gamma/2} \exp\left(\frac{-E_g}{k\bar{T}_{ij}}\right)\left(\exp\left(\frac{eU_{ij}}{k\bar{T}_{ij}}\right) - 1\right)\frac{S_{\mathrm{pn}}}{U_{ij}}, \tag{7.22}$$

where $\bar{T}_{ij} = (T_i + T_j)/2$ and $U_{ij} = (\mu_i - \mu_j)/q$. $S_{\mathrm{pn}} = (L_y/N_y)(L_z/N_z)$ corresponds to the cross section area determined by the discretization. For simplicity, $G_{\mathrm{sh}} = \sigma_{\mathrm{sh}} S_{\mathrm{pn}}$ scales with the cross section area as well. Note that an additional series resistance is not taken into account.

Taking into account voltage dependent conductances implies that a system of non-linear equations has to be solved. We rely on the method on hand, and we solve the system iteratively. In the first iteration step, the potential distribution μ_i (i running over all nodes) is derived neglecting the diode. Subsequently, we solve the system eqs. (3.13) and (3.14) and update μ_i and G_{pn}. This process is repeated until the solution becomes stable. Thereby, the evolution of the variables should not to be misinterpreted as a time evolution.

7.4.3 *Influence of band gap and shunt conductance*

At first, we investigate the influence of the newly introduced parameters, band gap E_g and shunt conductivity σ_{sh}, on the electrical power. Further parameters are taken from table 9.

Again, we focus on P_{max}, and its determination requires $P(I)$. Due to the diodes, $P(I)$ can not be a quadratic function of I. However, in the power producing regime $P > 0$, an almost linear current-voltage characteristic is observed as shown exemplarily in fig. 7.21. R. Chavez [23] and A. Becker [172] obtained the same result in their experiments. The occurrence of the linear behavior is surprising, since voltages across the diodes are quite large and approximating the current-voltage characteristic of the diodes by a linear function is not feasible.

In order to understand of the device, we consider the conductances G_{pn} along the interface for fixed G_{sh} and different E_g and I (see

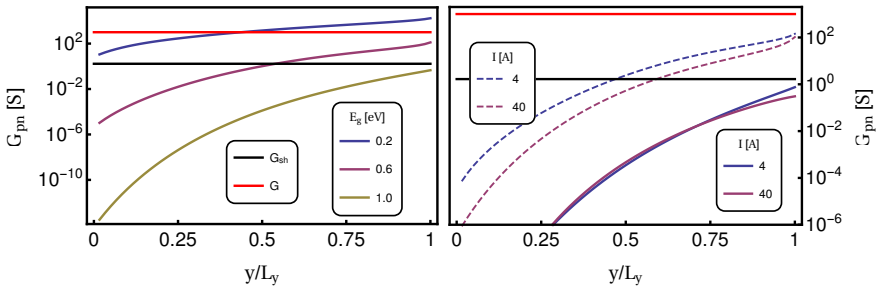

Figure 7.22: The conductance G_{pn} is plotted along the interface . The cold side is located at $y/L_y = 0$ and the hot side at $y/L_y = 1$. Furthermore, the shunt conductance G_{sh} (black) used in fig. 7.21 and the bulk bond conductance G (red) are shown. In the right figure, the dependence of G_{pn} on the current is indicated for $E_g = 0.6\,\mathrm{eV}$ (dashed lines) and $E_g = 1.0\,\mathrm{eV}$ (solid lines). The heat bath temperatures are $T_h = 1000\,\mathrm{K}$ and $T_c = 300\,\mathrm{K}$.

fig. 7.22). It is derived along the interface, where the cold side is located at $y/L_y = 0$ and the hot side at $y/L_y = 1$. We notice that the temperature increases the saturation current to such extent that diodes on the hot side conduct much better than diodes on the cold side, although diodes are reverse biased on the hot side. Considering the influence of the band gap (fig. 7.22, left), we recognize that for $E_g = 0.2\,\mathrm{eV}$ diodes are active ($G_{\mathrm{pn}} > G_{\mathrm{sh}}$) along the whole interface, while for large $E_g = 1.0\,\mathrm{eV}$ diodes are mainly bypassed. For intermediate band gaps, diodes on the cold side are inactive, while on the hot side $G_{\mathrm{pn}} > G_{\mathrm{sh}}$. This leads to an advantageous effect on P_{max} as discussed below. The effect of the electrical current I on G_{pn}, shown in fig. 7.22 (right) for $E_g = 0.6\,\mathrm{eV}$ (dashed lines) and $E_g = 1.0\,\mathrm{eV}$ (solid lines), is quite weak. In general, G_{pn} decreases with the electrical current, which is attributed to the fact that on the cold side more charge carriers flow out of the device lowering the forward biased voltage across the interface. Although G_{pn} for $E_g = 0.6\,\mathrm{eV}$ changes significantly with I, the position-dependent relation to G_{sh} and G is hardly affected. As a consequence, the current distribution for $I = 4\,\mathrm{A}$ and $I = 40\,\mathrm{A}$ are very similar and the total conductance of the PNG is almost independent of I.

In the following investigation of P_{max}, we use an interpolation to describe $P(I)$ and subsequently perform a numerical search for the maximum. Figure 7.23 displays P_{max} in dependence of E_g for different σ_{sh}. Three regions are recognized. First, for small E_g the diode is highly conductive, the current bypasses the shunt and hence, P_{max} becomes independent of σ_{sh}. Even though σ_{pn} decreases with E_g, the maximum power should saturate, since the total conductance is limited by the bulk conductance. For large $E_g \gtrsim 1\,\mathrm{eV}$ we observe that P_{max} is constant as well, because the diodes block across the whole interface, such that all current passes the shunt. Here, P_{max} is strongly influenced by σ_{sh}. In between, a complex interplay between σ_{pn} and σ_{sh} causes the shape of $P_{\mathrm{max}}(E_g)$, which is characterized by a maximum. With increasing E_g, the diode elements become less conductive, most notably on the cold side (see fig. 7.22). Consequently, the poten-

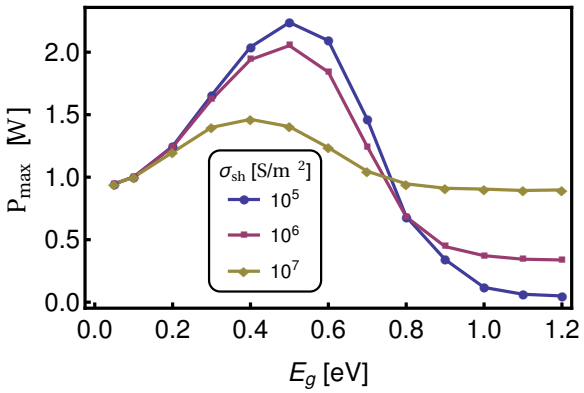

Figure 7.23: The influence of E_g and σ_{sh} on P_{max} is shown for $T_h = 1000\,\mathrm{K}$ and $T_c = 300\,\mathrm{K}$.

tial distribution evolves such that more current is flowing across the interface on the hot side, which is similar to the situation created by a cut. The mechanism leading to an enhancement by cutting is explained in section 7.3.7, and the same arguments apply here. For even larger E_g, σ_{pn} on the hot side is affected as well and P_{max} enters the regime, where σ_{sh} is relevant. The maximum is less pronounced for large σ_{sh}, since the cut like effect of the temperature dependence of σ_{pn} just works if σ_{sh} is small.

A comparable TEG with perfect electrical contacts delivers $P_{\mathrm{max}} = 4.9\,\mathrm{W}$, which is about a factor two larger than the best PNG in fig. 7.23. Thus, engineering the pn junction bears as much potential as introducing a cut.

7.4.4 *Influence of temperature difference*

Of great interest is the influence of the temperature difference ΔT on P_{max}. As shown before, for a TEG in CPM approximation the maximum power scales with ΔT. Even for real parameters, usually exhibiting moderate temperature dependence, just slight deviations from the quadratic behavior are observed. However, for the extended PNG model substantial differences are anticipated due to the exponential nature of the diode. As in the previous section, P_{max} is determined from an interpolating function. In subsequent investigations, we vary E_g and investigate the influence of the shunt.

The maximum power for three combinations of E_g and σ_{sh} is depicted in fig. 7.24. Each curve is characterized by three regimes. For low ΔT, P_{max} increases quadratically. The diode is highly resistive and all current is passing the shunt. That is why σ_{sh} strongly affects P_{max}. Here, σ_{sh} is significantly smaller than the bulk conductivity such that the PNG performs orders of magnitude worse than a TEG (black dashed line). Additionally, unfavorable effects caused by the geometry of the PNG as discussed in section 7.3 reduce the power. In an intermediate temperature regime, the diode is activated and the PNG substantially increases its power. This region is more pronounced for low σ_{sh} carrying more potential for improvement. Re-

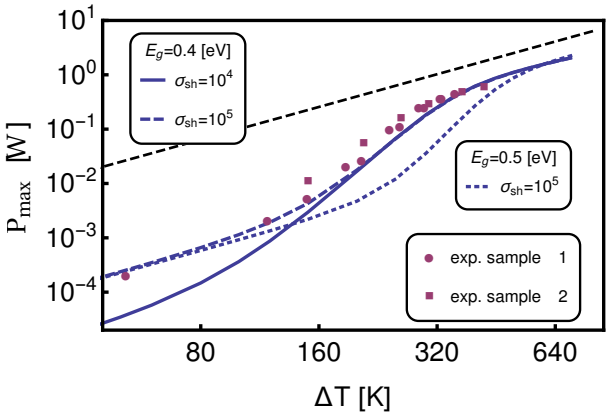

Figure 7.24: P_{max} is derived in dependence of ΔT and for $E_g = 0.4\,\text{eV}$, $E_g = 0.5\,\text{eV}$ as well as two shunt conductivities $\sigma_{sh} = 10^4\,\text{S/m}^2$ and $\sigma_{sh} = 10^5\,\text{S/m}^2$. Furthermore, experimental results are presented (red symbols). Note that experimental data are multiplied by 30 such that the same axis can be used. The black dashed line corresponds to P_{max} derived for a comparable TEG in the framework of a CPM.

sponsible for the location of this transition region is the band gap E_g and the shunt σ_{sh}: raising E_g or σ_{sh} shifts the onset of the strong increase to higher temperatures. However, despite the strong increase, P_{max} still undercuts the TEG power by a factor of 2-3. At higher temperatures $\Delta T > 400\,\text{K}$, both disperse even further, since a closer investigation reveals that P_{max} of the PNG rises weaker than ΔT^2. This observation is ascribed to the fact that diodes further away from the hot side become conductive with increasing T_h. This allows for a growth of unfavorable current vortices. The situation is similar to reducing the cut below the optimal cut length (see section 7.3.7). This explanation is illustrated by the the potential distribution $\mu(\vec{r})/q$ shown in fig. 7.25 for $E_g = 0.5\,\text{eV}$ and $\sigma_{sh} = 10^5\,\text{S/m}^2$. In the regime $200\,\text{K} \lesssim \Delta T \lesssim 350\,\text{K}$ ($T_h = 500\,\text{K}$ to $T_h = 750\,\text{K}$), we observe that the line of equal potential (dashed line) is shifted towards the hot side. There, diodes are conductive, while they are still blocked on the cold side. Note, that the potential distribution in fig. 7.25 (upper left to upper right) develops such that it becomes similar to a cut PNG. In the high temperature regime with $350\,\text{K} \lessapprox \Delta T$, we recognize that with increasing T_h the interface part with well conducting σ_{pn} shifts towards the cold side and $\mu(\vec{r})/q$ diverge from its optimal distribution.

In fig. 7.24 we also show experimentally measured maximum power from two different samples (red squares and points) and find a qualitative agreement between simulation and experiment. Note that experimental data are multiplied by 30 such that the same axis can be used. Although at low temperatures differences, only few data points are available, the three regimes can be recognized in experimental data as well. Due to different transport parameters, device dimensions and shape, experimental and simulational values deviate. Further differences, especially in the intermediate temperature regime, may also arise due to differing E_g and σ_{sh}.

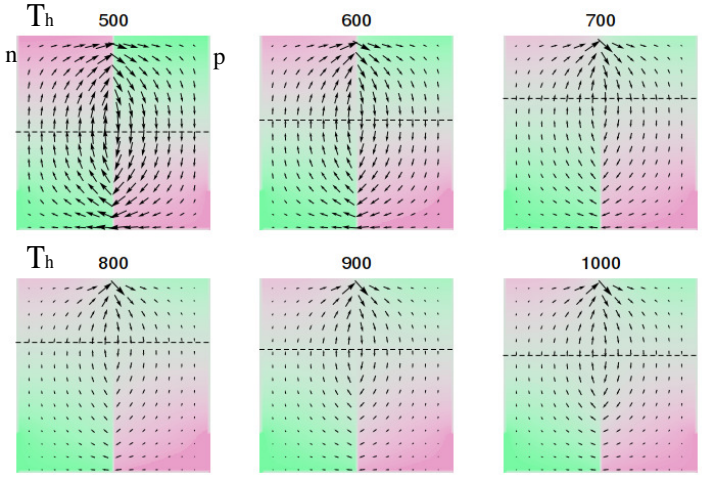

Figure 7.25: Potential distribution $\mu(\mathbf{r})/q$ and current distribution for various temperatures. $\mu(\mathbf{r})/q$ increases from green to pink and black arrows indicate current strength and direction. Note that the color coding for the potential reflects the relative potential variation in each figure and does not represent absolute values. The same is true for the size of the arrows. The dashed lines denote the height at which the potentials in p- and n-type legs are equal.

7.5 PN-GENERATOR VS. CONVENTIONAL DEVICE

Finally, we present a comparison between an experimental TEG and a PNG with nearly optimal cut length. As a reference we use a TEG built from the same source material as the PNG [174]. Since elevated temperatures were not accessible with the TEG, we show complementary simulation results. Therefore, we used temperature dependent parameters $\sigma(T), \alpha(T), \kappa(T)$ [62, 179], which were obtained from the same material as the TEG. Note that the simulations were performed at the same hot and cold side temperatures as the experiment with the PNG.

Both experimental generators have different geometries. To be comparable, we have to rescale $P_{\max}$ adequately. Often, $P_{\max}/S$ with cross section area S is used, instead of $P_{\max}$ itself. But this quantity still depends on L_y. Therefore, we propose a further quantity, which is independent of the geometry. It is defined as

$$p_{\max} := \frac{P_{\max} L_y}{S}. \tag{7.23}$$

For the CPM, eq. (7.23) corresponds to the power factor $\alpha^2\sigma$. This is not the case for the PNG as the conductance is not proportional to L_y^{-1}.

Fig. 7.26 shows $p_{\max}$ of the said generators. The experimental TEG and the simulated TEG are separated by an offset that results from parasitic losses in the experimental TEG, which are neglected in the simulation. Note that the experimental TEG contains the parasitic losses of 32 legs. For small ΔT the PNG performs about two orders of magnitude worse than the perfect TEG. A strong reduction

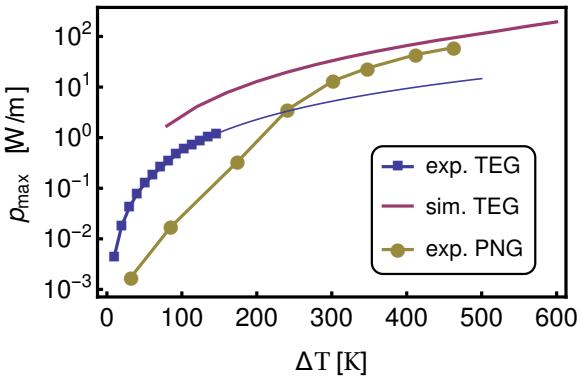

Figure 7.26: Comparison of the power output density of the cut PNG and TEG. Since experimental data available (blue points) just reach to $\Delta T \approx 180°C$ an ideal device (red line) is simulated covering the high temperature regime.

is also found in simulations of the PNG and are attributed to non-conducting diodes and low shunt conductivity (see section 7.4.4). Moreover, the unfavorable geometry of the PNG contribute to the bad performance. However, with increasing ΔT, the diode becomes more conductive and exceeds the extrapolated power of the experimental TEG (thin blue line). The extrapolation is obtained by fitting a quadratic function to the experimental TEG data. For large ΔT the PNG provides merely half of the power produced by the perfect simulated TEG. We want to stress, that the experimental accessible hot side temperature and hence ΔT are bounded for technical reasons, and in principle higher T_h can be applied to the PNG before degradation sets in.

Up to now, the presumably best performing generator is built from half-Heusler material and provides approximately $23000\,W/m^2$ at $\Delta T \approx 460\,K$ [180], which translates into $p_{max} = 69\,W/m$ just slightly more than the PNG built from nanostructured silicon with $p_{max} = 60\,W/m$ at $\Delta T = 463°C$.

7.6 CONCLUSION AND OUTLOOK

In this chapter, we presented an investigation of a new thermoelectric device geometry. The advantage of the new setup consists of the dismissal of hot side electrical contacts, which usually limit the application range of today's TEGs.

Our analysis was done in two steps: First, we used the basic Onsager network model to discretize a two-dimensional pn junction with attached electrodes. Interface effects are neglected, and the doping is just reflected by the Seebeck coefficients. We focused on the electrical power and showed that it can be described by a quadratic equation (see eq. (7.16)). Moreover, we explained the physical origin of its coefficients. Unfortunately, those coefficients are such that the PNG performs significantly worse than a TEG. A way to improve the performance consists of introducing a cut along the interface. We derived the optimal cutting length and understood its origin.

PNG	$P_{max}^{(TEG)}/P_{max}^{(PNG)}$
standard	5.4
cut	1.8
diode	2.1

Table 10: Comparison of P_{max} between PNG and TEG with perfect electric contacts on the hot side. For all cases we choose $T_h = 1000\,\mathrm{K}$ and $T_c = 300\,\mathrm{K}$. Results obtained with optimal cutting height are used. Concerning the advanced model we applied $E_g = 0.5\,\mathrm{eV}$ and $\sigma_{sh} = 1000\,\mathrm{S/m^2}$.

Second, an extended model was developed by replacing each pn interface bond by a diode-shunt structure. This model is able to reproduce experimental results qualitatively, especially the temperature dependence.

Throughout this chapter, we compared the maximum power output of the PNG to the CPM TEG with perfect contacts. We summarize them in table 10.

The model still lacks a lot of physics. The most interesting feature are the additional charge carriers, which are separated by the SCR as proposed by G. Span. They can be implemented phenomenologically by an additional current source at the interface, similarly to the solar cell description. But the strength of the current includes processes, which are out of the scope of the presented model. However, the importance of the additional current for systems based on nanostructuring has not been experimentally validated.

Another important aspect is the temperature dependence of the transport parameters. Especially the electrical conductivity can have a beneficial effect. By appropriate doping, solely extrinsic charge carriers are available on the cold side, while on the hot side additional intrinsic charge carriers implicate considerably higher electrical conductivity. This in turn leads to a metallic-like hot side, similar to a TEG structure, but without metal-semiconductor contact issues. The here presented model already offers the possibility to assign any temperature dependence to transport properties, but this possibility has not been explored yet.

Since the model used by G. Span takes into account more physics than the model presented in this work, one may ask what advantages are offered by a simpler model. We are not yet able to simulate and predict real devices properties. However, as we have shown in the present chapter, a lot of general aspects can be investigated separately of each other, which are not as clearly exposed when using a more detailed description. By increasing the complexity of the model stepwise, we are able to distinguish relevant features and already reached an qualitative agreement to experiments.

8

CONCLUSION

In this thesis we studied complex dynamics and performance of inhomogeneous thermoelectrics in various contexts using the phenomenological Onsager-de Groot-Callen theory. To carry out our research beyond the analytically accessible regime, we developed a network model on the basis of the aforementioned theory. The fruitful collaboration with an engineering group, building thermoelectric generators from scratch, motivated the application of our approach to distinct problems. We demonstrated that our network model is suitable to describe and support the development and investigation of inhomogeneous thermoelectrics.

In addition to the conclusions and summaries at the end of each chapter, here, we condense the main results.

At first we considered the current-activated pressure-assisted densification (CAPAD). We focused on the initial stage of the process, where partial melting and the related particle motion have a huge impact. With the lattice model, we elaborated on the influence of elongated pores on density and conductivity. Moreover, we indicated the similarities between our CAPAD model and the random fuse model. In binary mixtures consisting of particles with distinct Seebeck coefficients, we discovered self-organized structure formation. For small Seebeck coefficient differences segregation of particle types is observed, while for large Seebeck coefficient differences the occurrence of a checkerboard-like pattern occurs. Nonetheless, the segregation is partly enabled by somewhat unphysical low densities, which are caused by a large number of mobilized particles. Whether those effects can be found in the MD model or in an experiment is an open question.

Furthermore, we showed that the application of the Harman method to inhomogeneous media has substantial systematic errors. As a first example, we investigated segmented material and compared true open circuit values to Harman measurement results. We focused on the relevant limit of small currents and weak heat coupling to the environment, which enables an analytical description. The influence of the current, indispensable to the method, is memorized by the temperature distribution, which is self-organized such that the absolute value of the Seebeck coefficient is always overestimated. This in turn, leads to an overestimation of heat conductivity as well as figure of merit, which reaches up to 56% if the Seebeck coefficients differ by a factor 4. For segmented material, including superlattices, we were able to find correction terms. In two-dimensional random particle mixtures, we detected the same error around the percolation threshold.

For double segmented structures, we demonstrated that the temperature distribution, affected by the current, may either enhance or

decrease the electrical power of a generator in comparison to the power expected from open circuit transport coefficients. In most cases, the interface Peltier effect leads to a temperature distribution with decreased temperature drop across the material with the higher Seebeck coefficient, which results in a reduced electrical power. However, we calculated a parameter regime, in which superposition of Joule heating and Peltier cooling causes an enhancement of the power.

Eventually, we investigated a novel generator geometry, consisting basically of a pn junction, which facilitates its employment at high temperatures. We showed that this type of generator suffers from internal losses due to current vortices. For an ohmic interface, we were able to determine a phenomenological equation describing the dependency of the electrical power on the current, material properties and system dimensions. Moreover, we detected that a geometric optimization consisting of a cut along the interface lowers the internal losses to a large extent. In a next step, we introduced diode-shunt structures at the pn interface, which facilitated a qualitative description of experimental data. Finally, it was shown by an experiment that an optimized pn generator performs almost as good as a simulated conventional device, characterized by the same transport parameters. This is all the more promising, since the simulated conventional device does not suffer any parasitic losses.

A

APPENDIX A: SEGMENTED THERMOELECTRICS

Here, we show the calculation of the temperature distribution of a one-dimensional segmented thermoelectric. A similar calculation has been presented in [83].

The basic idea entails that in each segment i the temperature follows a parabolic function

$$T_i(x) = a_i x^2 + b_i x + c_i \quad \text{with} \quad a_i = -\frac{j^2}{2\sigma_i \kappa_i}. \tag{A.1}$$

The unknown b_i, c_i are derived from the requirement for continuous temperatures and heat currents at the interfaces:

$$T_i(x_i) = T_{i+1}(x_i) \quad \text{and} \quad j_{q,i}(x_i) = j_{q,i+1}(x_i). \tag{A.2}$$

Besides, we apply a constant electrical current density j. In section 3.2.2 we provide temperatures at x_1 and x_{n+1}. However, in order to mimic the Harman method, here we couple the segmented structure to a heat bath of temperature T_{HB} via the heat conductance $K_{\mathrm{env}} = \kappa_{\mathrm{env}} S/d$ with the cross section area S. Note that just Fourier heat is flowing through those connections. Figure A.1 depicts a superlattice setup with $n = 4$ layers of material A and B. The material/-electrode interface is located at x_1 and x_{n+1}. Let the length of each segment A be $d_A = 2fL/n$, while each segment of material B has the length $d_B = 2(1-f)L/n$, where $0 \leq f \leq 1$ represents the amount of material A. Now, the interfaces are located at

$$x_i = \begin{cases} \frac{i}{2} d_A + \left(\frac{i}{2} - 1\right) d_B & \text{if } i \text{ is even} \\ \frac{i-1}{2} \left(d_A + d_B\right) & \text{if } i \text{ is odd} \end{cases}. \tag{A.3}$$

Considering n layers, eq. (A.2) delivers $2(n+1)$ equations. Further conditions result from the boundary conditions $T(-d) = T_{\mathrm{HB}}$ and

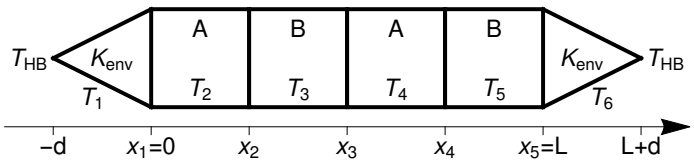

Figure A.1: An example of a superlattice with $n = 4$ layers consisting of material A and B. Furthermore, we consider a Fourier heat coupling of the segmented structure to the heat bath temperature T_{HB}.

$T(L+d) = T_{\mathrm{HB}}$. Applying a matrix formalism, the system of linear equations for the $2(n+2)$ unknown b_i, c_i reads

$$\begin{pmatrix} -d & 1 & 0 & 0 & \dots & \dots & \dots & \dots & 0 \\ x_1 & 1 & -x_1 & -1 & 0 & \dots & \dots & \dots & 0 \\ M_1(x_1) & 0 & -M_2(x_1) & -P_2 & 0 & \dots & \dots & \dots & 0 \\ 0 & 0 & x_2 & 1 & -x_2 & -1 & 0 & \dots & 0 \\ 0 & 0 & M_2(x_2) & P_2 & -M_3(x_2) & -P_3 & 0 & \dots & 0 \\ \dots & \dots & \dots & \dots & \dots & \dots & \dots & \dots & \dots \\ 0 & 0 & \dots & 0 & 0 & x_{n+1} & 1 & -x_{n+1} & -1 \\ 0 & 0 & \dots & 0 & 0 & M_{n+1}(x_{n+1}) & P_{n+1} & -M_{n+2}(x_{n+1}) & -P_{n+2} \\ 0 & 0 & \dots & 0 & 0 & 0 & 0 & -(L+d) & 1 \end{pmatrix} \begin{pmatrix} b_1 \\ c_1 \\ \dots \\ \dots \\ \dots \\ \dots \\ \dots \\ b_{n+2} \\ c_{n+2} \end{pmatrix} = \begin{pmatrix} T_{\mathrm{HB}} \\ Y_1 \\ Z_1 \\ \dots \\ \dots \\ \dots \\ Y_{n+1} \\ Z_{n+1} \\ T_{\mathrm{HB}} \end{pmatrix} \tag{A.4}$$

with

$$\begin{aligned} M_i(x_k) &= \alpha_i x_k j - \kappa_i \\ P_i &= \alpha_i j \\ Y_i &= (\alpha_{i+1} - \alpha_i) x_i^2 \\ Z_i &= (\alpha_{i+1} a_{i+1} - \alpha_i a_i) j x_i^2 + 2(\kappa_i a_i - \kappa_{i+1} a_{i+1}) x_i. \end{aligned}$$

Equation (A.4) can be solved by means of standard methods, e. g. using the algebra program Mathematica [181]. We obtain a piecewise function representing the temperature in each segment. From the temperature distribution we derive the Seebeck coefficient measured with the Harman method according to

$$\alpha'_{\mathrm{eff}} = \frac{\sum_{i=2}^{n+1} \alpha_i \left(T_i(x_i) - T_i(x_{i-1})\right)}{T_n(x_{n+1}) - T_2(x_1)}. \tag{A.5}$$

B

APPENDIX B: BASE UNITS

We derive the dimension of all relevant quantities in the base unit system used for the lattice model in section 4.3 following the ideas presented in [182].

We start with the usual SI base unit system $\{\mathcal{M}, \mathcal{L}, \mathcal{T}, \mathcal{I}, \mathcal{E}\}$ containing the dimensions of mass $\mathcal{M}$, length $\mathcal{L}$, time $\mathcal{T}$, current $\mathcal{I}$ and temperature $\mathcal{E}$. The dimension $\mathcal{A}$ of a deduced quantity A is given in the form $\mathcal{A} = \mathcal{M}^{e_1}\mathcal{L}^{e_2}\mathcal{T}^{e_3}\mathcal{I}^{e_4}\mathcal{E}^{e_5}$. In the matrix eq. (B.1), we summarize the dimensions of all relevant quantities using the exponents e_i

$$\mathfrak{U}_i = \begin{pmatrix} & \mathcal{M} & \mathcal{L} & \mathcal{T} & \mathcal{I} & \mathcal{E} \\ m & 1 & 0 & 0 & 0 & 0 \\ l & 0 & 1 & 0 & 0 & 0 \\ t & 0 & 0 & 1 & 0 & 0 \\ I & 0 & 0 & 0 & 1 & 0 \\ T & 0 & 0 & 0 & 0 & 1 \\ G & -1 & -2 & 3 & 2 & 0 \\ K & 1 & 2 & -3 & 0 & -1 \\ C & 1 & 2 & -2 & 0 & -1 \\ \alpha & 1 & 2 & -3 & -1 & -1 \end{pmatrix}. \tag{B.1}$$

First, instead of the mass, the heat capacity of a particle C shall be used in the base unit system. In the present base unit system the dimension of C is $\mathcal{C} = \mathcal{M}\mathcal{L}^2\mathcal{T}^{-2}\mathcal{E}^{-1}$, from which we can derive the dimensions of the mass in the $\{\mathcal{C}, \mathcal{L}, \mathcal{T}, \mathcal{I}, \mathcal{E}\}$ base system. The matrix

$$\mathfrak{P} = \begin{pmatrix} & \mathcal{C} & \mathcal{L} & \mathcal{T} & \mathcal{I} & \mathcal{E} \\ \mathcal{M} & 1 & -2 & 2 & 0 & 1 \\ \mathcal{L} & 0 & 1 & 0 & 0 & 0 \\ \mathcal{T} & 0 & 0 & 1 & 0 & 0 \\ \mathcal{I} & 0 & 0 & 0 & 1 & 0 \\ \mathcal{E} & 0 & 0 & 0 & 0 & 1 \end{pmatrix}, \tag{B.2}$$

enables a change of the base unit system. By the multiplication $\mathfrak{U}_i \cdot \mathfrak{P}$ we gain the exponents e_i in the $\{\mathcal{C}, \mathcal{L}, \mathcal{T}, \mathcal{I}, \mathcal{E}\}$ base unit system. In a

similar way, we replace time by heat conductance and electric current by electric conductance resulting in the following exponents

$$\mathfrak{U}_f = \begin{pmatrix} & \mathcal{C} & \mathcal{L} & \mathcal{K} & \mathcal{G} & \mathcal{E} \\ m & 3 & -2 & -2 & 0 & 1 \\ l & 0 & 1 & 0 & 0 & 0 \\ t & 1 & 0 & -1 & 0 & 0 \\ I & 0 & 0 & \frac{1}{2} & \frac{1}{2} & \frac{1}{2} \\ T & 0 & 0 & 0 & 0 & 1 \\ G & 0 & 0 & 0 & 1 & 0 \\ K & 0 & 0 & 1 & 0 & 0 \\ C & 1 & 0 & 0 & 0 & 0 \\ \alpha & 0 & 0 & \frac{1}{2} & -\frac{1}{2} & -\frac{1}{2} \end{pmatrix}. \tag{B.3}$$

Now, we derive the dimension of all relevant quantities in the base unit system used for the MD model in section 4.4. We start with

$$\mathfrak{U}_i = \begin{pmatrix} & \mathcal{M} & \mathcal{L} & \mathcal{T} & \mathcal{I} & \mathcal{E} \\ m & 1 & 0 & 0 & 0 & 0 \\ l & 0 & 1 & 0 & 0 & 0 \\ t & 0 & 0 & 1 & 0 & 0 \\ I & 0 & 0 & 0 & 1 & 0 \\ T & 0 & 0 & 0 & 0 & 1 \\ k_{n/t} & 1 & 0 & -2 & 0 & 0 \\ G & -1 & -2 & 3 & 2 & 0 \\ K & 1 & 2 & -3 & 0 & -1 \\ C & 1 & 2 & -2 & 0 & -1 \\ p & 1 & 0 & -2 & 0 & 0 \end{pmatrix} \tag{B.4}$$

The time is replaced by the force and the mass by the material density, which results in

$$\mathfrak{U}_f = \begin{pmatrix} & \subset & \mathcal{L} & \mathcal{F} & \mathcal{I} & \mathcal{E} \\ m & 1 & 2 & 0 & 0 & 0 \\ l & 0 & 1 & 0 & 0 & 0 \\ t & \frac{1}{2} & \frac{3}{2} & -\frac{1}{2} & 0 & 0 \\ I & 0 & 0 & 0 & 1 & 0 \\ T & 0 & 0 & 0 & 0 & 1 \\ k_{n/t} & 0 & -1 & 1 & 0 & 0 \\ G & \frac{1}{2} & \frac{1}{2} & -\frac{3}{2} & 2 & 0 \\ K & -\frac{1}{2} & -\frac{1}{2} & \frac{3}{2} & 0 & -1 \\ C & 0 & 1 & 1 & 0 & -1 \\ p & 0 & -1 & 1 & 0 & 0 \end{pmatrix}. \tag{B.5}$$

C

APPENDIX C: PISTON POSITION

In this section, we derive the time dependence of the piston position and the piston velocity assuming that a shock compaction takes place.

The front velocity of the compacted region reads

$$v_f = v\left(1 + \frac{\rho_0}{\rho_d}\right), \tag{C.1}$$

where $v = \dot{y}$ is the piston velocity, ρ_0 the initial and ρ_d the density of the compacted region. Assuming ρ_0 is homogeneous, the mass of the material moving with the piston changes as

$$\dot{m} = A\rho_0 v_f = \dot{y}\left(1 + \frac{\rho_0}{\rho_d}\right) A, \tag{C.2}$$

where A is the piston area. The mass

$$m(t) = \left(1 + \frac{\rho_0}{\rho_d}\right) \rho_0 A\tilde{y} + m_0 \tag{C.3}$$

includes the piston mass m_0 and increases linearly with $\tilde{y}$, the distance covered by the piston since starting the compression. For the equation of motion of the piston

$$(p - p_0)A = \dot{m}\dot{\tilde{y}} + m\ddot{\tilde{y}} \tag{C.4}$$

we have to take into account the consolidation pressure p_0 up to which the cohesive powder withstands external forces. Letting the initial piston position be $y(t = 0) = L_y$ and assuming that the piston moves downwards we obtain

$$\begin{aligned} y(t) &= L_y - \tilde{y}(t) \\ &= L_y + \tilde{L} - \sqrt{\tilde{L}^2 + \frac{ft^2}{\tilde{\rho}}} \quad \text{with} \\ \tilde{L} &= L_y \frac{\rho_d}{\rho_d + \rho_0} \\ \tilde{\rho} &= \left(1 + \frac{\rho_0}{\rho_d}\right) \rho_0. \end{aligned} \tag{C.5}$$

The piston velocity reads

$$v(t) = \dot{y}(t) = -\frac{\frac{f}{\tilde{\rho}} t}{\left(\tilde{L} + \frac{f}{\tilde{\rho}} t^2\right)^{1/2}}. \tag{C.6}$$

BIBLIOGRAPHY

[1] L. E. Bell. Cooling, heating, generating power, and recovering waste heat with thermoelectric systems. *Science*, 321:1457, 2008.

[2] Lawrence Livermore National Laboratory. Estimated U.S. energy use in 2014. `https://flowcharts.llnl.gov/content/assets/images/energy/us/Energy_US_2014.png`, visited: 2015-12-23.

[3] A. Shakouri. Recent developments in semiconductor thermoelectric physics and materials. *Annu. Rev. Mater. Res.*, 41(1):399, 2011.

[4] J. Yang. Potential applications of thermoelectric waste heat recovery in the automotive industry. In *24th International Conference on Thermoelectrics, 2005. ICT 2005*, pages 170–174, 2005.

[5] Fraunhofer IPM. Projekt HeatReCar - Thermoelectric waste heat recovery in light duty trucks. `http://www.ipm.fraunhofer.de/de/gf/funktionelle-materialien-systeme/anw/energyharvesting/heatrecar.html`,visited: 2016-02-15.

[6] K. Qiu and A. C. S. Hayden. Development of a thermoelectric self-powered residential heating system. *J. Power Sources*, 180(2):884, 2008.

[7] Biolite Inc. Biolite campstove. `http://www.biolitestove.com/products/biolite-campstove`,visited:2016-02-16.

[8] D. Champier, J. P. Bédécarrats, T. Kousksou, M. Rivaletto, F. Strub, and P. Pignolet. Study of a TE (thermoelectric) generator incorporated in a multifunction wood stove. *Energy*, 36(3):1518, 2011.

[9] S. LeBlanc. Thermoelectric generators: Linking material properties and systems engineering for waste heat recovery applications. *Sustainable Mater. Technol.*, 1-2:26, 2014.

[10] A. Moser, M. Erd, M. Kostic, K. Cobry, M. Kroener, and P. Woias. Thermoelectric energy harvesting from transient ambient temperature gradients. *J. Electron. Mater.*, 41(6):1653, 2012.

[11] NASA. Voyager - The Interstellar Mission. `http://voyager.jpl.nasa.gov/`,visited: 2016-02-15.

[12] R. C. O'Brien, R. M. Ambrosi, N. P. Bannister, S. D. Howe, and H. V. Atkinson. Safe radioisotope thermoelectric generators and heat sources for space applications. *J. Nucl. Mater.*, 377(3):506, 2008.

[13] I. Chowdhury, R. Prasher, K. Lofgreen, G. Chrysler, S. Narasimhan, R. Mahajan, D. Koester, R. Alley, and R. Venkatasubramanian. On-chip cooling by superlattice-based thin-film thermoelectrics. *Nat. Nanotechnol.*, 4(4):235, 2009.

[14] L. D. Hicks and M. S. Dresselhaus. Effect of quantum-well structures on the thermoelectric figure of merit. *Phys. Rev. B*, 47(19):12727, 1993.

[15] Glen A. Slack. New materials and performance limits for thermoelectric cooling. In *CRC Handbook of Thermoelectrics*. CRC Press, 1995.

[16] G. Jeffrey S. and E. S. Toberer. Complex thermoelectric materials. *Nat. Mater.*, 7(2):105, 2008.

[17] R. Venkatasubramanian, E. Siivola, T. Colpitts, and B. O'Quinn. Thin-film thermoelectric devices with high room-temperature figures of merit. *Nature*, 413(6856):597, 2001.

[18] K. Biswas, J. He, I. D. Blum, Chun-I. Wu, T. P. Hogan, D. N. Seidman, V. P. Dravid, and M. G. Kanatzidis. High-performance bulk thermoelectrics with all-scale hierarchical architectures. *Nature*, 489(7416):414, 2012.

[19] G. Schierning. Silicon nanostructures for thermoelectric devices: A review of the current state of the art. *Phys. Status Solidi A*, 211(6):1235, 2014.

[20] G. J. Snyder. Application of the compatibility factor to the design of segmented and cascaded thermoelectric generators. *Appl. Phys. Lett.*, 84(13):2436, 2004.

[21] P. H. Ngan, D. V. Christensen, G. J. Snyder, L. T. Hung, S. Linderoth, N. V. Nong, and N. Pryds. Towards high efficiency segmented thermoelectric unicouples. *Phys. Status Solidi A*, 211(1):9, 2014.

[22] G. Span, M. Wagner, T. Grasser, and L. Holmgren. Miniaturized TEG with thermal generation of free carriers. *Phys. Status Solidi RRL*, 1(6):241, 2007.

[23] R. Chavez. *High Temperature Thermoelectric Device Concept Using Large Area PN Junctions*. Dissertation, Universität Duisburg-Essen, 2015.

[24] H. B. Callen. The application of Onsager's reciprocal relations to thermoelectric, thermomagnetic, and galvanomagnetic effects. *Phys. Rev.*, 73(11):1349, 1948.

[25] S. R. de Groot and P. Mazur. *Non-equilibrium thermodynamics*. North-Holland Publishing Co., 1969.

[26] L. Onsager. Reciprocal relations in irreversible processes. I. *Phys. Rev.*, 37(4):405, 1931.

[27] L. Onsager. Reciprocal relations in irreversible processes. II. *Phys. Rev.*, 38(12):2265, 1931.

[28] D. Kondepudi and I. Prigogine. *From Heat Engines to Dissipative Structures*. John Wiley & Sons, 1998.

[29] R. R. Heikes and R. W. Ure. *Thermoelectricity: science and engineering*. Interscience Publishers, 1961.

[30] C. A. Domenicali. Irreversible thermodynamics of thermoelectricity. *Rev. Mod. Phys.*, 26(2):237, 1954.

[31] R. Becker. *Theorie der Wärme*. Springer Verlag Berlin Heidelberg, 1966.

[32] C. Goupil, W. Seifert, K. Zabrocki, E. Müller, and G. J. Snyder. Thermodynamics of thermoelectric phenomena and applications. *Entropy*, 13(8):1481, 2011.

[33] C. A. Domenicali. Stationary temperature distribution in an electrically heated conductor. *J. Appl. Phys.*, 25(10):1310, 1954.

[34] T. P. Hogan and T. Shih. Modeling and characterization of power generation modules based on bulk materials. In *CRC Thermoelectrics Handbook: Macro to Nano*. CRC Press, 2006.

[35] S. Datta. *Electronic Transport in Mesoscopic Systems*. Cambridge University Press, 1997.

[36] S. Datta. *Lessons from Nanoelectronics: A New Perspective on Transport*. World Scientific Publishing Company, 2012.

[37] M. Lundstrom, C. Jeong, and R. Kim. *Near-Equilibrium Transport: Fundamentals and Applications*. World Scientific Publishing Company, 2013.

[38] A. F. Joffe and L. S. Stil'bans. Physical problems of thermoelectricity. *Rep. Prog. Phys.*, 22(1):167, 1959.

[39] A. J. Minnich, M. S. Dresselhaus, Z. F. Ren, and G. Chen. Bulk nanostructured thermoelectric materials: current research and future prospects. *Energy Environ. Sci.*, 2(5):466, 2009.

[40] H. Ibach and H. Lüth. *Festkorperphysik*. Springer Verlag Berlin Heidelberg, 1988.

[41] M. S. Dresselhaus, G. Chen, M. Y. Tang, R. G. Yang, H. Lee, D. Z. Wang, Z. F. Ren, J.-P. Fleurial, and P. Gogna. New directions for low-dimensional thermoelectric materials. *Adv. Mater.*, 19(8):1043, 2007.

[42] E. S. Toberer, A. F. May, and G. J. Snyder. Zintl chemistry for designing high efficiency thermoelectric materials. *Chem. Mater.*, 22(3):624, 2010.

[43] P. Rogl. Formation and crystal chemistry of clathrates. In *CRC Thermoelectrics Handbook: Macro to Nano*. CRC Press, 2005.

[44] H. Kleinke. New bulk materials for thermoelectric power generation: Clathrates and complex antimonides. *Chem. Mater.*, 22(3):604, 2010.

[45] M. Christensen, A. B. Abrahamsen, N. B. Christensen, F. Juranyi, N. H. Andersen, K. Lefmann, J. Andreasson, C. R. H. Bahl, and B. B. Iversen. Avoided crossing of rattler modes in thermoelectric materials. *Nat. Mater.*, 7(10):811, 2008.

[46] C. B. Vining. Thermoelectrics: Half-full glasses. *Nat. Mater.*, 7(10):765, 2008.

[47] A. Saramat, G. Svensson, A. E. C. Palmqvist, C. Stiewe, E. Mueller, D. Platzek, S. G. K. Williams, D. M. Rowe, J. D. Bryan, and G. D. Stucky. Large thermoelectric figure of merit at high temperature in Czochralski-grown clathrate $Ba_8Ga_{16}Ge_{30}$. *J. Appl. Phys.*, 99(2):023708, 2006.

[48] C. Uher. Skutterudite-based thermoelectrics. In *CRC Thermoelectrics Handbook: Macro to Nano*. CRC Press, 2005.

[49] X. Shi, J. Yang, J. R. Salvador, M. Chi, J. Y. Cho, H. Wang, S. Bai, J. Yang, W. Zhang, and L. Chen. Multiple-filled skutterudites: High thermoelectric figure of merit through separately optimizing electrical and thermal transports. *J. Am. Chem. Soc.*, 133(20):7837, 2011.

[50] L.-D. Zhao, S.-H. Lo, Y. Zhang, H. Sun, G. Tan, C. Uher, C. Wolverton, V. P. Dravid, and M. G. Kanatzidis. Ultralow thermal conductivity and high thermoelectric figure of merit in SnSe crystals. *Nature*, 508(7496):373, 2014.

[51] L. D. Hicks, T. C. Harman, and M. S. Dresselhaus. Use of quantum well superlattices to obtain a high figure of merit from nonconventional thermoelectric materials. *Appl. Phys. Lett.*, 63(23):3230, 1993.

[52] L. D. Hicks, T. C. Harman, X. Sun, and M. S. Dresselhaus. Experimental study of the effect of quantum-well structures on the thermoelectric figure of merit. *Phys. Rev. B*, 53(16):R10493, 1996.

[53] R. Kim, S. Datta, and M. S. Lundstrom. Influence of dimensionality on thermoelectric device performance. *J. Appl. Phys.*, 105(3):034506, 2009.

[54] G. D. Mahan and J. O. Sofo. The best thermoelectric. *Proc. Natl. Acad. Sci. USA*, 93(15):7436, 1996.

[55] J. P. Heremans, V. Jovovic, E. S. Toberer, A. Saramat, K. Kurosaki, A. Charoenphakdee, S. Yamanaka, and G. J. Snyder. Enhancement of thermoelectric efficiency in PbTe by distortion of the electronic density of states. *Science*, 321(5888):554, 2008.

[56] C. J. Vineis, A. Shakouri, A. Majumdar, and M. G. Kanatzidis. Nanostructured thermoelectrics: Big efficiency gains from small features. *Adv. Mater.*, 22(36):3970, 2010.

[57] A. I. Boukai, Y. Bunimovich, J. Tahir-Kheli, J.-K Yu, W. A. Goddard Iii, and J. R. Heath. Silicon nanowires as efficient thermoelectric materials. *Nature*, 451(7175):168, 2008.

[58] A. I. Hochbaum, R. Chen, R. D. Delgado, W. Liang, E. C. Garnett, M. Najarian, A. Majumdar, and P. Yang. Enhanced thermoelectric performance of rough silicon nanowires. *Nature*, 451(7175):163, 2008.

[59] B. Poudel, Q. Hao, Y. Ma, Y. Lan, A. Minnich, B. Yu, X. Yan, D. Wang, A. Muto, D. Vashaee, X. Chen, J. Liu, M. S. Dresselhaus, G. Chen, and Z. Ren. High-thermoelectric performance of nanostructured bismuth antimony telluride bulk alloys. *Science*, 320(5876):634, 2008.

[60] N. Petermann, N. Stein, G. Schierning, R. Theissmann, B. Stoib, M. S Brandt, C. Hecht, C. Schulz, and H. Wiggers. Plasma synthesis of nanostructures for improved thermoelectric properties. *J. Phys. D: Appl. Phys.*, 44(17):174034, 2011.

[61] S. K. Bux, R. G. Blair, P. K. Gogna, H. Lee, G. Chen, M. S. Dresselhaus, R. B. Kaner, and J.-P. Fleurial. Nanostructured bulk silicon as an effective thermoelectric material. *Adv. Funct. Mater.*, 19(15):2445, 2009.

[62] G. Schierning, R. Theissmann, N. Stein, N. Petermann, A. Becker, M. Engenhorst, V. Kessler, M. Geller, A. Beckel, H. Wiggers, and R. Schmechel. Role of oxygen on microstructure and thermoelectric properties of silicon nanocomposites. *J. Appl. Phys.*, 110(11):113515, 2011.

[63] N. Stein, N. Petermann, R. Theissmann, G. Schierning, R. Schmechel, and H. Wiggers. Artificially nanostructured n-type SiGe bulk thermoelectrics through plasma enhanced growth of alloy nanoparticles from the gas phase. *J. Mater. Res.*, 26(15):1872, 2011.

[64] D. Narducci. Do we really need high thermoelectric figures of merit? A critical appraisal to the power conversion efficiency of thermoelectric materials. *Appl. Phys. Lett.*, 99(10):102104, 2011.

[65] J. M. O. Zide, D. Vashaee, Z. X. Bian, G. Zeng, J. E. Bowers, A. Shakouri, and A. C. Gossard. Demonstration of electron filtering to increase the Seebeck coefficient in $In_{0.53}Ga_{0.47}As/In_{0.53}Ga_{0.28}Al_{0.19}As$ superlattices. *Phys. Rev. B*, 74(20):205335, 2006.

[66] M. Bachmann, M. Czerner, and C. Heiliger. Ineffectiveness of energy filtering at grain boundaries for thermoelectric materials. *Phys. Rev. B*, 86(11):115320, 2012.

[67] W. Seifert, E. Müller, and S. Walczak. Generalized analytic one-dimensional description of non-homogeneous TE cooler and generator elements based on the compatibility approach. In *25th International Conference on Thermoelectrics, 2006. ICT '06*, pages 714–719, 2006.

[68] G. J. Snyder, E. S. Toberer, R. Khanna, and W. Seifert. Improved thermoelectric cooling based on the Thomson effect. *Phys. Rev. B*, 86(4):045202, 2012.

[69] K. Zabrocki, E. Müller, and W. Seifert. One-dimensional modeling of thermogenerator elements with linear material profiles. *J. Electron. Mater.*, 39(9):1724, 2010.

[70] I. Webman, J. Jortner, and M. H. Cohen. Thermoelectric power in inhomogeneous materials. *Phys. Rev. B*, 16(6):2959, 1977.

[71] X. Kleber, L. Simonet, F. Fouquet, and M. Delnondedieu. Thermoelectric power of a two-dimensional metal/metal composite: a numerical approach. *Model. and Simul. Mater. Sci. Eng.*, 13(3):341, 2005.

[72] F. Gather, C. Heiliger, and P. J. Klar. Modeling of interface roughness in thermoelectric composite materials. *J. Phys. Condens. Matter*, 23(33):335301, 2011.

[73] F. Gather, C. Heiliger, and P. J. Klar. NeMo: a network model program for analyzing the thermoelectric properties of meso and nanostructured composite materials. *Prog. Solid State Chem.*, 39(3-4):97, 2011.

[74] A. Becker, S. Angst, A. Schmitz, M. Engenhorst, J. Stötzel, D. Gautam, H. Wiggers, D. E. Wolf, G. Schierning, and R. Schmechel. The effect of Peltier heat during current activated densification. *Appl. Phys. Lett.*, 101(1):013113, 2012.

[75] G. K. Wachutka. Rigorous thermodynamic treatment of heat generation and conduction in semiconductor device modeling. *IEEE Trans. Comput.-Aided Design Integr. Circuits Syst.*, 9(11):1141, 1990.

[76] J. L. Pérez-Aparicio, R. Palma, and R. L. Taylor. Finite element analysis and material sensitivity of Peltier thermoelectric cells coolers. *Int. J. Heat Mass Transfer*, 55(4):1363, 2012.

[77] S. Angst and D. E. Wolf. Network theory for inhomogeneous thermoelectrics. *New J. Phys.*, 18(4):043004, 2016.

[78] D. M. Rowe. General principles and basic considerations. In *CRC Thermoelectrics Handbook: Macro to Nano*. CRC Press, 2005.

[79] H. A. Knudsen and S. Fazekas. Robust algorithm for random resistor networks using hierarchical domain structure. *J. Comput. Phys.*, 211(2):700, 2006.

[80] P. Gottschling and D. Lindbo. Generic compressed sparse matrix insertion: Algorithms and implementations in MTL4 and FEniCS. In *Proceedings of the 8th Workshop on Parallel/High-Performance Object-Oriented Scientific Computing*. ACM, 2009.

[81] W. H. Press, S. A. Teukolsky, W. T. Vetterling, and B. P. Flannery. *Numerical Recipes in C: The Art of Scientific Computing*. Cambridge University Press, 1992.

[82] M. Zebarjadi, A. Shakouri, and K. Esfarjani. Thermoelectric transport perpendicular to thin-film heterostructures calculated using the monte carlo technique. *Phys. Rev. B*, 74(19):195331, 2006.

[83] E. Müller, S. Walczak, and W. Seifert. Optimization strategies for segmented Peltier coolers. *Phys. Status Solidi A*, 203(8):2128.

[84] Y. Yang, S. H. Xie, F. Y. Ma, and J. Y. Li. On the effective thermoelectric properties of layered heterogeneous medium. *J. Appl. Phys.*, 111(1):013510, 2012.

[85] O. Guillon, J. Gonzalez-Julian, B. Dargatz, T. Kessel, G. Schierning, J. Räthel, and M. Herrmann. Field-assisted sintering technology/spark plasma sintering: mechanisms, materials, and technology developments. *Adv. Eng. Mater.*, 16(7):830, 2014.

[86] J. E. Garay. Current-activated, pressure-assisted densification of materials. *Ann. Rev. Mater. Res.*, 40(1):445, 2010.

[87] R. Orrù, R. Licheri, A. M. Locci, A. Cincotti, and G. Cao. Consolidation/synthesis of materials by electric current activated/assisted sintering. *Mater. Sci. Eng. R-Rep.*, 63(4-6):127, 2009.

[88] V. Kessler. *Hochtemperaturstabile thermoelektrische Generatoren auf Basis von nanokristallinem Silizium*. Dissertation, Universität Duisburg-Essen, 2014.

[89] K. Morita, B.-N. Kim, K. Hiraga, and H. Yoshida. Fabrication of high-strength transparent MgAl2o4 spinel polycrystals by optimizing spark-plasma-sintering conditions. *J. Mater. Res.*, 24(09):2863, 2009.

[90] R. Chaim, R. Marder-Jaeckel, and J. Z. Shen. Transparent YAG ceramics by surface softening of nanoparticles in spark plasma sintering. *Mat. Sci. Eng. A-Struct*, 429(1-2):74, 2006.

[91] R. Chaim. Densification mechanisms in spark plasma sintering of nanocrystalline ceramics. *Mat. Sci. Eng. A-Struct*, 443(1-2):25, 2007.

[92] R. Marder, C. Estournès, G. Chevallier, and R. Chaim. Plasma in spark plasma sintering of ceramic particle compacts. *Scr. Mater.*, 82:57, 2014.

[93] L. Wang, V. Pouchly, K. Maca, Z. Shen, and Y. Xiong. Intensive particle rearrangement in the early stage of spark plasma sintering process. *J. Asian Ceram. Societies*, 3(2):183, 2015.

[94] J. Guyon, A. Hazotte, J. P. Monchoux, and E. Bouzy. Effect of powder state on spark plasma sintering of TiAl alloys. *Intermetallics*, 34:94, 2013.

[95] Ke Hu, Xiaoqiang Li, Shengguan Qu, and Yuanyuan Li. Spark-Plasma Sintering of w-5.6ni-1.4fe heavy alloys: Densification and grain growth. *Metall. Mat. Trans. A*, 44(2):923, 2012.

[96] M. Herrmann, Z. Shen, I. Schulz, J. Hu, and B. Jancar. Silicon nitride nanoceramics densified by dynamic grain sliding. *J. Mater. Res.*, 25(12):2354, 2010.

[97] G. Schierning et al. Microcrystalline silicon formation by silicon nanoparticles. *J of Appl Phys*, 103(8):084305, 2008.

[98] D. Schwesig, G. Schierning, R. Theissmann, N. Stein, N. Petermann, H. Wiggers, R. Schmechel, and D. E. Wolf. From nanoparticles to nanocrystalline bulk: percolation effects in field assisted sintering of silicon nanoparticles. *Nanotechnology*, 22(13):135601, 2011.

[99] X. Song, X. Liu, and J. Zhang. Neck formation and self-adjusting mechanism of Neck growth of conducting powders in Spark Plasma Sintering. *J. Am. Ceram. Soc.*, 89(2):494, 2006.

[100] C. Shearwood, Y. Q. Fu, L. Yu, and K. A. Khor. Spark plasma sintering of TiNi nano-powder. *Scr. Mater.*, 52(6):455, 2005.

[101] T. B. Holland, U. Anselmi-Tamburini, D. V. Quach, T. B. Tran, and A-K. Mukherjee. Effects of local Joule heating during the field assisted sintering of ionic ceramics. *J. Eur. Cer. Soc.*, 32(14):3667, 2012.

[102] J. Trapp and B. Kieback. Temperature distribution in metallic powder particles during initial stage of field-activated sintering. *J. Am. Ceram. Soc.*, 98(11):3547, 2015.

[103] J. Gonzalez-Julian and O. Guillon. Effect of electric field/current on liquid phase sintering. *J. Am. Ceram. Soc.*, 98(7):2018, 2015.

[104] K. Vanmeensel, A. Laptev, J. Hennicke, J. Vleugels, and O. Van der Biest. Modelling of the temperature distribution during field assisted sintering. *Acta Mater.*, 53(16):4379, 2005.

[105] B. McWilliams and A. Zavaliangos. Multi-phenomena simulation of electric field assisted sintering. *J. Mater. Sci.*, 43(14):5031, 2008.

[106] S. Muñoz and U. Anselmi-Tamburini. Temperature and stress fields evolution during spark plasma sintering processes. *J. Mater. Sci.*, 45(23):6528, 2010.

[107] D. Giuntini, E. A. Olevsky, C. Garcia-Cardona, A. L. Maximenko, M. S. Yurlova, C. D. Haines, D. G. Martin, and D. Kapoor. Localized overheating phenomena and optimization of spark-plasma sintering tooling design. *Materials*, 6(7):2612, 2013.

[108] E. A. Olevsky, C. Garcia-Cardona, W. L. Bradbury, C. D. Haines, D. G. Martin, and D. Kapoor. Fundamental aspects of sparks plasma sintering: II. finite element analysis of scalability. *J. Am. Ceram. Society*, 95(8):2414, 2012.

[109] S. Angst, G. Schierning, and D. E. Wolf. Simulation of current-activated pressure-assisted densification. In *AIP Conference Proceedings*, volume 1542, page 593. AIP Publishing.

[110] G. Schierning, J. Stötzel, R. Chavez, V. Kessler, J. Hall, R. Schmechel, T. Schneider, N. Petermann, H. Wiggers, S. Angst, D. E. Wolf, B. Stoib, A. Greppmair, M. Stutzmann, and M. S. Brandt. Silicon-based nanocomposites for thermoelectric application. *Phys. Status Solidi A*, 213(3):497, 2016.

[111] S. Hartner, D. Schwesig, I. Plümel, D. E. Wolf, A. Lorke, and H. Wiggers. Electrical transport in semiconductor nanoparticle arrays: Conductivity, sensing and modeling. In *Nanoparticles from the Gasphase*, pages 231–271. 2012.

[112] D. Sornette and C. Vanneste. Dynamics and memory effects in rupture of thermal fuse networks. *Phys. Rev. Lett.*, 68(5):612, 1992.

[113] C. Pennetta, L. Reggiani, and Gy. Trefán. Scaling and universality in electrical failure of thin films. *Phys. Rev. Lett.*, 84(21):5006, 2000.

[114] G. Tørå and A. Hansen. Heat diffusion in a two-dimensional thermal fuse model. *Phys. Rev. E*, 81(6):o66111, 2010.

[115] B. Schmittmann and R. K. P. Zia. Statistical mechanics of driven diffusive systems. In *Phase Transition and Critical Phenomena*, volume 17. Academic Press, 1995.

[116] K.-T. Leung. Finite-size scaling of driven diffusive systems: Theory and Monte Carlo studies. *Phys. Rev. Lett.*, 66(4):453, 1991.

[117] D. Kadau, G. Bartels, L. Brendel, and D.E. Wolf. Pore stabilization in cohesive granular systems. *Ph. Transit.*, 76(4-5):315, 2003.

[118] F. A. Gilabert, J.-N. Roux, and A. Castellanos. Computer simulation of model cohesive powders: Plastic consolidation, structural changes, and elasticity under isotropic loads. *Phys. Rev. E*, 78(3):031305, 2008.

[119] S. Plimpton. Fast parallel algorithms for short-range molecular dynamics. *J. Comput. Phys.*, 117:1, 1995.

[120] S. Luding. Cohesive, frictional powders: contact models for tension. *Granul. Matter.*, 10(4):235, 2008.

[121] S. Strege, A. Weuster, H. Zetzener, L. Brendel, A. Kwade, and D. E. Wolf. Approach to structural anisotropy in compacted cohesive powder. *Granular Matter*, 16(3):401–409, November 2013.

[122] M. Morgeneyer, M. Röck, J. Schwedes, L. Brendel, K. Johnson, D. Kadau, D. Wolf, and L.-O. Heim. Compaction and mechanical properties of cohesive granular media. *Behavior of granular media : [proceedings of the final presentation of DFG research program "Verhalten granularer Medien"]*, 2006.

[123] T. C. Harman. Special techniques for measurement of thermoelectric properties. *J. App. Phys.*, 29(9):1373–1374, 1958.

[124] T. C. Harman, J. H. Cahn, and M. J. Logan. Measurement of thermal conductivity by utilization of the Peltier effect. *J. Appl. Phys.*, 30(9):1351, 1959.

[125] W. J. Turner, A. S. Fischler, and W. E. Reese. Physical properties of several II-v semiconductors. *Phys. Rev.*, 121(3):759, 1961.

[126] G. E. Smith and R. Wolfe. Thermoelectric properties of bismuth-antimony alloys. *J. Appl. Phys.*, 33(3):841, 1962.

[127] P. H. M. Böttger, K. Valset, S. Deledda, and T. G. Finstad. Influence of ball-milling, nanostructuring, and ag inclusions on thermoelectric properties of ZnSb. *J. Electron. Mater.*, 39(9), 2010.

[128] T. C. Harman, P. J. Taylor, M. P. Walsh, and B. E. LaForge. Quantum dot superlattice thermoelectric materials and devices. *Science*, 297(5590):2229, 2002.

[129] R. Singh, Z. Bian, G. Zeng, J. Zide, J. Christofferson, H.-F. Chou, A. Gossard, J. Bowers, and A. Shakouri. Transient Harman measurement of the cross-plane ZT of InGaAs/InGaAlAs superlattices with embedded ErAs nanoparticles. In *Symposium F - Materials and Technologies fore Direct Thermal-to-Electric Energy Conversion*, volume 886 of *MRS Online Proceedings Library Archive*, 2005.

[130] R. Singh, Z. Bian, A. Shakouri, G. Zeng, J.-H. Bahk, J. E. Bowers, J. M. O. Zide, and A. C. Gossard. Direct measurement of thin-film thermoelectric figure of merit. *Appl. Phys. Lett.*, 94(21):212508, 2009.

[131] R. Zeipl, M. Jelínek, J. Navrátil, T. Kocourek, S. Leshkov, F. Šroubek, J. Vanіž, and J. Walachová. Properties of thermoelectric Ce0.09Fe0.67Co3.33Sb12/FeSb2Te multi-layered structures prepared by laser ablation. *Thin Solid Films*, 548:590–596, 2013.

[132] R. Chavez, A. Becker, M. Bartel, V. Kessler, G. Schierning, and R. Schmechel. Note: High resolution alternating current/direct current Harman technique. *Rev. Sci. Instrum.*, 84(10):106106.

[133] X. Ao, J. de Boor, and V. Schmidt. Radiation-corrected Harman method for characterization of thermoelectric materials. *Adv. Energy Mater.*, 1(6):1007, 2011.

[134] M. A. Korzhuev and E. S. Avilov. Use of the Harman technique for figure of merit measurements of cascade thermoelectric converters. *J. Electron. Mater.*, 39(9):1499, 2010.

[135] R. J. Mehta, Y. Zhang, H. Zhu, D. S. Parker, M. Belley, D. J. Singh, R. Ramprasad, T. Borca-Tasciuc, and G. Ramanath. Seebeck and figure of merit enhancement in nanostructured antimony telluride by antisite defect suppression through sulfur doping. *Nano Lett.*, 12(9):4523, 2012.

[136] H. Scherrer and S. Scherrer. Thermoelectric properties of bismuth antimony telluride solid solutions. In *CRC Thermoelectrics Handbook: Macro to Nano*. CRC Press, 2005.

[137] G. Hurvits, R. Rosenbaum, and D. S. McLachlan. A quantitative analysis of the thermoelectric power measurements on composite Al-Ge films. *J. Appl. Phys.*, 73(11):7441, 1993.

[138] D. J. Bergman and O. Levy. Thermoelectric properties of a composite medium. *J. Appl. Phys.*, 70(11):6821–6833, 1991.

[139] D. G. Cahill, P. V. Braun, G. Chen, D. R. Clarke, S. Fan, K. E. Goodson, P. Keblinski, W. P. King, G. D. Mahan, A. Majumdar, H. J. Maris, S. R. Phillpot, E. Pop, and L. Shi. Nanoscale thermal transport. II. 2003-2012. *Appl. Phys. Rev.*, 1(1):011305, 2014.

[140] H. Bracht, S. Eon, R. Frieling, A. Plech, D. Issenmann, D. Wolf, J. Lundsgaard Hansen, A. Nylandsted Larsen, J. W. Ager Iii, and E. E. Haller. Thermal conductivity of isotopically controlled silicon nanostructures. *New J. Phys*, 16(1):015021, 2014.

[141] D. J. Bergman and L. G. Fel. Enhancement of thermoelectric power factor in composite thermoelectrics. *J. Appl. Phys.*, 85(12):8205, 1999.

[142] E Müller, K Zabrocki, C Goupil, G Snyder, and W Seifert. Functionally graded thermoelectric generator and cooler elements. In *CRC Thermoelectrics Handbook: Materials, Preparation, and Characterization in Thermoelectrics*. CRC Press, 2012.

[143] G. J. Snyder and T. S. Ursell. Thermoelectric efficiency and compatibility. *Phys. Rev. Lett.*, 91(14):148301, 2003.

[144] W. Seifert, G. J. Snyder, E. S. Toberer, C. Goupil, K. Zabrocki, and E. Müller. The self-compatibility effect in graded thermoelectric cooler elements. *Phys. Status Solidi A*, 210(7):1407, 2013.

[145] W. Seifert, V. Pluschke, and N. F. Hinsche. Thermoelectric cooler concepts and the limit for maximum cooling. *J. Phys. Condens. Matter*, 26(25):255803, 2014.

[146] W. Seifert and V. Pluschke. Maximum cooling power of a graded thermoelectric cooler. *Phys. Status Solidi B*, 251(7):1416, 2014.

[147] W. Seifert, K. Zabrocki, G. J Snyder, and E. Müller. The compatibility approach in the classical theory of thermoelectricity seen from the perspective of variational calculus. *Phys. Status Solidi A*, 207(3):760, 2010.

[148] Y. Apertet, H. Ouerdane, C. Goupil, and Ph. Lecoeur. Equivalent parameters for series thermoelectrics. *Energy Convers. Manage.*, 93:160, 2015.

[149] Y. Yang, F. Y. Ma, C. H. Lei, Y. Y. Liu, and J. Y. Li. Is thermoelectric conversion efficiency of a composite bounded by its constituents? *Appl. Phys. Lett.*, 102(5):053905, 2013.

[150] R. Saleh, P. Thomas, and I. P. Zvyagin. Internal currents in multi-layer structures. *Superlattices and Microstruct.*, 10(1):59, 1991.

[151] Y. Apertet, H. Ouerdane, C. Goupil, and Ph. Lecoeur. Thermoelectric internal current loops inside inhomogeneous systems. *Phys. Rev. B*, 85(3):033201, 2012.

[152] G. D. Mahan. Parallel thermoelectrics. *Physical Review B*, 87(4):045415, January 2013. 00003.

[153] Z. Bian and A. Shakouri. Beating the maximum cooling limit with graded thermoelectric materials. *Appl. Phys. Lett.*, 89(21):212101, 2006. 00018.

[154] M.V. Vedernikov and E.K. Iordanishvili. A.F. ioffe and origin of modern semiconductor thermoelectric energy conversion. In *17th International Conference on Thermoelectrics, 1998. ICT 98*, pages 37–42, 1998.

[155] G. Schierning, R. Chavez, R. Schmechel, B. Balke, G. Rogl, and P. Rogl. Concepts for medium-high to high temperature thermoelectric heat-to-electricity conversion: a review of selected materials and basic considerations of module design. *Transl. Mater. Res.*, 2(2):025001, 2015.

[156] A. Becker, R. Chavez, N. Petermann, G. Schierning, and R. Schmechel. A thermoelectric generator concept using a pqn junction: Experimental proof of principle. *J. Electron. Mater.*, page 2297, 2013.

[157] F. L. Curzon and B. Ahlborn. Efficiency of a carnot engine at maximum power output. *Am. J. Phys.*, 43(1):22, January 1975.

[158] J. M. Gordon. Generalized power versus efficiency characteristics of heat engines: The thermoelectric generator as an instructive illustration. *Am. J. Phys.*, 59(6):551, 1991.

[159] D. C. Agrawal and V. J. Menon. The thermoelectric generator as an endoreversible carnot engine. *J. Phys. D: Appl. Phys.*, 30(3):357, 1997.

[160] Y. Apertet, H. Ouerdane, O. Glavatskaya, C. Goupil, and P. Lecoeur. Optimal working conditions for thermoelectric generators with realistic thermal coupling. *EPL*, 97(2):28001, 2012.

[161] G. Span, M. Wagner, S. Holzer, and T. Grasser. Thermoelectric power conversion using generation of electron-hole pairs in large area pn junctions. In *25th International Conference on Thermoelectrics, 2006. ICT '06*, pages 23–28, 2006.

[162] M. Wagner, G. Span, S. Holzer, O. Triebl, T. Grasser, and V. Palankovski. Power output improvement of silicon-germanium thermoelectric generators. *ECS Trans.*, 3(7):1151, 2006.

[163] M. Wagner, G. Span, S. Holzert, and T. Grasser. Design optimization of large area Si/SiGe thermoelectric generators. In *2006 International Conference on Simulation of Semiconductor Processes and Devices*, pages 397–400, September 2006.

[164] M. Wagner, G. Span, S. Holzer, and T. Grasser. Thermoelectric power generation using large-area Si/SiGe pn-junctions with varying Ge content. *Semicond. Sci. Technol.*, 22(1):173, 2007.

[165] T. Grasser and S. Selberherr. IμE Minimos-NT 2.1 user's guide. *Institute for Microelectronics, Technische Universität Wien, Austria*, 2004.

[166] S. M. Sze and K. K. Ng. *Physics of Semiconductor Devices*. John Wiley & Sons, 2006.

[167] D. Fu, A. X. Levander, R. Zhang, J. W. Ager, and J. Wu. Electrothermally driven current vortices in inhomogeneous bipolar semiconductors. *Phys. Rev. B*, 84(4):045205, 2011.

[168] J. Y. Yang, T. Aizawa, A. Yamamoto, and T. Ohta. Effects of interface layer on thermoelectric properties of a pn junction prepared via the BMA-HP method. *Mat. Sci. Eng. B-Solid*, 85(1):34, 2001.

[169] P. L. Hagelstein and Y. Kucherov. Enhanced figure of merit in thermal to electrical energy conversion using diode structures. *Appl. Phys. Lett.*, 81(3):559–561, 2002.

[170] Y Kucherov, P. Hagelstein, V. Sevastyanenko, H. L. Brown, S. Guruswamy, and W. Wingert. Importance of barrier layers in thermal diodes for energy conversion. *J. Appl. Phys.*, 97(9):094902, 2005.

[171] T. Kumpeerapun, V. Kosalathip, H. Scherrer, A. Dauscher, W. Onreabroy, and I. Sripichai. Fabrication of pn junctions of Bi-Sb-Te thermoelectric materials. In *26th International Conference on Thermoelectrics, 2007. ICT 2007*, pages 42–44, 2007.

[172] André Becker. *Präparation und Eigenschaften monolithisch gesinterter Silizium pn Übergänge für thermoelektrische Anwendungen*. PhD thesis, Universität Duisburg-Essen, 2013.

[173] R. Chavez, S. Angst, J. Hall, J. Stötzel, V. Kessler, L. Bitzer, F. Maculewicz, N. Benson, H. Wiggers, D. Wolf, G. Schierning, and R. Schmechel. High temperature thermoelectric device concept using large area pn junctions. *J. Electron. Mater.*, page 2376, 2013.

[174] V. Kessler, M. Dehnen, R. Chavez, M. Engenhorst, J. Stötzel, N. Petermann, K. Hesse, T. Huelser, M. Spree, C. Stiewe, P. Ziolkowski, G. Schierning, and R. Schmechel. Fabrication of high-temperature-stable thermoelectric generator modules based on nanocrystalline silicon. *J. Electron. Mater.*, 43(5):1389, 2014.

[175] R. Chavez, S. Angst, J. Hall, H. Wiggers, D. Wolf, R. Schmechel, and G. Schierning. Thermoelectric module design for high temperature applications. *to be submittted*, 2016.

[176] A. Becker, G. Schierning, R. Theissmann, M. Meseth, N. Benson, R. Schmechel, D. Schwesig, N. Petermann, H. Wiggers, and P. Ziolkowski. A sintered nanoparticle pn junction observed by a Seebeck microscan. *J. Appl. Phys.*, 111(5), 2012.

[177] M. Meseth, P. Ziolkowski, G. Schierning, R. Theissmann, N. Petermann, H. Wiggers, N. Benson, and R. Schmechel. The realization of a pn diode using only silicon nanoparticles. *Scr. Mater.*, 67(3):265, 2012.

[178] E. Lorenzo. *Solar Electricity: Engineering of Photovoltaic Systems*. PROGENSA, 1994.

[179] V. Kessler, D. Gautam, T. Hülser, M. Spree, R. Theissmann, M. Winterer, H. Wiggers, G. Schierning, and R. Schmechel. Thermoelectric properties of nanocrystalline silicon from a scaled-up synthesis plant. *Adv. Eng. Mater.*, 15(5):379, 2013.

[180] K. Bartholomé, B. Balke, D. Zuckermann, M. Köhne, M. Müller, K. Tarantik, and J König. Thermoelectric modules based on half-Heusler materials produced in large quantities. *J. Electron. Mater.*, 43(6):1775, 2013.

[181] Wolfram Research Inc. Mathematica 10.4, 2016.

[182] H. Görtler. *Dimensionsanalyse: Theorie der physikalischen Dimensionen mit Anwendungen*. Springer Berlin Heidelberg, 1975.

PUBLICATIONS

Some ideas and figures have appeared previously or will be published soon in the following publications:

1. A. Becker, S. Angst, A. Schmitz, M. Engenhorst, J. Stötzel, D. Gautam, H. Wiggers, D. E. Wolf, G. Schierning, and R. Schmechel. The effect of Peltier heat during current activated densification. *Appl. Phys. Lett.*, 101(1):013113, 2012.

2. R. Chavez, S. Angst, J. Hall, J. Stötzel, V. Kessler, L. Blitzer, F. Maculewicz, N. Benson, H. Wiggers, D. E. Wolf, G. Schierning and R. Schmechel. High temperature thermoelectric device concept using large area pn junctions. *J. Electron. Mater.*, page 2376, 2013

3. S. Angst, G. Schierning, and D. E. Wolf. Simulation of current-activated pressure-assisted densification. In AIP *Conference Proceedings*, volume 1542, page 593. AIP Publishing.

4. S. Angst and D. E. Wolf. Network theory for inhomogeneous thermoelectrics. *New J. Phys.*, 18(4):043004, 2016.

5. G. Schierning, J. Stötzel, R. Chavez, V. Kessler, J. Hall, R. Schmechel, T. Schneider, N. Petermann, H. Wiggers, S. Angst, D. E. Wolf, B. Stoib, A. Greppmair, M. Stutzmann, and M. S. Brandt. Silicon-based nanocomposites for thermoelectric application. *Phys. Status Solidi A*, 213(3):497, 2016.

6. R. Chavez, S. Angst, J. Hall, H. Wiggers, T. H. Le, N. Nong, N. Pryds, G. Span, D. E. Wolf, R. Schmechel, and G. Schierning. Thermoelectric module design for high temperature applications. *submittted*, 2016.

7. S. Angst, L. Engelke, M. Winterer, D. E. Wolf. Models of current sintering *submittted*, 2016.

8. S. Angst, D. E. Wolf. Performance of segmented thermoelectrics. *to be submitted*, 2016.

ERKLÄRUNG

Die vorliegende Dissertation wurde von mir selbständig verfasst. Bei der Abfassung der Dissertation wurden nur die angegebenen Hilfsmittel benutzt und alle wörtlich oder inhaltlich übernommenen Stellen sind als solche gekennzeichnet. Die Dissertation ist nur in diesem Promotionsverfahren eingereicht und es wird der Doktorgrad Dr. rer. nat. angestrebt.

Duisburg, 14.04.2016

Sebastian Angst

DANKSAGUNG

An dieser Stelle möchte ich jenen danken, die zum Gelingen dieser Arbeit wesentlich beitrugen.

Ein großer Dank gilt Prof. Dietrich E. Wolf für die Betreuung meiner Promotion, für die vielen fruchtbaren Diskussionen sowie die Ermöglichung der zahlreichen Konferenzteilnahmen und Auslandsaufenthalte.

Ich danke auch Dr. Gabi Schierning, Prof. Roland Schmechel und deren Arbeitsgruppe für die hervorragende Zusammenarbeit und eine Vielzahl inspirierender Diskussionen, die nahezu alle in meiner Arbeit angesprochenen Themen berührten.

Besonders danke ich Dr. Ruben Chavez für die intensiven, erkenntnisreichen und freudvollen Diskussionen sowie die produktive Kollaboration auf dem Gebiet des pn-Generators.

Des Weiteren gilt mein Dank Dr. André Becker für die gute Kooperation und die Einführung in die stromassistierte Druckverdichtung.

Für die gute Arbeitsatmosphäre und die physikalischen und nichtphysikalischen Gespräche danke ich der AG Wolf. Für die Unterstützung bei Problemen mit dem Computer danke ich Dr. Lothar Brendel und Stephan Schulz. Weiterer Dank gilt Alexander Weuster für die Unterstützung bei den Molekular Dynamik Simulationen und der freundschaftlichen Gesellschaft seit Beginn unseres Studiums.

Für das Korrekturlesen des Textes danke ich Anthony Ajunwa, Anja Angst, Wilfried Angst, Carl Friedrich Bolz, Marta Arias Campo und Alexander Weuster.

Bei Familie und Freunden, insbesondere bei Marta Arias Campo, bedanke ich mich für die vielfältige Hilfe und die Ermunterungen.